# Nucleobases in Supercritical Fluids: Solubility, Molecular Beam Expansion, and Surface Deposition

DISSERTATION

zur Erlangung des akademischen Grades

Dr. rer. nat.
im Fach Chemie

eingereicht an der
Mathematisch-Naturwissenschaftlichen Fakultät I
Humboldt-Universität zu Berlin

von
**Herrn Adnan Sarfraz**
geboren am 24.02.1980 in Lagos, Nigeria

Präsident der Humboldt-Universität zu Berlin:
Professor Dr. Christoph Markschies

Dekan der Mathematisch-Naturwissenschaftlichen Fakultät I:
Professor Dr. Lutz-Helmut Schön

Gutachter:
1. Professor Dr. Klaus Rademann
2. Professor Dr. Ulrich Panne

**eingereicht am:** 23.11.2009
**Tag der mündlichen Prüfung:** 22.12.2009

# Dedication

To Ammi and Abu.

# Zusammenfassung

Überkritische Fluide haben Anwendungen in vielen Bereichen, als Lösungsmittel, Reaktionsmedium oder bei der Erzeugung von Nanopartikeln. Sie sind auch beim Transport nicht flüchtiger organischer Moleküle in die Gasphase und zur Abscheidung auf Oberflächen von Interesse. Diese Arbeit zeigt die Verwendung überkritischer Fluide als analytisches Werkzeug für den Transport einer Gruppe nichtflüchtiger Moleküle, nämlich Nucleobasen, in die Gasphase. Das am häufigsten verwendete überkritische Fluid ist Kohlendioxid, welches sich jedoch als zu ineffizient bei der Auflösung von Nucleobasen, selbst bei Verwendung eines Cosolvens, herausstellte. Deshalb wurde ein Gemisch aus Ethylen ($p_c$ = 50,6 bar und $T_c$ = 9,35 °C) mit Ethanol als Cosolvens als überkritisches Lösungsmittel verwendet.

Für die Erkennung des kritischen Punktes reiner Fluide oder verdünnter Fluidmischungen wurde eine neue Methode entwickelt. Die Verschiebung des kritischen Punktes von Ethylen durch Zugabe von Ethanol wurde experimentell ermittelt und mit der Zustandsgleichung von Soave Redlich Kwong in Beziehung gesetzt. Für einen Molenbruch des Cosolvens Ethanol von 0.054 erhöht sich die kritische Temperatur nur um 5,5 °C, wohingegen die Theorie eine Erhöhung um 10 °C vorhersagt.

Fünf biologisch relevante Nucleobasen Adenin, Guanin, Cytosin, Thymin und Uracil wurden mit Hilfe von 3% Ethanol als Cosolvens in überkritischem Ethylen gelöst. Die Zusammensetzung des Überschall-Molekularstrahles der expandierten Lösung wurde mit einem Quadrupol-Massenspektrometer quantitativ analysiert. Das Signalverhältnis der Nucleobasen zu Ethylen lag in der Größenordnung von $10^{-4}$ bis $10^{-5}$. Ihre unterschiedlichen Löslichkeiten können durch die Reihenfolge Cytosin > Uracil ∼ Adenin > Guanin > Thymin beschrieben werden.

Diese Nucleobasen wurden auch auf Oberflächen abgeschieden, sowohl durch Hochdruckexpansion der überkritischen Lösungen, als auch durch Verdampfung von alkoholischen Lösungen (nach der 'Drop Casting' Methode). Die dabei entstehenden Morphologien wurden ex-situ mittels Rasterkraftmikroskopie untersucht. Mit der 'Drop Casting' Methode ergeben sich im Falle des Cytosins längliche, leicht gekrümmte Strukturen mit einem großen Aspektverhältnis. Nach Hochdruckexpansion wurden dünne Filme mit überwiegend sphärischen Partikeln mit einem Durchmesser im Bereich von Nanometer bis Mikrometer beobachtet. Die Ursachen dieser Unterschiede werden anhand der relevanten Nukleationsmechanismen diskutiert.

# Abstract

Supercritical fluids have found applications in a wide variety of fields, from solvents for reaction media to engineering of nanoparticles. They are also of interest in the analytical field for transferring non-volatile organic molecules into the gas phase for detection and deposition purposes. This work highlights the use of supercritical fluids as an analytical tool for the transfer of a group of non-volatile molecules, namely nucleobases, into the gas phase. The most commonly used supercritical fluid, carbon dioxide was found inefficient in dissolving the nucleobases even with the help of a cosolvent. Therefore, for this purpose a mixture of ethylene ($p_c = 50.6$ bar and $T_c = 9.35$ °C) with a cosolvent was used as the supercritical solvent.

A new bracketing method was developed for detecting the critical point of pure fluids and diluted mixtures of fluids. The shift in critical point of ethylene on addition of ethanol was determined and related to theoretical calculations by using the Soave Redlich Kwong equation of state. Comparing the experimental results to purely theoretical methods for calculating the critical point showed large deviations even at low concentrations. The critical temperature shifted by only 5.5 °C when the mole fraction of the cosolvent i.e. ethanol was 0.054.

Five biologically relevant nucleobases i.e. adenine, guanine, cytosine, thymine and uracil were dissolved in supercritical ethylene using 3% of ethanol as cosolvent. The supersonic molecular beam composition of the expanded solution was analyzed quantitatively using a quadrupole mass spectrometer and the ratio of the nucleobases to ethylene in the beam was found to be of the order of $10^{-4}$ to $10^{-5}$. The solubility for different nucleobases increased in the following order: cytosine $>$ uracil $\sim$ adenine $>$ guanine $>$ thymine.

Surface deposition of the nucleobases through supercritical fluid solutions was carried out and the morphology was recorded using Atomic Force Microscopy. Remarkable differences were observed while comparing the morphology obtained after deposition using rapid expansion of supercritical solutions (RESS) and drop casting method. For example, in the case of cytosine, the drop casting method produced rather long ($\sim$ $\mu$m range) curved rods with high aspect ratios, whereas spherical particles (ranging from nanometer to micrometer sizes) were observed in a thin particulate film when deposited using RESS. These differences are discussed in terms of diffusion, rate of evaporation of the solvent, degree of supersaturation, and the nucleation process.

# Contents

# List of Figures

# List of Tables

# 1. Introduction

## 1.1. Discovery of Supercritical Fluids

Nearly two hundred years ago in 1822, Cagniard de la Tour (1777 - 1859) made a historic experiment by rolling a flint ball in a sealed cannon partially filled with a liquid. He noticed that upon heating the system above a certain temperature above it's boiling point, the splashing sound which was generated by the flint ball passing the gas-liquid interface, disappeared. He noticed that this *"état particulier"* required high temperatures and did not depend on the volume of the system.[22] Faraday later called this point *"Cagniard de la Tour's state"* and the *"the Cagniard de la Tour point"*. Dmitri Mendeleev later renamed it to *"absolute Siedetemperatur"* or *absolute boiling point.*[77] Finally in 1869, the name *critical point* was given to it by Thomas Andrews,[3] which has been ever since in use. Any substance in the region above the critical temperature and pressure is called a supercritical fluid (SCF).

Since then, supercritical fluids have been employed as reaction medium[27] and also used widely in a number of fields like extraction[112] and purification.[6] To mark the 150th anniversary of the passing of Cagniard de la Tour, a short review was published by Berche et al.[8]

## 1.2. Critical Point

A simplified picture of the critical point can be obtained by considering the following definition. In a substance at the critical point, the average kinetic energy of the particles is equal to their average negative potential energy[119]. Thus, a substance present in the supercritical state cannot be condensed into a liquid by increasing the pressure.

While approaching the critical point by increasing the temperature, large density fluctuations occur and lead to a complete opacity at the critical point. This phenomenon is called critical opalescence and was first described by Andrews[3] and later quantitatively related to Rayleigh Scattering by Einstein[35]. Table 1.1 shows some substances which are of interest in the field of research pertaining to supercritical fluids.

## 1.3. Supercritical Fluids

A substance in the supercritical state is known to have properties from both gas and liquid phase. It has the ability to fill the container like a gas, and it can also dissolve a solute in it like a liquid. A general comparison of different physical properties of a substance in the supercritical state with liquids and gases is given in Table 1.2. It can

| **Molecule** | **Critical Temperature** $T_c$ (K) | **Critical Pressure** $p_c$ (bar) | **Critical Volume** $\nu_c$ (l/mol) | **Acentric Factor** $\omega$ |
|---|---|---|---|---|
| Argon | 150.9 | 49.0 | 0.075 | 0 |
| Ethylene | 282.5 | 50.6 | 0.131 | 0.089 |
| Fluoroform | 299.1 | 48.3 | 0.124 | 0.260 |
| Carbon dioxide | 304.2 | 73.8 | 0.092 | 0.239 |
| Ethanol | 514.0 | 63.0 | 0.168 | 0.649 |

Table 1.1.: Different properties relevant to the critical point for a number of molecules.[93]

be seen that in the supercritical region, the substance exhibits higher diffusitivity as compared to a liquid and is much more viscous than a gas. The behavior of density around the critical point can be seen in Figure 1.1b. The ability to control the density of a supercritical fluid by slight variation of pressure or temperature allows control over many physical properties of the supercritical fluid.

The most widely used supercritical fluid is carbon dioxide because of it being environmentally benign. It also has the property of dissolving a variety of organic molecules. The problem faced while using $CO_2$ for dissolution of organic molecules is that it is non-polar in nature, while many organic and bio-organic molecules of interest are polar in nature. This problem is usually tackled by using a cosolvent to increase the solubility of the solute.[121]

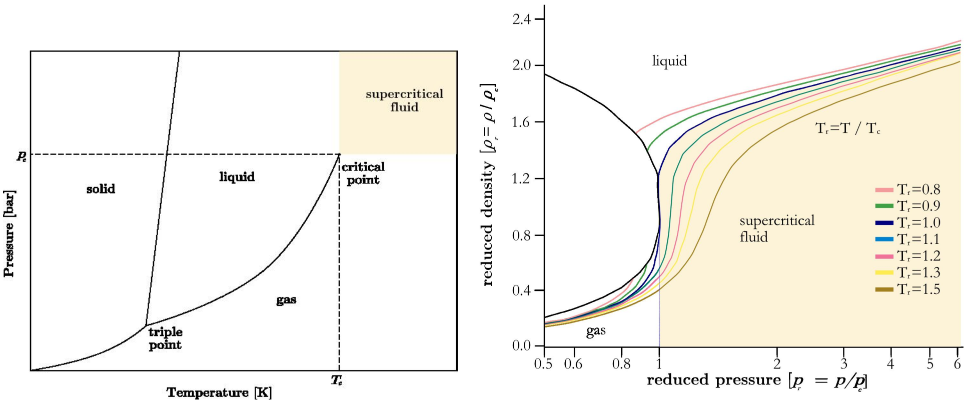

(a) (b)

Figure 1.1.: (a)$p$-$T$ phase diagram of $CO_2$. (b) density dependence of $CO_2$ in terms of reduced pressure and temperature.[66]

| **Property** | **Gas** | **SCF** | **Liquid** |
|---|---|---|---|
| Density [g ml$^{-1}$] | $10^{-3}$ | 0.4 | 1 |
| Viscosity [Pa s] | $10^{-5}$ | $10^{-4}$ | $10^{-3}$ |
| Diffusitivity [cm$^2$ s$^{-1}$] | $10^{-1}$ | $> 10^{-3}$ | $10^{-5}$-$10^{-6}$ |

Table 1.2.: Comparison of some physical properties in different phases.

### 1.3.1. Supercritical Ethylene

Ethylene in its supercritical state is also used for studying the solubility of organic molecules,[67] extraction[105] and as a reaction medium[49]. The study of supercritical state of ethylene is also motivated by the fact that ethylene is a raw material in the petrochemical industry and is in the critical state while being transported. The critical point ($T_c = 9.35$ °C, $p_c = 50.6$ bar) of ethylene is relatively low and easily achievable under laboratory conditions.

### 1.3.2. Solvation in Supercritical Fluids

An interesting property observed for the solvation of a solute in supercritical fluids is that the local density of the solvent molecules around the solute increases significantly. This concept of 'local density augmentation' was originally proposed by Eckert et al.[32,33] A representative diagram of this clustering effect is shown in Figure 1.2. This difference in bulk solvent density to local solvent density leads to large and negative partial molar volumes of a solute in the supercritical fluid.[33] Moreover, this effect can also influence a number of processes like reaction rates, extraction and solute conformation in the fluid. Kajimoto[52] gave an extensive review on the understanding of the solvation process in supercritical fluids.

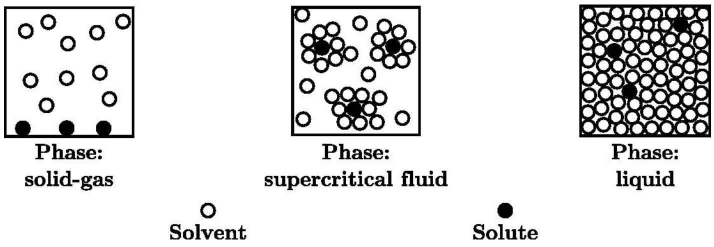

Figure 1.2.: Representative diagram of the clustering effect in supercritical fluids.

### 1.3.3. Cosolvents in Supercritical Fluids

To modify the properties of supercritical fluids, very often cosolvents in small amounts are used. This small amount ($1 - 5\%$) can significantly increase the dissolving power of the fluid. The cosolvent effect is mainly used to increase the solubilities of solutes[128] and to increase the selectivity of a solute for extraction purposes.[2,29] For example, if a polar cosolvent is added to a nonpolar supercritical fluid, it can increase the solubility of a polar solute up till one order of magnitude.[37] Low molecular weight volatile organic solvents are commonly used as cosolvents, although other supercritical fluids[1] as well as solid cosolvents[116] have also been found to be helpful in increasing the solubility of a solute.

When a cosolvent is added to the supercritical fluid to facilitate the dissolution of a solute, cosolvent solute interactions become very important. The cosolvent preferentially forms a solvation shell around the solute rather than the solvent.[72] Thus a local density enhancement of the cosolvent around the solute takes place. The study of the solvation structure in a supercritical fluid is usually performed by using a dye molecule,[68] as it exhibits features which strongly depend on the physicochemical properties of their surroundings.

Tavana et al.[115] proposed an experimental method of selecting a suitable cosolvent for a particular solute. They measured the affinity of a solute to the cosolvent in the vapor phase using gas chromatography and found it to be related to the solubility of the solute in that solvent.

The addition of a cosolvent although advantageous, shifts the critical temperature and pressure of the supercritical fluid even at low concentrations. Thus, information relevant to the binary mixture becomes a necessity for further studies relevant to the applications of this mixture.

### 1.3.4. Binary Mixtures

In the case of a cosolvent being added to a SCF, the critical pressure and temperature of the cosolvent is usually higher than that of the SCF. This leads to the fact that on addition of the cosolvent, the critical temperature and pressure of a system will tend to increase. Knowledge regarding the phase behavior thus becomes important for such a mixture. $p$-$T$ phase diagrams are used to describe the behavior of such binary mixtures.

The phase diagrams are divided into six types[19] and are shown in Figure 1.3. $\mathrm{C}_\alpha$ and $\mathrm{C}_\beta$ denote the critical points of the two components and the dashed lines represent the critical line for the mixture. Based on the properties of the second component, these types can be further divided into two classes. The phase diagrams of Types 1, 2, and 6 is usually observed when a cosolvent is added to a supercritical fluid, whereas the Types 3, 4, and 5 are applicable when a solid solute is added to the SCF. It can be observed that the major differences in the phase diagrams in each class are below the critical temperatures of the two components and thus will not be important when the mixture is in the supercritical phase.

Thus, when dealing with a mixture of a supercritical fluid the knowledge of the critical coordinates become very important before the mixture can be used for dissolution purposes.

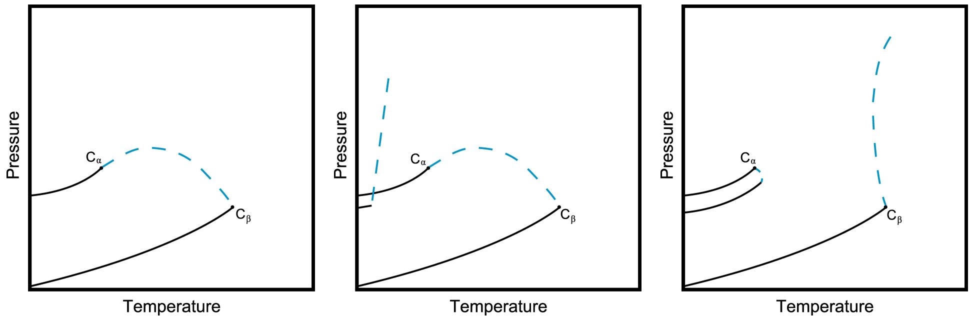

(a) Type 1 (b) Type 2 (c) Type 3

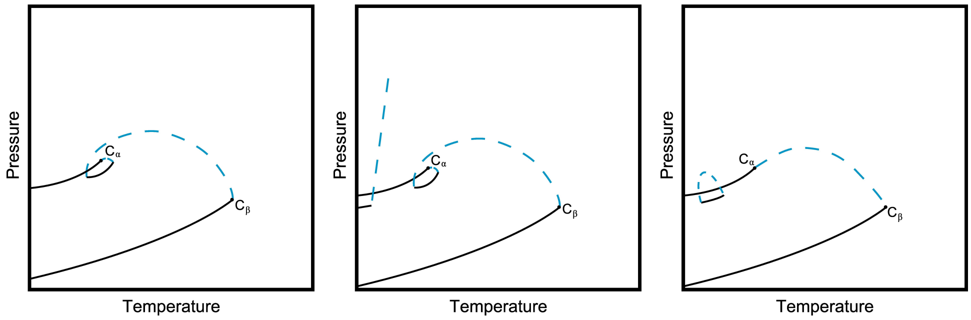

(d) Type 4 (e) Type 5 (f) Type 6

Figure 1.3.: Typical phase diagrams of binary mixtures of supercritical fluid with a co-solvent.[19]

## 1.4. Determination of the Critical Point

A vast variety of data exists[5] relevant to the experimental and theoretical determination of phase equilibria of binary mixtures of SCFs due to interest in the engineering field. A classification of the different methods available for measuring the phase equilibria has been reported in literature.[79] Determination of critical transition of mixtures can be done either experimentally and theoretically.

### 1.4.1. Experimental Methods

Detection of critical opalescence at the critical point is one of the most accurate methods of determining the critical coordinates of supercritical fluids. The detection of this phenomenon requires precise control of the temperature of the system (± 1 mK).[122] This phenomenon can be observed visually[69] or by measuring the scattering of light through the system.[82]

Other experimental methods to detect the critical transition exploit the change in a physical property near the critical point. The speed of sound depends on the properties of the medium that the sound waves are propagating through. It changes significantly when the substance approaches its critical point. The speed of sound shows a minimum[94] at the critical temperature and pressure and can thus be used to measure the critical point quite accurately.

Ziegler et al.[129] proposed a relatively fast method for measuring the critical point of mixtures using chromatography. Based on the shape of the chromatographic peaks of the mixture, they were able to assign the aggregation state of the mixture and thus measure the critical point.

Oag et al.[84] reported the critical point of a number of systems using a multitechnique approach and concluded that observing the scattering of light in the vicinity of the critical point leads to an accurate determination of the critical coordinates.

In using spectroscopic methods for studying high pressure fluids, there are a number of precautions that need to be taken. A modern high pressure setup is mainly composed of stainless steel components because of its inert nature. Quartz windows are most commonly installed in a high pressure setup for performing UV-Vis spectroscopy. Most common sealing materials used for the windows are polymer O-rings. The selection of the material of these sealing needs to be done with care as many fluids at high pressure have the ability to dissolve polymers. For example carbon dioxide in the supercritical state has the ability to dissolve many fluoropolymers thus making them ineffective as sealing materials, whereas the same material would work for supercritical ethylene since these polymers are inert to it.

### 1.4.2. Theoretical Methods

Due to the complexity of multicomponent mixtures, it is much more practical in industrial applications to use theoretical methods for determining the critical point of the mixture. Many theoretical methods exist for determining the critical point of mixtures and have been reviewed extensively.[101]

Empirical equations of state are commonly used to describe the phase behavior of fluids and the most common are of the van der Waals (vdW) type. The vdW type equation of state can be expressed as shown below:

$$p = \frac{RT}{\nu - b} - \frac{a}{\nu^2 + ub\nu + wb^2} \tag{1.1}$$

where $\nu$ is the molar volume, $u$ and $w$ are integer values given in Table 1.3, and $a$ and $b$ are parameters which account for the energy of interaction and covolume occupied by the molecules, respectively.

These equations of states can be used to derive expressions for determining the critical pressure and temperature of mixtures.[4] For binary systems, mixing rules for the parameters $a$ and $b$ are required which include binary interaction parameters. These binary interaction parameters are empirically determined to fit the results of the calculations to experimental results.

The vdW equation of state is no longer used for quantitative calculation because of development of modified and more advanced versions of the equation. Some of the equations are shown in Table 1.3 and have been used for different systems with varying success. A comparison of many different equations of state for a number of systems has

| equation | u | w | b | a |
|---|---|---|---|---|
| van der Waals | 0 | 0 | $\frac{RT_c}{8p_c}$ | $\frac{27R^2T_c^2}{64p_c}$ |
| Redlich Kwong[100] | 1 | 0 | $\frac{0.0867RT_c}{p_c}$ | $\frac{0.4278R^2T_c^{2.5}}{p_cT^{0.5}}$ |
| Soave-Redlich-Kwong[109] | 1 | 0 | $\frac{0.0867RT_c}{p_c}$ | $\frac{0.4278R^2T_c^2}{p_c}\alpha^a$ |
| Peng-Robinson[89] | 2 | -1 | $\frac{0.07780RT_c}{p_c}$ | $\frac{0.45724R^2T_c^2}{p_c}\alpha^b$ |

---

${}^a\alpha = [1 + M(1 - T_r^{0.5})]^2$ and $M = 0.48 + 1.574\omega + 0.176\omega^2$

${}^b\alpha = [1 + M(1 - T_r^{0.5})]^2$ and $M = 0.37464 + 1.54226\omega + 0.26992\omega^2$

Table 1.3.: Different properties relevant to the critical point of a number of molecules with different parameters.[93] $\alpha$ is a temperature dependent parameter and $\omega$ is the acentric factor of the substance.

been provided by Palenchar et al.[73] They reported that Soave-Redlich-Kwong Equation of State (SRK-EOS) could generally describe the critical temperature and pressure for a number of systems with much more accuracy as compared to other two-constant or three-constant equations of state.

Apart from using equations of state which require experimental data for describing the critical coordinates, purely theoretical methods also exist. One such method was proposed by Liu,[71] which uses only properties of the pure components in the mixture. Kolář et al.[65] used a semi-empirical method known as UNIFAC (Unified Functional Activity Coefficient) to predict the critical point of a number of mixtures with varying degree of success.

## 1.5. Nucleobases

The nucleobases (guanine, thymine, adenine, cytosine and uracil) have been the focus of recent research in a variety of fields such as radiation damage of biological tissues, gas phase spectroscopy and surface chemistry. Radiation damage to the nucleobases has been studied for gaining insight into the interaction of radiations with the human skin.[20,114] The gas phase investigations have been an area of interest to study the constituents of the nucleobase in a solvent free environment and thus study the intrinsic properties of the molecules.[23,50,55] Research of the nucleobases on surfaces is motivated by DNA microarray formation and the possibility of usage of the nucleobases in electronics devices.[54,85,92,125]

The Watson Crick base pairing of nucleobases in the DNA was first proposed by Watson and Crick in the historic publication[120] in which they explained the double helix structure of the DNA.

Apart from Watson-Crick base pairing, each individual nucleobase has the ability to form keto-enol tautomers. The biological significance of this phenomenon has also led to many theoretical and experimental studies of tautomerism of the nucleobases.[21,23]

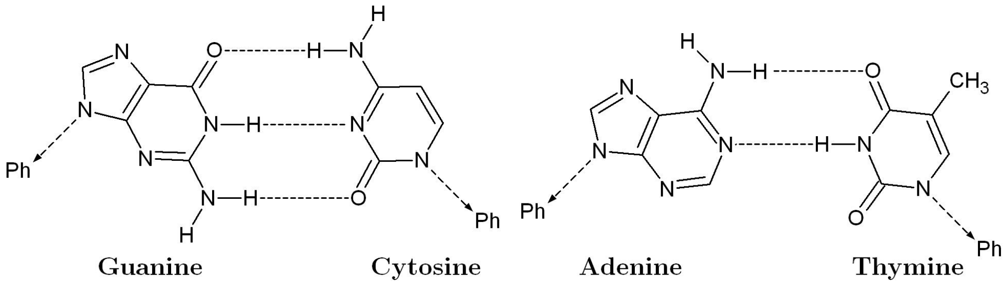

(a) (b)

Figure 1.4.: Watson Crick base pairing of nucleobases in the DNA. Ph denotes the bond to the phosphate backbone. In the RNA thymine is replaced by uracil.

## 1.5.1. Nucleobases in Solution

Solution studies of the nucleobases are mainly motivated due to their application in electrochemical sensors.[31]

Stofer et al.[111] theoretically calculated the free energies of the Watson-Crick base pairing and the energies matched those determined experimentally. In aqueous solutions of the nucleobases, they reported the free energy increment to be at 2 kcal/mol per hydrogen bond.

The knowledge regarding solubility of the nucleobases in supercritical fluids can lead to applications in extraction and purifications of these compounds. Burgos-Solórzano et al.[10] measured the solubility of uracil in supercritical carbon dioxide and found it to increase from $10^{-5}$ to $10^{-3}$ mole fraction on increasing the temperature from 40 °C to 60 °C and the pressure from 100 to 300 bar. They concluded that this increase in solubility is mainly caused by the increased vapor pressure of the solute and can be further increased by using an appropriate cosolvent.

## 1.5.2. Nucleobases in the Gas Phase

Even though sublimation and laser ablation has been widely used to transfer them into the gas phase, certain nucleobases have been reported to be relatively labile and sensitive to heat. Specifically cytosine and guanine have been reported[56] to dissociate on mild heating.

Hydration of the DNA bases adenine and thymine has been studied in the gas phase by Kim et al.[55] They observed well defined hydration shells consisting of four water molecules for both adenine and thymine.

The possibility of these molecules being delivered to early Earth[9] through space has also motivated research in studying photophysics and photochemistry of these molecules in vacuum. Jochims et al.[50] measured the fragmentation pattern and ionization energies of adenine, thymine, and uracil and suggested on the basis of the results that these molecules can easily by dissociated in interstellar medium and thus need to be present in radiation shielded meteorites for transport through space.

The biological importance of the nucleobases has also sparked a large number of research papers detailing the radiation damage of these molecules. Schlathölter et al.[104] reviewed the current understanding of interaction of low energy electrons with the nucleobases with relevance to radiation damage.

In an effort to study the Watson-Crick base pairs in gas phase, Dey et al.[28] expanded mixtures of the nucleobases in the gas phase. Nir et al.[83] also analyzed the different hydrogen bonded structures of adenine-thymine base spectroscopically in the gas phase and concluded with the help of ab initio calculations that the Watson-Crick pair was not the most stable isomer. In order to study the photostability of the nucleobases, Samoylova et al.[102] investigated the excitation dynamics of the nucleobases using femtosecond pump-probe. Moreover, presence of a number of different tautomers in the gas phase for each nucleobases has been observed and a comprehensive review has been published recently.[23]

### 1.5.3. Nucleobases on Surfaces

The interactions between biological material and surfaces are of interest because of a vast range of applications from biosensors, medical implants to biofouling. In all of these areas, surface design, interaction of surface with different materials, and the orientation of molecules on the surface are key elements. The insight into these elements can largely help in designing e.g. biosensors, medical implants etc. The preparation and characterization of surfaces used in the above mentioned examples require sophisticated surface science knowledge. Similarly in the field of bioelectronics, the basic need is to obtain surfaces on which molecules are confined to certain locations, which of course again requires suitable surface chemistry data. Sarantopoulou et al.[103] reported a rare study of imaging of thin films of DNA bases upon irradiation with a laser light at 157 nm. AFM images of the etched DNA bases exhibited very uniform films as compared to the non-etched ones. Östblom et al.[85] reported an extensive study of structure of the DNA bases on a polycrystalline gold surface. They reported the desorption dynamics of the nucleobases and concluded that the adhesive forces play a more important role for adenine desorption for gold, whereas for guanine cohesive forces are more relevant in obtaining a stable layer.

The focus of research related to the nucleobases on surfaces also concentrates on studying ordering of the nucleobases at a molecular level on different metal surfaces. Otero et al.[86] reported the formation of guanine quartets on Au(111) and explained this structure on the basis of resonance-assisted hydrogen bonding of the molecules. By using scanning tunneling microscopy (STM) at the liquid-solid interface, Xu et al.[123] showed the presence of guanine-cytosine base pairs on a graphite surface.

Research relevant to adenine deposited on substrates is also motivated by theoretical models predicting it's presence in interstellar dust clouds.[108] Mateo-Martí et al[75] studied the ultraviolet photostability of adenine on different surfaces in vacuum.

## 1.6. Molecular Beams

The molecular beam technique is a frequently used method for studying isolated particles. In a molecular beam the free path length of particles in the beam is very large in comparison with the scale of the measurement apparatus, so that there is no interaction occurring between the particles as well as with the background gas. This isolated state of the molecules is used for investigations without significant amount of interference. A molecular beam is obtained by coupling a high pressure source with a vacuum chamber through a nozzle.

The molecular beams can be divided into two categories namely effusive beams and supersonic jets. The type of the molecular beam depends on the orifice diameter of the beam source and expansion conditions. An effusive beam[97] is obtained when the mean free path of the molecules ($\lambda_0$) inside the beam source is larger than the orifice diameter (d). In an effusive molecular beam no collisions occur between the molecules present in the beam. The velocity distribution of such a beam is simply described by velocity weighted Boltzmann distribution, which is characteristic of the beam source temperature. The advantages of using an effusive beam is the low consumption and consequently low demands upon the pumping speed in the expansion chamber. The beam thus produced is well defined based on the temperature and pressure of the reservoir.

The second type of molecular beams are called supersonic jets.[53] In the case of supersonic jets, the orifice diameter is much larger than the mean free path of the molecules present in the beam source. This leads to large number of collisions taking place between the molecules upon expansion. The expansion of a supersonic jet usually takes place through a converging nozzle. The velocity ($v$) of such beams is usually above the speed of sound ($c = \sqrt{\gamma RT/m}$, where $\gamma$ is the heat capacity ratio) and thus termed supersonic. Thus, the velocity of the species present in the beam upstream from the nozzle is higher than the local speed of sound or the Mach number ($M = v/c$) is greater than 1.

The most important characteristic of a supersonic jet is the cooling of the internal degrees of freedom of the molecules caused by the high number of collisions occurring in the throat of the nozzle. This cooling of the molecules is the reason why supersonic jets are most commonly used in spectroscopic investigations. As the degrees of freedom (translational, rotational and vibrational) of the molecules are cooled, the respective spectral lines become sharp.

Another typical phenomenon observed in supersonic jet expansion is the clustering. In the context of molecular beams, clusters are small collection of molecules or atoms commonly bound together by van der Waals force. Thus size-dependent study of these aggregates also leads to understanding the evolution of different physical and chemical properties of the molecule/atom.

### 1.6.1. Molecular Beam Expansion of Supercritical Fluids

Combining the usage of supercritical fluids with supersonic jets has a number of advantages. Many organic molecules which are thermally labile are not compatible with the conventional techniques for transferring them into the gas phase, as these technique operate at higher temperatures. Supercritical fluids can be used in this case for the successful transfer of these molecules in the gas phase.

Christen et al.[15] observed extremely low temperatures on the molecular beam expansion from supercritical carbon dioxide and carbon monoxide and explained it on the basis of the high heat capacity ratios of supercritical fluids near the critical point. Dea et al.[24] characterized the cluster intensities and velocity distributions for the free jet expansion of supercritical carbon dioxide. They observed two dominant velocity peaks and assigned them as originating from condensed phase clusters of carbon dioxide. Christen et al.[13] observed typical distributions based on the aggregation state of the source and presented a thermodynamic model to explain the free jet expansions of high pressure gases, liquids and fluids. Since many physical properties become very sensitive to pressure and temperature when present near the critical point, the control of these conditions becomes very important. Christen et al.[16] developed a high pressure source with unprecedented thermodynamic stability. They were able to deduce a generalized picture which enabled the determination of the aggregation conditions in the reservoir before expansion by simply measuring the velocity distribution. These developments in the interesting phenomenon of cooling observed on free jet expansions of supercritical fluids has been reviewed recently.[12]

Supercritical fluids have also been used as an analytical tool by exploiting the property of supercritical fluids to dissolve solids. Hayes named the use of supercritical fluids for spectroscopy of organic molecules as 'Supercritical Fluid Spectroscopy' and reviewed it's usage in literature.[47] Randall et al.[98] successfully combined a dense gas chromatograph with a mass spectrometer to detect the transfer of organic molecules in the gas phase. Ming et al.[87,88] detected a number or biomolecules including adenine in the gas phase by using pulsed molecular beam expansion of supercritical ammonia. They observed clusters of the solute and solvent in the gas phase and explained it on the basis of strong hydrogen bonding between the solute and the solvent. Goates et al.[41] observed narrow spectral lines of polycyclic aromatic hydrocarbons upon molecular beam expansion of their solution in carbon dioxide. Quite recently Christen et al.[14,17] reported the mass spectrometric detection of a number of non-volatile organic molecules. Figure 1.5 depicts the temporal behavior of the signal of the molecular masses of caffeine and carbon dioxide upon pulsed expansion of a solution in supercritical state. Zhang et al.[127] used UV laser irradiation for ionizing a number of organic molecules including guanine and $C_{60}$, after transferring them in to the gas phase using carbon dioxide and carbon disulfide at high pressure. High resolution excitation spectra of an organic molecule, comparable to that achieved by using argon as carrier has been obtained by using molecular beam expansion from carbon dioxide in the supercritical state.[107]

The inability of using thermally labile molecules in a thermal evaporation source can be overcome by using a number of modern techniques. Matrix assisted laser desorption (MALDI) and Electrospray ionization (ESI) are the most commonly used techniques for such purposes. These techniques have very successfully been applied for studying organic molecules, but they have certain limitations. MALDI is limited by the choice of matrix and is mostly applicable to large bio-organic molecules, whereas ESI produces

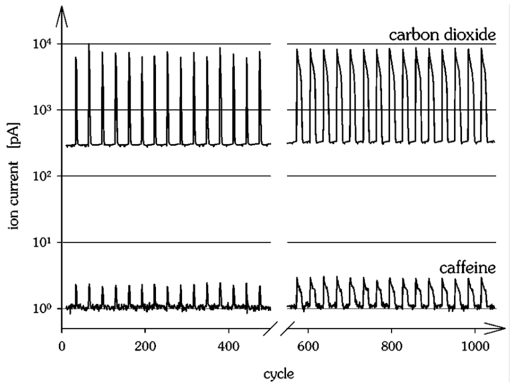

Figure 1.5.: Temporal behavior from the quadrupole residual gas analyzer for the pulsed expansion of caffeine in supercritical carbon dioxide.[14]

many multiply charged peaks which makes the interpretation of spectra complicated. SCFs can provide a viable alternative for studying the molecules that are otherwise incompatible with the above mentioned techniques.

## 1.7. Rapid Expansion of Supercritical Solutions

When a supercritical solution with a solid solute dissolved in it is expanded through an orifice, the solvent density decreases considerably and the solute is precipitated from the solvent. This process was first mentioned in a paper published in 1986 by Petersen et al.[90] as the Rapid Expansion of Supercritical Solutions (RESS). The fast reduction in density (on a scale of $\mu$s) results in uniform conditions and very high supersaturation ratios. This feature is very frequently used for production of nano to micro sized particles with very narrow distributions.

The RESS process is usually carried out in four steps as shown in Figure 1.6. In the first step, the solute is dissolved in the supercritical fluid. Then the required pre-expansion conditions are set just upstream from the expansion chamber. This solution is then expanded into a region of much lower pressure (ambient or low ambient conditions). The particles thus produced are recovered from the expansion chamber.

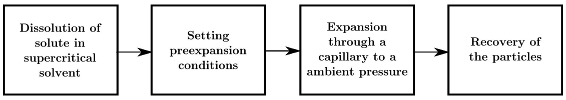

Figure 1.6.: The steps required for a RESS process.[113]

A parameter that is important in the context of solid formation from solution is called 'degree of supersaturation'. It is defined the ratio between the mole fraction of the solute at a certain temperature and pressure with the equilibrium mole fraction at the same location in the process.

### 1.7.1. Particle Formation using RESS

Nucleation followed by crystal growth is the basic mechanism of solid formation from a solution. The rate of these mechanisms is determined by concentration of the solute and degree of supersaturation. The particle size produced on precipitation from a solution is governed by a competition between the crystal growth and nucleation process. A higher degree of saturation will lead to nucleation taking over crystal growth and will thus produce smaller particles. Here lies the basic principle of formation of nano microsized particles using supercritical fluids. The high degree of supersaturation present on using the RESS process facilitates the production of such small particles.

The factors that ultimately affect the uniformity and the size of the particles produced are pre and post-expansion temperature and pressure, concentration of the solute, and the geometry of the nozzle orifice through which the solution expands.[117] A large amount of experimental work has been done dealing with the effect of these factors on the particle size. It has been observed that increase in the pre-expansion pressure and temperature leads to a increase in the average particle size.[78] The effect of post expansion pressure and temperature effect is also observed to have a similar but much less pronounced effect on the particle size and uniformity. Increase in mole fraction of the solute has also been known to decrease the particle size due to the fact that higher concentration leads to higher degrees of supersaturation.[78] Furthermore, the morphology of the particles can also be controlled by changing the expansion parameters. Particle morphology ranging from fibers to spheres can be observed on using RESS for particle production of different substances.[91]

Shaub et al.[106] developed a model for predicting the effect of these parameters on particle size. The model proposed also showed a decrease in particle size and uniformity on increasing the pre-expansion temperature or decreasing the pre-expansion pressure. Contrary to experimental evidence, their model predicted an increase in particle size upon increasing the mole fraction of the solute in the solution. They explained this discrepancy on the basis of an assumption used in the model, that no precipitation occurs inside the nozzle, which can be the case for long capillary nozzles used in the experiments.

The most prominent advantage of using RESS for material processing is the absence of any post production treatment of the particles. Since on expansion the supercritical fluid is automatically removed, no further purification is required. Secondly, the narrow and uniform size distributions obtained by RESS is useful in a number of fields. On the other hand, the disadvantages include the requirement of large amount of solvent because of low solubility of the solute. Furthermore, aggregation of the particles is also observed on using RESS for production of particles.[76,117]

## 1.8. Aim of the Work

The aim of this work is to exhibit the practicability of using supercritical fluids for transferring the biologically relevant nucleobases into the gas phase and also depositing them on surfaces to form thin particulate films. For this purpose, a SCF, namely ethylene will be used along with a cosolvent ethanol. Knowledge regarding the critical point of a mixture is a prerequisite for solubility studies. For this purpose the critical point of the binary mixture of ethylene and ethanol will be determined experimentally using a iterative bracketing method. As mentioned in Section 1.4.1 studying high pressure fluids pose great experimental challenges relevant to the materials, preparation and the apparatus which also needed to be tackled.

Using the results obtained regarding the critical point of the supercritical fluid, the nucleobases will be dissolved in it in the supercritical phase of the mixture. Molecular beam expansion from the solution will be used for the transfer and mass spectrometric detection of these nucleobases in the gas phase. Moreover, quantitative knowledge regarding the solubility of the nucleobases in the supercritical fluid will also be obtained. The solubility order thus obtained will also provide information relevant to solvation of these molecules in the SCF.

RESS will be used to form thin particulate films of these nucleobases on soda lime silicate glass. Morphological data regarding these deposits will be obtained using atomic force microscopy and compared with drop casting of solutions of the nucleobases in methanol.

It is expected that this study will lead to results that will successfully exhibit the practicality of using supercritical fluids for transferring non-volatile nucleobases into the gas phase and on surfaces.

## 1.9. Organization of the Thesis

The thesis is divided into five further chapters and the organization of the thesis is explained below.

Chapter 2 details the working and calibration of the experimental apparatus used for this work.

Chapter 3 discusses the results pertaining to the shift in the critical point of supercritical ethylene on addition of ethanol. Experimental results are reported and are fitted to an equation of state.

Chapter 4 reports on the dissolution and molecular beam detection of the nucleobases in the gas phase after dissolution in a solvent composed of supercritical ethylene with ethanol as cosolvent.

Chapter 5 pertains to results originating from the RESS process applied to the nucleobases dissolved in the supercritical fluid. Atomic force microscopy is used to image the morphology of the particles on soda lime silicate glass. The morphology is then compared with the particles formed using drop casting of the solutes from a methanol solution.

Finally, Chapter 6 provides a summary of the results obtained by this work along with an outlook on further possibilities.

# 2. Experimental

This chapter describes the operation and calibration of the experimental apparatus used in this work. It is divided into three major parts. The first part deals with the experiment to determine the critical co-ordinates (critical temperature $T_c$ and pressure $p_c$) of supercritical fluids and solutions. The second part deals with the experimental setup capable of producing and detecting supersonic molecular beams from supercritical fluids and solutions. The third part details the construction of the setup for performing thermal desorption spectroscopy.

## 2.1. Determination of Critical Co-ordinates

The apparatus described below utilizes a new bracketing method which uses the property of increased scattering of light at the gas-liquid phase boundary of ethylene for the detection of the critical co-ordinates.

### 2.1.1. Apparatus

A schematic representation of the experimental setup is given in Figures 2.1. Figure 2.2 shows a photograph of the sample cell.

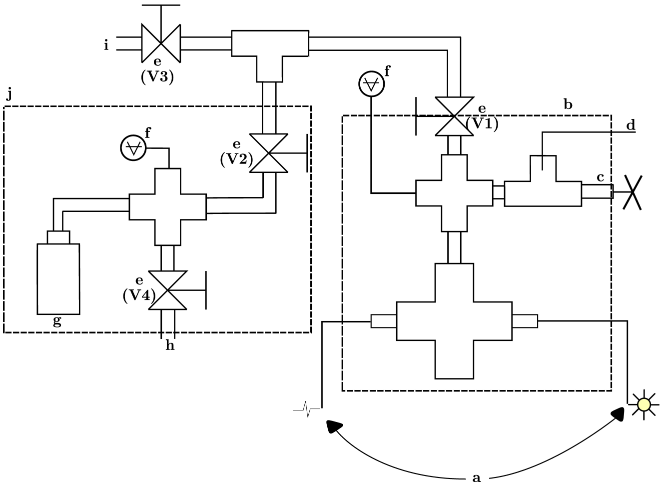

Figure 2.1.: Schematic diagram of the experimental setup. a: Fibers for UV-Vis source and detector, b: Sample cell, c: Pressure controller, d: Thermocouple, e: Valve, f: Pressure gauge, g: Autoclave, h: Fluid/Gas inlet, i: Fluid/Gas outlet, j: Mixing cell.

The setup has mainly two parts, i.e. the mixing cell and the sample cell. The mixing cell is connected to the gas reservoir and is used to prepare a mixture of known concentration of the solvent and cosolvent. This mixture is then transferred to the sample cell for detection of the phase boundary as explained in Section 2.1.3. The sample cell is a temperature controlled high pressure cell, which has quartz windows installed for spectroscopic purposes. It is immersed in the water bath of a circulator (Julabo Model 26). As the critical temperature of ethylene is 9.35 °C, cooling of the setup below room temperature is required to detect the gas-liquid phase boundary of ethylene. Cooling is accomplished by a recirculating chiller unit (National Labs, Model Proficool) which is connected to the water bath which contains the sample cell. The setup allows operation with an overall temperature stability of ±0.2 °C. The temperature stability is depicted in Figure 2.3 for different temperatures.

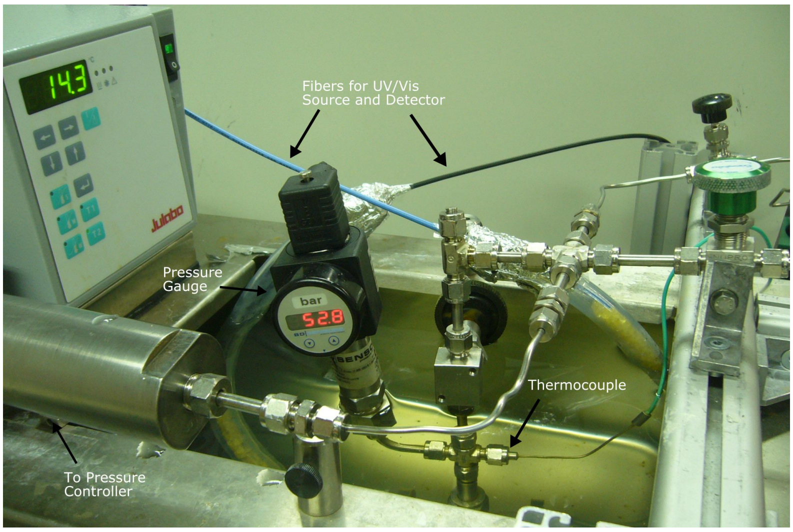

Figure 2.2.: A photograph of the sample cell in the water bath. The manual pressure controller was moved inside the water bath during the course of the measurements.

The fibers shown in Figure 2.1 are connected to the light source and the spectrometer for recording the transmission spectrum. These fibers are kept dry by using rubber tubes. The tubes contain silica gel to avoid unwanted scattering of light from water condensing on the windows of the high pressure cell at low temperatures. A manual pressure controller is attached to the high pressure cell to change the pressure at a constant temperature. A thermocouple, which is in direct contact with the fluid is used to measure the temperature. The thermocouple was calibrated using ice and also a pre-calibrated reference thermocouple. A temperature indicator (Eurotherm 2416) is used to display and record the temperature. The light source (Mikropak DH-2000 UV-Vis Lightsource) and the spectrometer (Stellarnet Inc. EPP 2000), which is connected to a computer are used to record the UV-Vis transmission spectra. The software (Spectrawiz) has the ability to record spectra in a mode known as 'Episodic Data Capture'. This mode automatically displays and records the full spectrum (190 nm to 850 nm) after a given time interval. For the experiments explained below, only the visible light source was used (350 nm to 850 nm).

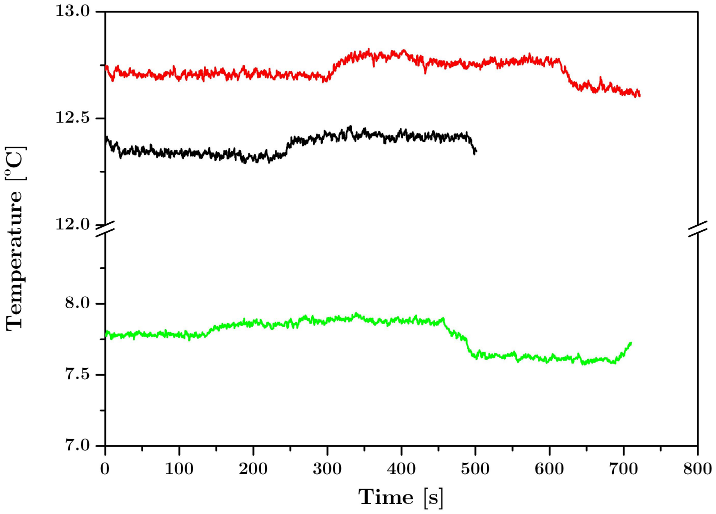

Figure 2.3.: Temperature stability as measured using the thermocouple inside the high pressure cell as a function of time.

### 2.1.2. Volume of the Mixing Cell

Determining the volume of the mixing cell is required to prepare solutions of known concentrations. The volume of the mixing cell was determined using a method involving known values of densities of ethylene at different pressures and temperatures. Another high pressure cell of known volume $V_1$ was connected to the mixing cell with an unknown volume $V_2$ with a valve in between, and the whole setup was evacuated using a vacuum pump. The valve between both cells was closed and ethylene was added to the unknown volume using the gas reservoir at a known initial pressure $p_i$ and temperature $T_i$. The pressure and temperature was noted and then the valve in between the cells was opened so that the pressure is reduced due to the fact that ethylene is now present in a larger volume $(V_1 + V_2)$. The volume change produced by the valve needle (which is used to open and close the valve) is exceedingly small as compared to the total volume and is not included in the calculation. The final pressure $p_f$ and temperature $T_f$ is noted. The densities of ethylene in both initial $(\rho_i)$ and final $(\rho_f)$ states are known and the unknown volume $(V_2)$ is then calculated as shown below.

$$\rho_i = \frac{m}{V_i} \qquad\qquad \rho_f = \frac{m}{V_f} \tag{2.1}$$

Since mass ($m$) remains constant after expansion, $V_i = V_2$ and $V_f = V_1 + V_2$, the following relation can then be derived.

$$\rho_i V_2 = (V_1 + V_2)\rho_f \tag{2.2}$$

$$V_2 = V_1\left(\frac{\rho_f}{\rho_i - \rho_f}\right) \tag{2.3}$$

Thus by using this process, a value of the unknown volume was determined for the high pressure cell used in this experiment. The volume of the mixing cell was found to be 76.1 ± 1.6 mL.

### 2.1.3. Experimental Procedure

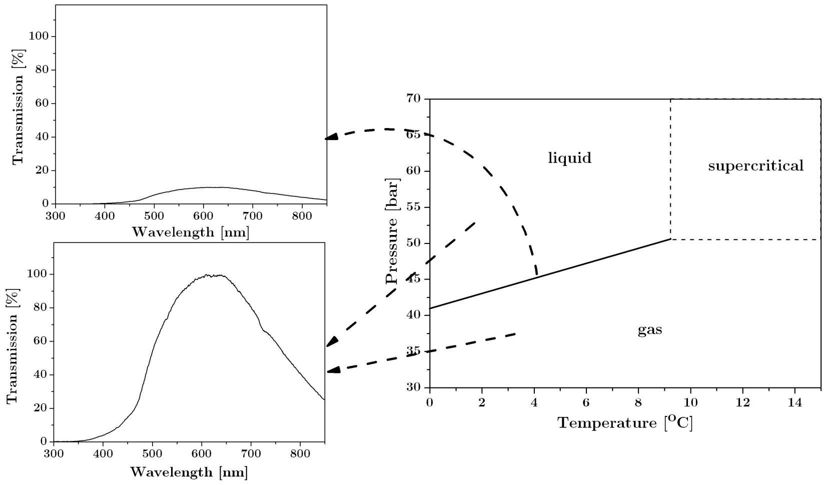

Figure 2.4.: Dependence of the transmission spectrum on the state of ethylene. The visible transmission spectrum (shown on the left-top) displays almost no transmission once the system is at the gas-liquid phase boundary, whereas a normal transmission spectrum (shown on left bottom) is recorded in the gas or liquid phase.

The required temperature is set on the water bath and the recirculating cooler is switched on at 0 °C. To speed up the process of cooling the water bath, ice can also be added directly to it. The cosolvent is added into the empty mixing cell and known concentration of the solution is prepared by adding ethylene by opening the valve V4 and then closing it upon reaching the required pressure. The pressure in the sample cell is then increased to the required initial pressure from the mixing cell by opening V1 and V2. After the temperature of the sample cell, which is being measured using the thermocouple, reaches the required temperature, episodic data capture is started using the software which records a full spectrum with a time interval of 500 ms. The pressure is increased by slowly rotating (one full turn per 5 seconds) the handles on the pressure controller clockwise. This will cause a slight change in the temperature (ca. 0.2 °C), observed in Figure 2.3. After the maximum pressure attainable by the pressure controller is reached, the handle bars are rotated anticlockwise to decrease the pressure. After reaching the initial pressure value, the episodic data capture will be stopped. Then the valves V1 and V2 are used to increase the pressure to the point of highest pressure attained during the last measurement and the above steps are repeated until the required pressure range for the particular temperature is scanned.

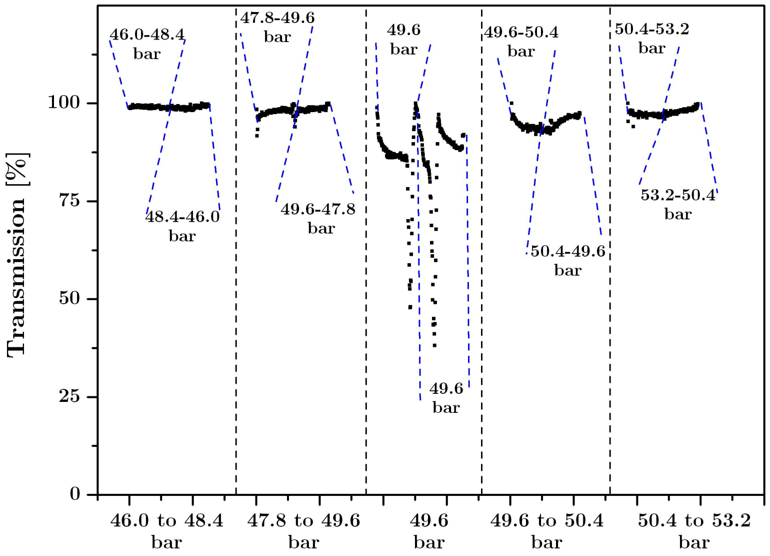

Figure 2.5.: The transmission measurements at an isotherm ($T$=9.0±0.2 °C) through the gas-liquid phase boundary. The pressure ranges given above and below the measurements are the ranges when the pressure was increased and decreased, respectively.

A dip in the transmission is observed at the gas liquid phase boundary, whereas once the fluid is in the supercritical state, the transmission does not change significantly during the measurement at that temperature. The software can be used to plot transmission at a single wavelength as a function of time. A suitable wavelength (600 nm is chosen because of high transmission at that wavelength) is selected and the data can be plotted against time. From this data, the transmission at different pressures for a single temperature is extracted and plotted. The high pressure cell is then depressurized to atmospheric pressure and is then connected to a vacuum pump to remove ethanol by pumping for 2-3 hours at an elevated temperature (∼30 °C).

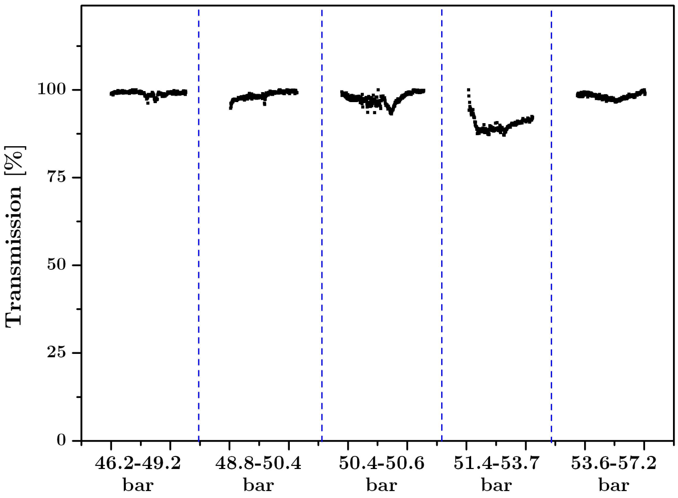

Figure 2.6.: Transmission measurement at an isotherm at $T$=10.0 ±0.2 °C. Absence of any significant amount of scattering indicates that the gas-liquid phase boundary is absent at this temperature.

Figures 2.5 and 2.6 depict the transmission measurements performed for ethylene indicating the undercritical and supercritical states, respectively. The pressure range (e.g. 46.0 to 48.4 bar) given in the x-axis of Figure 2.5 indicate the starting and the maximum pressure. The maximum pressure attainable using the manual pressure controller is reached in the middle of the measurement for the transmission curve for that particular pressure range. Then the pressure is decreased to the initial value to complete the pressure sweep. Similarly further scans were performed until scattering was observed at 49.6 bar. At this pressure, no change in pressure was observed while operating the manual pressure controller. This is explained by the fact that near the phase boundary, isothermal compressibility of ethylene is very high, thus a pressure change could not be induced by the limited range of the pressure controller. It is also evident from the plot that scattering is seen in both directions, i.e. while increasing and decreasing the pressure. This pressure value was assigned as the gas-liquid phase boundary at this temperature. On the other hand Figure 2.6 does not show any significant amount of scattering. This is because ethylene is now supercritical and the gas-liquid phase boundary is non-existent. Similar measurements were also made at $T$=9.5 ° C and no significant scattering was observed. This iterative bracketing method can thus be used to indirectly determine the critical point.

## 2.2. Molecular Beam Apparatus

A schematic diagram of the molecular beam machine is shown in Figure 2.7. The molecular beam apparatus consists of a high pressure cell connected via a pulsed nozzle to a vacuum system which contains an on-axis quadrupole mass spectrometer for beam detection.[14] A temperature controlled high pressure cell with a pulsed nozzle is used to produce supersonic molecular beams. The volume of the high pressure was calculated using the method described in Section 2.1.2. The nozzle is a commercially available Series 9 Pulsed Valve (General Valve) with a conical orifice of 0.5 mm. The pressure is measured using an industrial piezo-resistive stainless steel sensor (BDSensors DMP333) with 0.35% full scale (160 bar) accuracy. The quadrupole mass spectrometer (QMS) used for molecular beam detection is a residual gas analyzer (Balzers Prisma QMS 200) and has a maximum mass detection capability of 200 amu. The chamber also contains a surface manipulator which can be used for deposition of solutes on surfaces and is explained in detail in section 2.3.

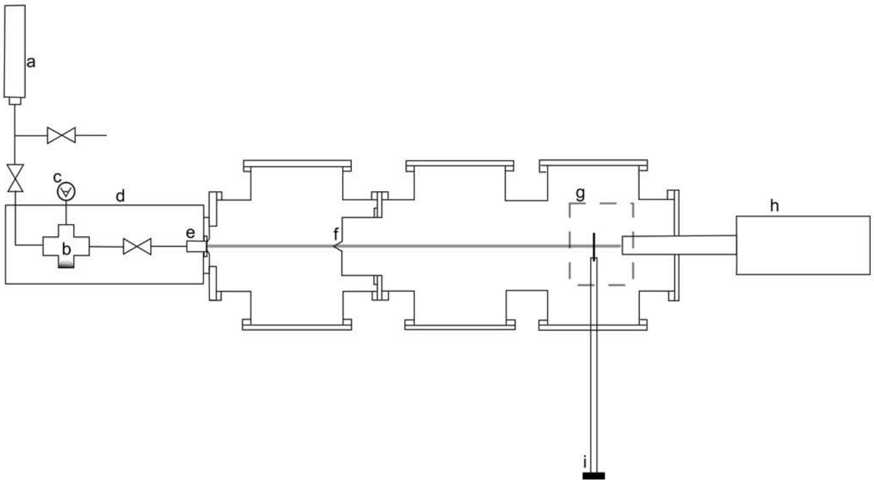

Figure 2.7.: Schematic diagram of the apparatus used for producing molecular beam. a: Solvent, b: Solute/Cosolvent, c: Pressure gauge, d: Temperature controlled high pressure cell, e: Pulsed nozzle (shown in detail in Figure 2.8), f: Skimmer, g: Surface holder (shown in detail in Figure 2.12), h: Quadrupole mass spectrometer, i: Surface manipulator.

### 2.2.1. Vacuum Chambers

The vacuum chambers, namely, the expansion chamber and the detection chamber are pumped separately using two different types of pumps. The expansion chamber is pumped using a Diffstak Diffusion pump with a pumping speed of 1000 l/s. The high pumping speed is necessary for this chamber to maintain a vacuum ($\approx 10^{-6}$ mbar) after the high flux of the pulsed molecular beam. The second chamber which is separated using a conical skimmer (5 mm diameter) is pumped using a turbomolecular pump.

### 2.2.2. High Pressure Cell

High pressure (10-200 bar) is maintained in the current setup using mainly stainless steel fittings and sealings provided by Swagelok. The stainless steel fittings use conical metal sealing which are inert with respect to all the chemicals used in the experiments. A Novaswiss pressure gauge was used to determine the pressure inside the high pressure cell. Temperature control was achieved using a combination of water bath and band heater. The band heater is isolated using aluminium foil to reduce the loss of heat. Due to the error given by the band heater the overall temperature is maintained with an accuracy of ±3 °C.

### 2.2.3. Nozzle

The pulsed nozzle is a General Valve Series 9 pulsed nozzle which by default is able to work up till atmospheric pressure. The nozzle was modified so that it is able to produce pulsed beams with a backing pressure of up to 150 bar which is more than two orders of magnitude than the original value. Shown in Figure 2.8 is a schematic diagram of the nozzle. The spring holds the poppet in place to seal the nozzle opening. A sealing foil made of Kapton is used in between the poppet and the nozzle opening. The nozzle produces beams using a poppet which is controlled using a magnet as shown in the Figure 2.8.

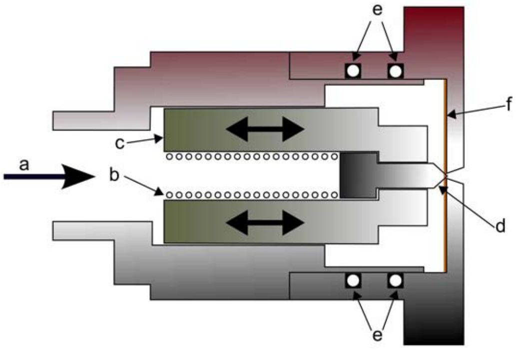

Figure 2.8.: Schematic diagram of the nozzle. a: Solution inlet, b: Spring, c: Magnet, d: Poppet, e: O-Rings, f: Kapton sealing.

### 2.2.4. Molecular Beam Detection

The QMS used is capable of recording the signal in two modes, Analog Scan and Multiple Ion Detection (MID) mode. The analog scan records the mass spectrum of a range of masses specified whereas the Multiple Ion Detection (MID) mode can be used to monitor single masses.

#### Multiple Ion Detection (MID)

MID mode is useful in detecting the behavior of different ions as a function of time. Specifically in the detection of molecular beams, which contain a range of molecules or atoms, the MID mode can be useful for comparing the amount present in the beam. Figure 2.9 depicts the molecular beam expansion of ethylene and shows that reproducible molecular beams are detected.

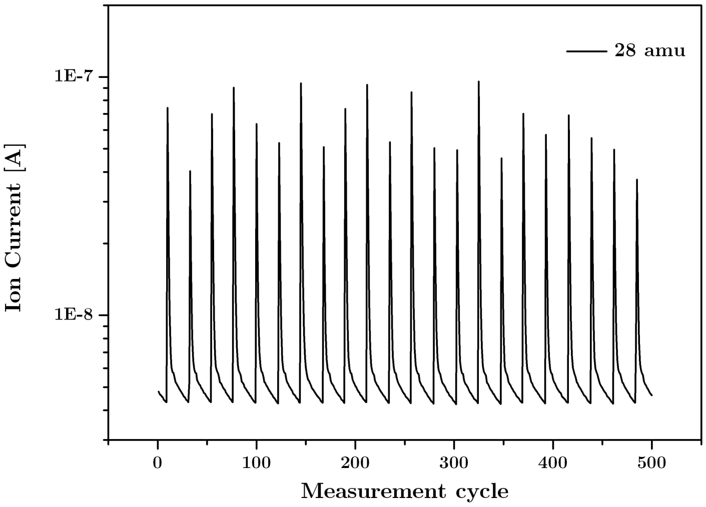

Figure 2.9.: Temporal behavior recorded using the QMS in the MID mode. The figure shows pulses of ethylene at $p$=72.6 bar and $T$=40 °C.

MID is a very practical mode to be used for sampling the evolution of single masses as a function of time. The challenge faced while using MID mode is that it provides no information on the maximum of a particular mass peak. Furthermore, because of the difference in the time constants of the QMS and nozzle, amplitude oscillations are observed which translate into large error bars when quantitative analysis is required.

Furthermore, using MID it was not straightforward to account for the neighboring masses during quantitative calculation. Shown in Figure 2.10 is the temporal behavior of the expansion of a solution of adenine in ethylene and ethanol. It not only shows a peak at the molecular ion of adenine (135 amu) but also a comparable peak at mass 137 amu which does not originate from adenine.

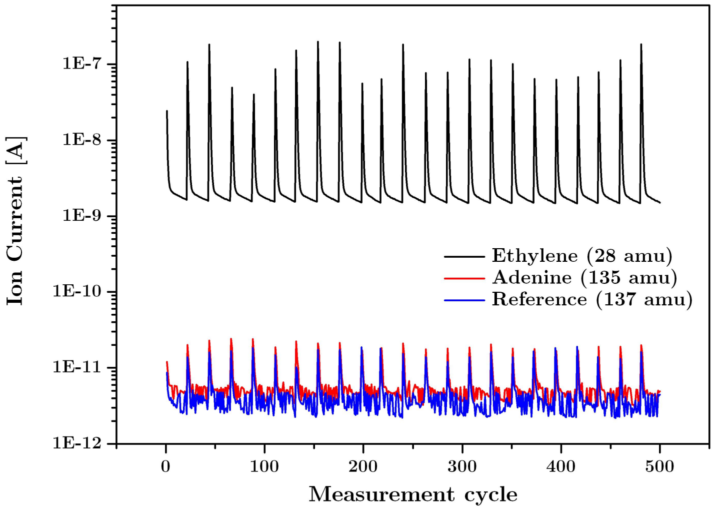

Figure 2.10.: Temporal behavior of the molecular masses of ethylene, adenine and a reference mass while pulsing at 0.1 Hz, a solution of adenine in ethylene and ethanol (3%) at $p$=74.2 to 74.4 bar and $T$=40 °C.

### Analog Scan

Analog scan can be used to record the mass spectrum of a specified range of masses. It can be combined with the pulsed molecular beam by measuring at a slow scan rate so that the molecules present in the beam are detected. It is also used to record background mass spectrum. Figure 2.11 depicts the mass spectrum of the background present in the vacuum chambers. The rest gas spectrum shows peaks originating from background with a major peak present at 18 amu denoting water desorbing from the chamber walls. Analog scan is very helpful while scanning a range of masses close to each other. Furthermore, while operating this mode at slower speed (60 s/amu), multiple pulses can be summed to detect a signal which cannot be detected in a single pulse. This method improves the overall errors in the quantitative analysis because of the slow scan rate of

| | | | |
|---|---|---|---|
| Ion Reference | 130 V | Extract | 5 V |
| Cathode | 85 V | Filament Current | 1.50 mA |
| Focus | 10 V | Resolution | 50 |
| Field Axis | 5 V | SEM | 1100 V |

Table 2.1.: Ion source settings for the QMS used for the analog scans.

the QMS. It can provide information regarding the peak maximum and can be used for quantitative analysis as described in the Appendix. The ion source settings used for the analog scans in this work are given in Table 2.1.

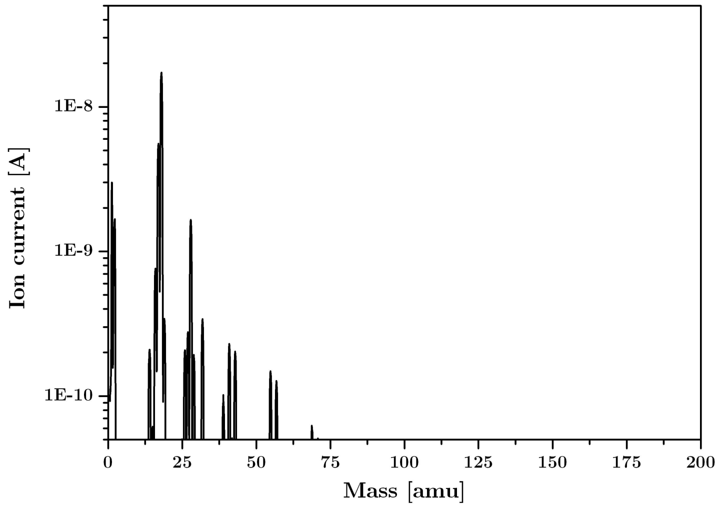

Figure 2.11.: Rest gas mass spectrum of the background present in the vacuum chambers. Background pressures in the expansion and detection chamber were $1.8 \times 10^{-6}$ and $3.8 \times 10^{-6}$ mbar, respectively.

## 2.3. Temperature Programmed Desorption Setup

### 2.3.1. Apparatus

A detailed schematic representation of the temperature programmed desorption setup is shown in Figure 2.12, which includes an enlarged view of the section denoted as 'g' in Figure 2.7. The substrate is held mechanically on top of the surface holder using a copper plate with screws. The surface manipulator has the capability of translational as well as rotational movement. The translational motion allows the surface to be moved either in or out of the path of the molecular beam. The surface can also be rotated to face either the molecular beam for deposition or the QMS for desorption experiments. The surface is kept in a fixed position at $\sim$ 5 cm from the QMS.

### 2.3.2. Linear Temperature Ramps

Linear ramps are obtained by regulating the wattage of a 150W bulb using a PID controller (Eurotherm 2416). The bulb heater is in direct contact with the surface holder as shown in the Figure 2.12. A flexible copper strand connected to a liquid nitrogen cold

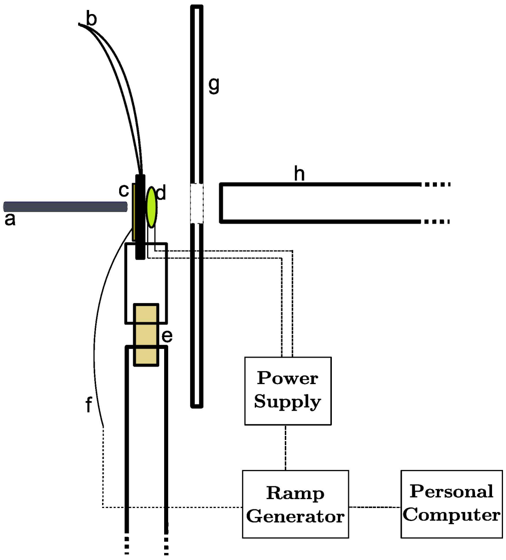

Figure 2.12.: Schematic diagram of the apparatus. a: Molecular beam, b: Copper strand attached to liquid nitrogen cold trap, c: Substrate, d: Heating bulb, e: Machinable ceramic slab, f: Thermocouple, g: Shield, h: QMS.

trap is clamped to the surface holder using copper plates between the heating bulb and the surface to permit a wider range of the temperature. The cold trap allows cooling down of the surface to ∼ -100 °C. The surface holder is thermally decoupled from the rest of the translator using a MACOR (machinable ceramic) slab as shown in the Figure 2.12. Linear ramps of up to 0.5 K/s can be carried out up till a temperature of 300 °C. Figure 2.13 shows the linear ramps at different scan rates whereas Figure 2.13 shows the complete ramp with a linear fit and the spread of the temperature around it.

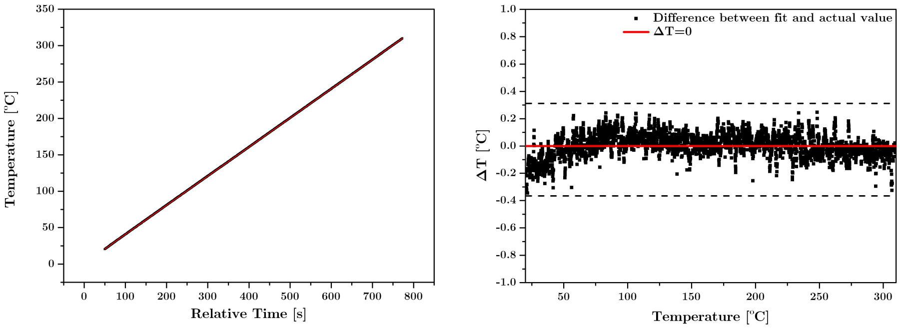

(a)

(b)

Figure 2.13.: Linearity of the temperature ramp (a) is shown by the spread of temperature around the ideal value (b).

### 2.3.3. Measurement of Thermal Desorption Spectra

A shield is placed between the QMS ion source and the surface. The shield is placed directly in front of the surface and has a 5mm diameter hole. The purpose of the shield is to minimize the probability of detecting unwanted species that do not originate from the substrate.

#### Molecular Beam Deposition

The surface can be rotated to face the molecular beam using the surface translator. For molecular beam deposition, the solute was dissolved in the high pressure cell at the required stagnation conditions. The vacuum chambers were evacuated and the surface was cooled to a temperature of -10 °C. Pulsed molecular beams were then produced using the nozzle which caused the solute particles to precipitate and deposit on the surface. After deposition the surface was rotated so that it faced the quadrupole mass spectrometer and a temperature ramp was generated to record the thermal desorption spectrum.

# 3. Binary Mixtures of Supercritical Fluids

The determination of the critical co-ordinates (critical temperature $T_c$ and pressure $p_c$) is imperative in studies involving solubility of a solute in the supercritical fluid. As adding a cosolvent to a supercritical fluid will shift the critical point of the solution, knowledge regarding the new critical point is important in solubility studies involving that solvent. The change in the critical co-ordinates not only depends on the critical properties of the species involved but also on the interactions between them. This chapter deals with the determination of the shift in the critical co-ordinates of ethylene on the addition of ethanol. The Soave Redlich Kwong Equation of State (SRK-EOS) is used to fit the experimental data.

## 3.1. Supercritical Ethylene

Table 1.1 shows the different physical properties of supercritical ethylene. It is a non-polar molecule with an unsaturated $\pi - \pi$ bond. It's relatively easy to reach the supercritical state of ethylene in the laboratory, as it essentially is present in the supercritical state in the bottle in which it was delivered.

### 3.1.1. Determination of Critical Co-ordinates of Pure Ethylene

Initially the apparatus described in section 2.1.1 was used to determine the critical point of ethylene for calibration purposes. Measurements were performed for pure ethylene according to the bracketing method described in section 2.1.3. Figure 2.5 shows the scattering of light at the gas-liquid phase boundary for ethylene and Figure 2.6 displays the absence of significant scattering once the temperature is above the critical temperature. Figure 3.1 shows a plot of pressure and temperature indicating the points at which scattering was observed.

The experimental points displayed in Figure 3.1 have already been corrected by 0.4 bar to match the literature value of the gas liquid boundary of ethylene (obtained from NIST fluid data). As the thermocouple measuring the temperature has already been calibrated, the pressure (instead of temperature) was shifted to match the data. Thus, the shift also served the purpose of the calibration of the pressure gauge. The dashed line displayed in Figure 3.1 signifies the temperature at which no scattering was observed.

An approximation was made at this point that, in the small pressure and temperature range, the behavior of the phase boundary is linear. A linear extrapolation is made up till the dotted line, which allowed the determination of the critical point of ethylene. The critical temperature was determined to be lying between 8.6 to 9.5 °C and the critical pressure was $> 50.0$ bar.

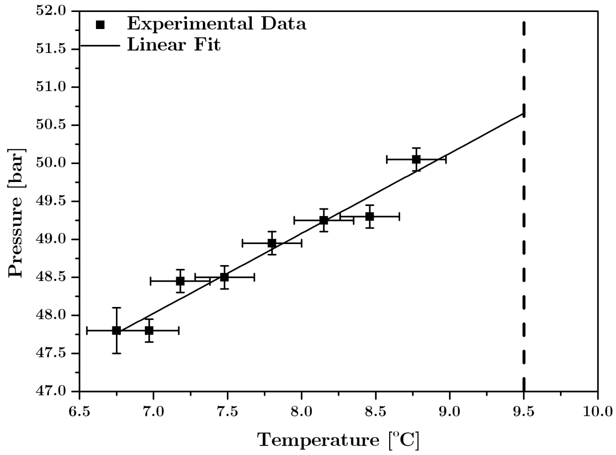

Figure 3.1.: Experimental phase diagram of pure ethylene. The dashed line denotes the temperature at which no scattering was observed.

## 3.2. Mixture of Ethylene and Ethanol

Studies involving supercritical ethylene and alcohols are mainly concerned with the phase equilibrium at higher temperature ( $> 293$ K)[36,43] and are not that common at lower temperatures.[61] Even then, the studies are limited to values of critical pressure, and values of critical temperature as a function of ethanol mole fraction are not reported. The following results mainly concern the shift in critical co-ordinates on addition of very small amounts of ethanol with mole fractions of less than 6%.

The basic experimental principle remains the same as for pure ethylene. On addition of small amounts of ethanol, the critical point of the mixture shifts slightly. This is evident by the presence of a gas-liquid phase boundary (see Figure 3.2) at temperatures higher than the critical temperature of pure ethylene. The increase in the critical co-ordinates is evident, as the critical co-ordinates of ethanol are higher than that of ethylene (Table 1.1). Five different concentrations were measured up till a mole fraction of 0.054 of ethanol. Given below are results for the five measurements.

### 3.2.1. 0.010 and 0.019 Mole Fraction of Ethanol

On addition of ethanol, measurements made at temperatures higher than the critical point of ethylene showed scattering as displayed in Figure 3.2.

Figure 3.2 is a plot of transmission as a function of pressure and is composed of three separate measurements. The pressure change induced by the manual pressure controller is dependent on the volume of the cell and also temperature and pressure of the fluid. In each of the three measurements displayed in Figure 3.2, the pressure is increased and decreased using the manual pressure controller. The steps shown approximately in

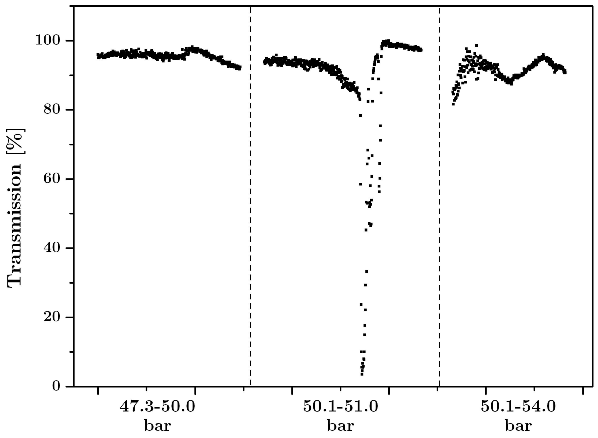

Figure 3.2.: Transmission measurement through an isotherm ($T$=9.5 °C) for ethylene with 0.010 mole fraction of ethanol. The pressure range measured was $p$=47.3 to 54.0 bar.

the middle of the measurements are seen when the maximum pressure attained using the manual pressure controller has been reached. Furthermore, small oscillations in the transmission are also seen during the measurements, mainly because of fluctuations in the power of the light source.

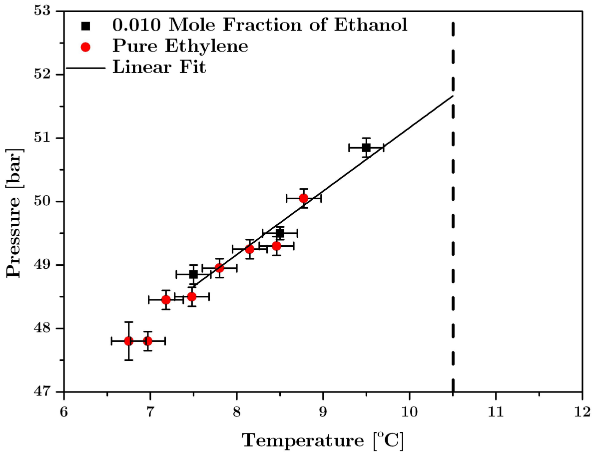

Figure 3.3.: Experimental phase diagram of ethylene with ethanol (0.010 mole fraction). The dashed line denotes the temperature at which no scattering was observed.

Similar measurements were made at higher temperatures. The temperature at which no scattering was observed on changing the pressure signifies the absence of a gas-liquid phase boundary. The temperatures at which measurements were performed include 7.5, 8.5, 9.5, and 10.5 °C. Figure 3.3 shows the pressure at which scattering was observed. For reference purposes, the phase boundary of pure ethylene is also given. The dashed line at $T$ = 10.5 °C denotes the temperature at which no scattering was observed on changing the pressure. The critical temperature was found to lie between 9.2-10.5 °C and the critical pressure was found to be > 51.0 bar.

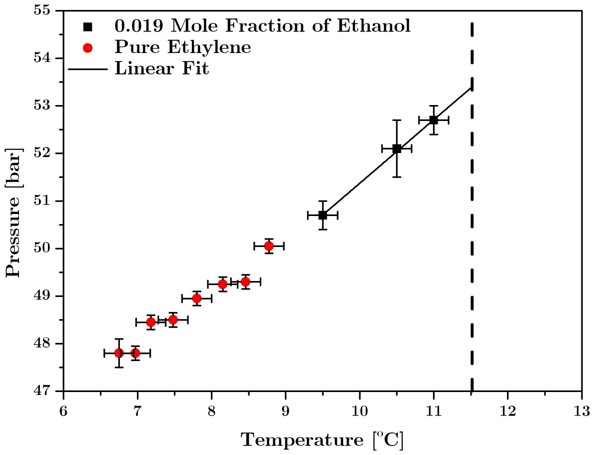

Figure 3.4.: Experimental phase diagram of ethylene with ethanol (0.019 mole fraction). The dashed line denotes the temperature at which no scattering was observed.

Transmission through the mixture was measured at higher temperatures to determine the critical point for the mixture containing 0.019 mole fraction of ethanol. Measurements at this concentration were made at 9.5, 10.5, 11.0, and 11.5 °C. Figure 3.4 shows the phase diagram for the mixture along with a dotted line which represents the temperature at which no scattering was observed. Critical co-ordinates determined from the graph are $T_c$ = 10.8-11.5 °C and $p_c$ > 53 bar.

### 3.2.2. 0.031 and 0.039 Mole Fraction of Ethanol

The temperatures at which scattering experiments were performed for 0.031 mole fraction of ethanol are 11.5, 12.5, 13.5, and 14.0 °C. Figure 3.5 shows the scattering observed at $T$=13.5 °C. The phase diagram based on the experiments is plotted in Figure 3.6 along with the dotted line indicating the temperature at which no scattering was observed. Critical co-ordinates of the mixture are $T_c$ = 13.3-14.0 ° C and $p_c$ > 54.4 bar. The phase diagram for the solution containing 0.039 mole fraction of the ethanol is depicted in Figure 3.7. The critical co-ordinates were calculated to be $T_c$= 13.3-14.5 °C and $p_c$ > 54.4 bar.

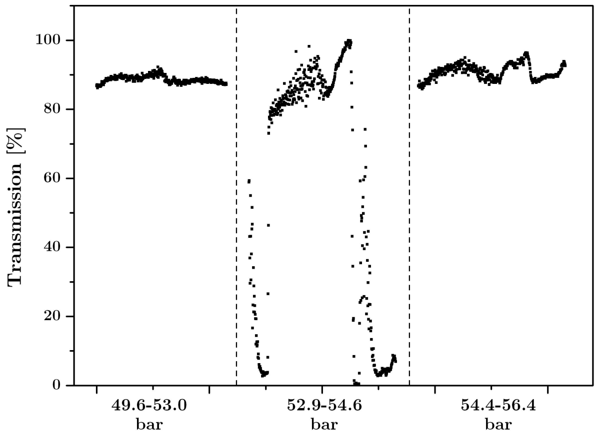

Figure 3.5.: Transmission measurement through an isotherm ($T$=13.5 °C) for ethylene with 0.031 mole fraction of ethanol. The pressure range measured was $p$=49.6 to 56.4 bar.

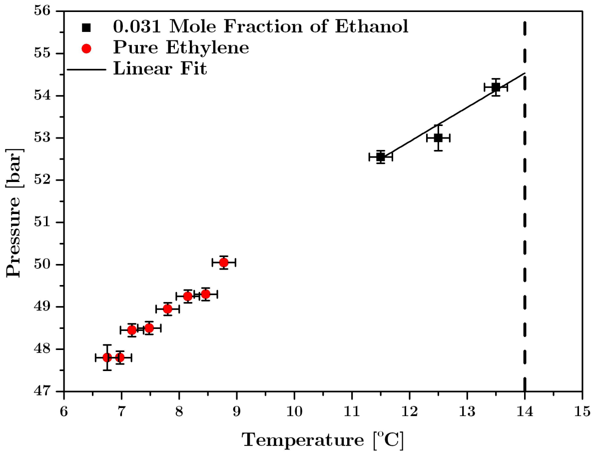

Figure 3.6.: Experimental phase diagram of ethylene with ethanol (0.031 mole fraction). The dashed line denotes the temperature at which no scattering was observed.

### 3.2.3. 0.054 Mole Fraction of Ethanol

Similar to the previous measurements, scattering at different isotherms was recorded for solution containing 0.054 mole fraction of ethanol. The temperatures at which the experiments were performed were $T$ = 12.5, 13.5, 14.5, and 15.5 °C.

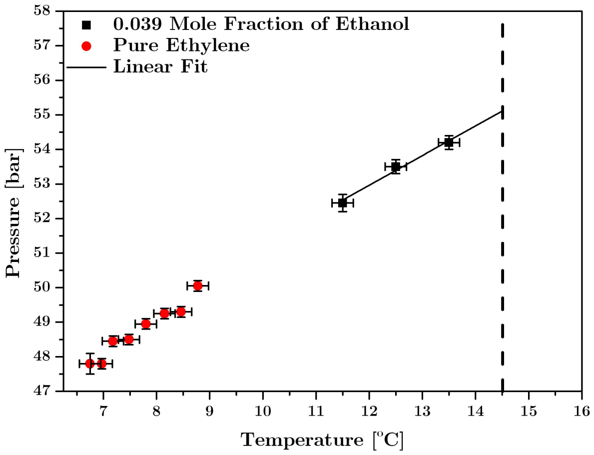

Figure 3.7.: Experimental phase diagram of ethylene with ethanol (0.039 mole fraction). The dashed line denotes the temperature at which no scattering was observed.

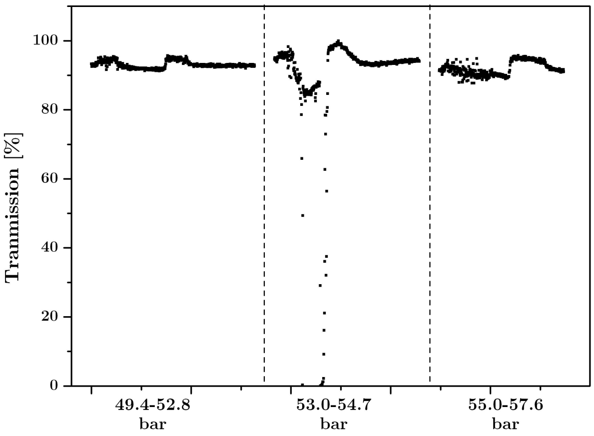

Figure 3.8.: Transmission measurement through an isotherm ($T$=13.5 °C) for ethylene with 0.054 mole fraction of ethanol. The pressure range measured was $p$=49.4 to 57.6 bar.

Figure 3.8 shows scattering at the gas-liquid phase boundary for the mixture at $T$ = 13.5 °C. Figure 3.9 shows the phase boundary for this concentration of ethanol. The critical co-ordinates are calculated to be $T_c$ = 14.3-15.5 °C and $p_c$ > 55.5 bar.

The experimental results obtained are summarized in Table 3.1.

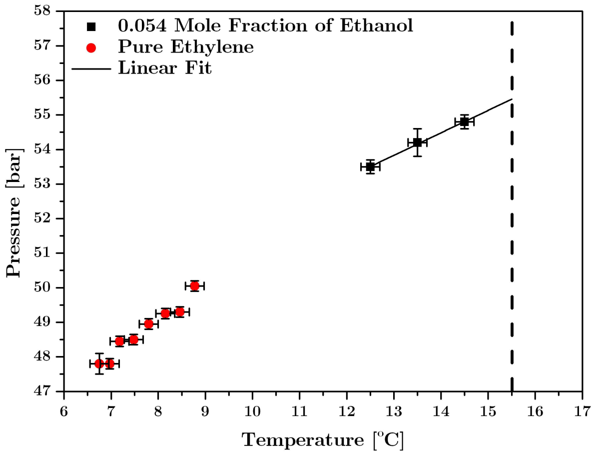

Figure 3.9.: Experimental phase diagram of ethylene with ethanol (0.054 mole fraction). The dashed line denotes the temperature at which no scattering was observed.

| **Mole Fraction** | $T_c$ **(°C)** | $p_c$ **(bar)** |
|---|---|---|
| $0.010 \pm 2.7 \cdot 10^{-4}$ | 9.2-10.5 | $> 51.0$ |
| $0.019 \pm 2.7 \cdot 10^{-4}$ | 10.8-11.5 | $> 53.0$ |
| $0.031 \pm 7.9 \cdot 10^{-4}$ | 13.3-14.0 | $> 54.4$ |
| $0.039 \pm 7.4 \cdot 10^{-4}$ | 13.3-14.5 | $> 54.4$ |
| $0.054 \pm 2.1 \cdot 10^{-3}$ | 14.3-15.5 | $> 55.5$ |

Table 3.1.: Summary of the results obtained for the critical co-ordinates of the mixture.

## 3.3. Shift in Critical Point using an EOS

The calculation of phase equilibrium of multi-component system is crucial in design of distillation and extraction equipment. By use of theoretical methods, one can have phase equilibrium data for multicomponent system. The key method of calculating phase equilibrium is the use of an equation of state. There exist a number of advanced equations of state which provide data for different types of systems as described in Section 1.4.2. These equations of state are also used for the determination of the shift in the critical co-ordinates of multicomponent systems.

### 3.3.1. Soave Redlich Kwong Equation of State

The equation of state chosen for the system under question (ethylene and ethanol) is the Soave Redlich Kwong Equation of State (SRK-EOS).[109] This equation was chosen because of the fact that previously, it has been successfully used to fit experimental data of the phase equilibrium of a number of alcohols[45,61,63,64] with ethylene. Furthermore, it has also been applied to a number of hydrocarbon mixtures[4] by combining it with the work of Gualtieri et al.[42] For ethylene and ethanol, the method proposed by Anselme et al.,[4] which is applicable to multi-component systems, has been applied by limiting it to a binary system.

A dilute binary mixture is mainly composed of one species, in our case it would be the solvent ethylene and is denoted by index 1 and the mole fraction $x_1$. The second component (the cosolvent) is present in very low concentration (1-6 mole fraction percent) and is denoted by subscript 2 and mole fraction $x_2$.

The equation of state proposed by Redlich Kwong[100] has been modified by Soave[109] by making the previously temperature independent parameter '$a$' to be temperature dependent, as shown below.

$$p = \frac{RT}{v-b} - \frac{a(T)}{v(v+b)} \tag{3.1}$$

Using the SRK-EOS in conjunction with Anselme et al.,[4] the critical temperature and volume of a dilute binary system is given as:

$$\begin{aligned} T_c = T_{c1}\Bigg\{1 + \frac{x_2}{1+M_1}\Bigg[&0.25666\left(\frac{b_2}{b_1}\right)^2 + 2.26989\left(\frac{a_{12}}{a_{11}}\right)^2 \\ &- 1.52654\left(\frac{a_{12}b_2}{a_{11}b_1}\right) + 0.01323\left(\frac{b_2}{b_1}\right) - 1.01322\left(\frac{a_{12}}{a_{11}}\right)\Bigg]\Bigg\} \end{aligned} \tag{3.2}$$

$$\begin{aligned} v_c = v_{c1}\Bigg\{1 + x_2\Bigg[&1 - 0.14952\left(\frac{b_2}{b_1}\right)^3 + 3.93341\left(\frac{a_{12}}{a_{11}}\right)^3 \\ &+ 0.11973\left(\frac{b_2}{b_1}\right) + 0.27207\left(\frac{b_2}{b_1}\right)^2 + 0.03044\left(\frac{a_{12}}{a_{11}}\right) \\ &- 2.65661\left(\frac{a_{12}}{a_{11}}\right)^2 - 3.96793\left(\frac{a_{12}^2 b_2}{a_{11}^2 b_1}\right) + 1.33421\left(\frac{a_{12}b_2^2}{a_{11}b_1^2}\right) \\ &+ 0.08420\left(\frac{a_{12}b_2}{a_{11}b_1}\right)\Bigg]\Bigg\}^{-1} \end{aligned} \tag{3.3}$$

The parameters $a_{ii}$ and $b_i$ for the pure component are given by:

$$a_{ii} = 0.42747\frac{R^2T_{ci}^2}{P_{ci}}\alpha_i(T) \tag{3.4}$$

and

$$b_i = 0.08664\frac{RT_{ci}}{P_{ci}} \tag{3.5}$$

where

$$\sqrt{\alpha_i(T)} = 1 + M_i(1 - \sqrt{T_{ri}}) \tag{3.6}$$

with

$$M_i = 0.480 + 1.574\omega_i - 0.176\omega_i^2 \tag{3.7}$$

$T_{ci}$, $p_{ci}$ and $\omega_i$ are the critical temperature, critical pressure and the acentric factor of component $i$, respectively and $T_{ri} = T/T_{ci}$ is the reduced temperature. $T_c$ and $v_c$ are the critical temperature and volume of the mixture and $T_{c1}$ and $v_{c1}$ are the critical temperature and volume of pure ethylene.

The mixing rules used for the component parameters are:

$$a_{12} = \sqrt{a_{11}a_{22}}(1 - k_{12}) \tag{3.8}$$

where $k_{12}$ is known as the binary interaction parameter. Equation 3.2 can be used to calculate the critical temperature and the critical volume of the mixture. Using $T_c$ and $v_c$ in the SRK-EOS (Equation 3.1), the critical pressure of the mixture can then be calculated. In which case:

$$a = \sum_i \sum_j x_i x_j a_{ij} \tag{3.9}$$

$$b = \sum_i \sum_j x_i x_j b_{ij} \tag{3.10}$$

where

$$b_{12} = \frac{b_1 + b_2}{2} \tag{3.11}$$

and $b_{11} = b_1$ and $b_{22} = b_2$. The value of different physical properties of the components used are given in Table 1.1.

### 3.3.2. Critical Co-ordinates of Mixture of Ethylene and Ethanol

Using the method described above, a fit was made using the experimental data of the critical pressure and temperature of mixture of ethylene and ethanol. Displayed in Figure 3.10 is the experimentally determined critical temperature of ethylene as a function of the mole fraction of ethanol. It shows a comparison between the experimental measurements and the fit to the SRK-EOS. The binary interaction parameter $k_{12}$ for the fit is 0.113±0.007. It is evident from the figures that the theoretical fit is fairly in agreement with the experimental data of the behavior and value of the critical co-ordinates of the mixture on addition of ethanol.

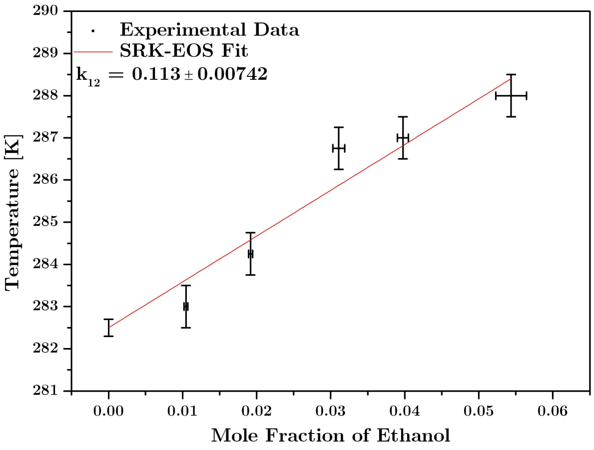

Figure 3.10.: Shift in critical temperature of ethylene as a function of ethanol mole fraction.

## 3.4. Discussion

The obtained experimental data show a significant increase in the critical temperature of the mixture on addition of very small amounts of ethanol. The SRK-EOS was used to derive the binary interaction parameter ($k_{12}$) from the experimental data. The binary interaction parameter is independent of temperature, pressure and composition[109] and serves mainly as an adjustable empirical parameter. The interpretation of the binary interaction parameter is based on the difference of the value from zero. A higher value of the binary interaction parameter suggests a stronger interaction between the unlike molecules.

One should be careful while comparing the binary interaction parameter obtained by different systems. The form of the mixing rule used determines the absolute value of the binary interaction parameter. Strictly speaking, it is an empirical parameter to account for the difference observed between theoretical and experimental data. Bartle et al.[7] proposed a purely theoretical correlation to predict the value of $k_{12}$ of a binary system. The formula for the estimation is:

$$k_{12} = 0.51B; \qquad B = A(\omega_2 - \omega_1)\left(\frac{\nu_{c2}}{\nu_{c1}}\right)\left(\frac{p_{c2}}{p_{c1}}\right)^2 \tag{3.12}$$

where $A$ is a parameter which is 1/2 when compounds containing -OH groups are involved and 1 for other compounds. The value of $k_{12}$ thus calculated contains a typical error of 0.015. The properties available in Table 1.1 were used to calculate the value of $k_{12}$, which is equal to 0.281. This value which is higher than the one reported in section

3.3.2 ($k_{12}$=0.112) but has an even larger deviation from the one reported in literature,[61] which is -0.0057.

| **Alcohol** | $k_{12}$ |
|---|---|
| Methanol[45] | -0.0417 |
| Ethanol[61] | -0.0057 |
| 1-Propanol[62] | 0.0154 |
| 2-Methyl-1-Propanol[64] | 0.0379 |
| 1-Butanol[63] | 0.0224 |

Table 3.2.: Values of binary interaction parameters for the binary mixture of ethylene with different alcohols.

Table 3.2 shows the binary interaction parameters of different alcohols found in literature. The value calculated in this work deviates from the value found in literature. It has been reported in literature[101] that the binary interaction parameter can differ depending on the type of equilibria under consideration e.g. gas-gas, gas-liquid. This can originate from the fact that depending on the phases of the components, some new types of interactions can occur, or some can be absent which can then effect the binary interaction parameter. This can also explain the discrepancy seen in the value of the binary interaction parameter given in this work and the one reported in literature.[61]

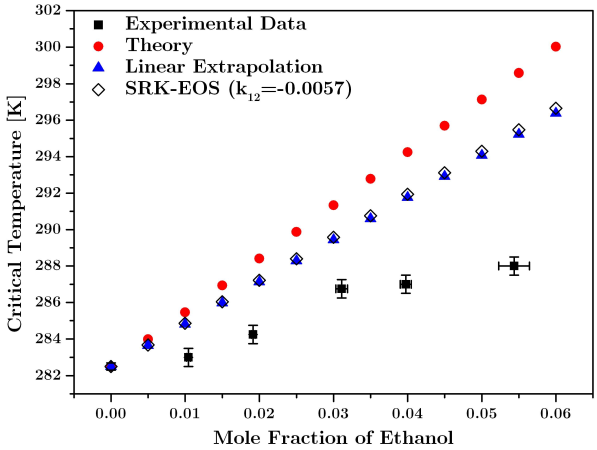

Figure 3.11.: Comparison of different methods to determine/estimate the critical temperature of mixtures. The methods include the one proposed by Liu[71] and using the SRK-EOS with a $k_{12}$=-0.0057.[61] The linear extrapolation is simply an average of $T_c$ depending on the mole fractions.

The prediction of the critical co-ordinates using an equation of state requires experimental data. Methods which do not require experimental data for the prediction of the critical co-ordinates also exist in literature. For example, Liu[71] proposed a method for determining critical temperature and pressure of multicomponent mixtures by using only the properties of pure components.

Figure 3.11 compares the method proposed by Liu[71] and linear extrapolation with the experimental data. It clearly shows that the critical temperature is overestimated in both of the cases even at such low concentrations. In the case of using the $k_{12}$ value provided in literature,[61] the values obtained are also much higher than the one reported in this work.

Thus, it can be concluded that before more reliable theoretical methods are developed, experimental determination of the critical co-ordinates is required.

# 4. Molecular Beam Expansion of Nucleobases

The main objective of this chapter is to use supersonic molecular beam expansion to transfer non-volatile organic molecules into the gas phase, namely the five bio-organically relevant nucleobases. The scientific goal is to learn about the solubility of the nucleobases in the supercritical solvent. These bases have a vanishingly low vapor pressure [18,40] and guanine and cytosine have a tendency to dissociate at elevated temperatures. [55] Ethylene was used as solvent in the supercritical phase with ethanol as a cosolvent. This chapter reports on the results from the molecular beam expansion of solutions of nucleobases in supercritical ethylene with ethanol as cosolvent.

## 4.1. Selection of Solvent

In the supercritical fluid research field supercritical carbon dioxide is the solvent of choice in most solubility experiments. Only a few references were found where the solubility of the nucleobases in supercritical fluids was studied. For example uracil was found to be soluble in carbon dioxide above 100 bar [10] and a study that measures the partitioning of adenine in a carbon dioxide, water, and ethanol system. [2] Zhang et al. [127] reported the mass spectrometric detection of guanine using carbon dioxide as solvent. In the case of nucleobases, preliminary experiments showed that as a pure solvent is was inefficient in dissolving all of the nucleobases at pressures less than 100 bar. Even with the help of a cosolvent, it was not able to dissolve the nucleobases.

Ethylene was selected as a solvent because of being able to exhibit $\pi - \pi$ interaction and it has a relatively low critical point i.e. $p_c = 50.6$ bar and $T_c = 9.35$ °C. Pyrimidine and its derivatives are known to be soluble in supercritical ethylene. [81,124] This was a positive point because of the fact that cytosine, uracil and thymine are derivatives of pyrimidine.

## 4.2. Selection of Cosolvent

Addition of cosolvents to a supercritical fluids can enhance the solubility of a solute manifold, even up to several hundred percent. [34] Ethanol was selected on the basis of the fact that it contains a hydrocarbon part, which is compatible with ethylene, and a polar part, which is compatible with the nucleobases. The polar *-OH* group also participates in hydrogen bonding with the nucleobases [110] which further enhances the solubility. The factors discussed above make ethanol an excellent candidate as a cosolvent.

## 4.3. Purines

The purines studied in this work are guanine and adenine. The solubility order of the purines is discussed in terms of different physical properties and interactions.

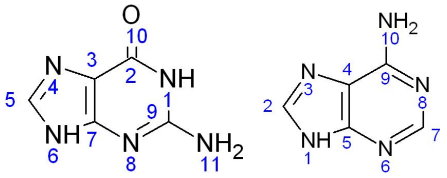

(a) Guanine (b) Adenine

Figure 4.1.: Molecular structure of the purines.

| Purine | Formula | Molecular Weight (amu) | Melting Point (°C) | Dipole Moment (Debye) |
|---|---|---|---|---|
| Adenine | $C_4H_4N_2O_2$ | 135 | 360-365 | 2.66 |
| Guanine | $C_4H_5N_3O$ | 151 | 360-365[a] | 6.88 |

---

[a] Decomposes.

Table 4.1.: Different properties of the two purines investigated in this work

### 4.3.1. Guanine

Guanine was dissolved in supercritical ethylene with ethanol as cosolvent and transferred into the gas phase using molecular beam expansion of the solution.

Figure 4.2 shows the mass spectrum obtained on expansion of the solution in the gas phase. It shows the molecular peak of guanine (mass = 151 amu). The peak maxima is slightly shifted below 151 amu. This is due to slight difference in the mass calibration of the QMS. The fragment masses of guanine were also measured and the molecular peak was found to be of the highest intensity.

By changing the pressure, a pressure dependent plot for the ratio of the molecule to ethylene in the beam was obtained and is shown in Figure 4.3.

### 4.3.2. Adenine

Displayed in Figure 4.4 is the mass spectrum obtained after molecular beam expansion from the solution of adenine in the supercritical fluid. Along with the adenine molecular ion peak (135 amu) peaks are also observed at 133, 136 and 137 amu.

These peaks are accounted for in the calculation as explained in Section A.2. The pressure dependence of the amount of adenine present in the beam is plotted in Figure 4.5.

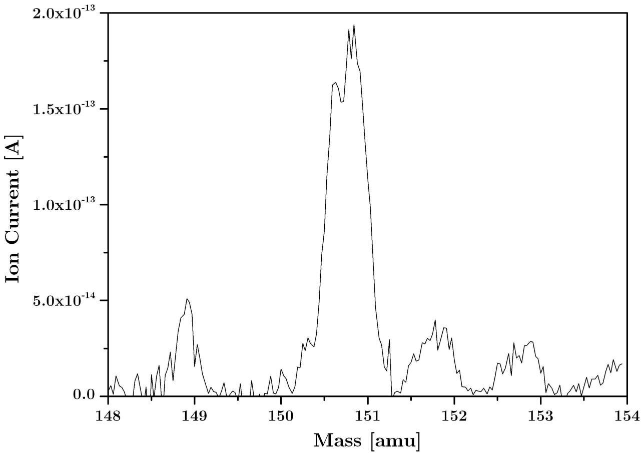

Figure 4.2.: A single scan from the mass spectrum of guanine recorded while pulsing at 0.5 Hz a solution of guanine in ethylene and ethanol (3%) at $p$ = 78.7 to 81.8 bar and $T$ = 40 °C.

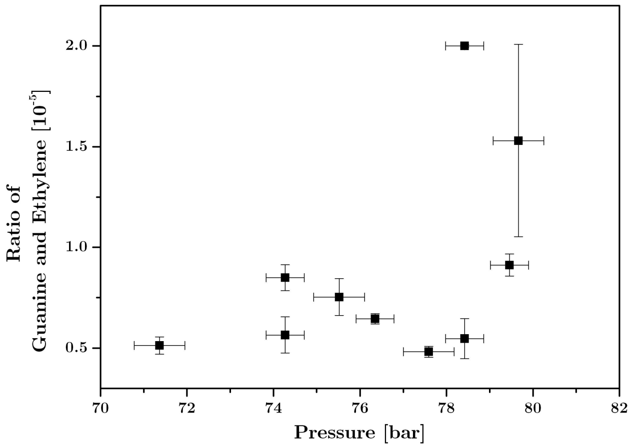

Figure 4.3.: The ratio of guanine with ethylene in the beam is plotted as a function of pressure. For explanation regarding the calculation of the ratio, see Section A.1.

### 4.3.3. Solubility of Purines

Shown in Figures 4.3 and 4.5 are plots for the pressure dependence of the ratio of the nucleobase present in the beam. Taking into consideration different detection and ionization probabilities of the molecules involved, this ratio can directly be compared

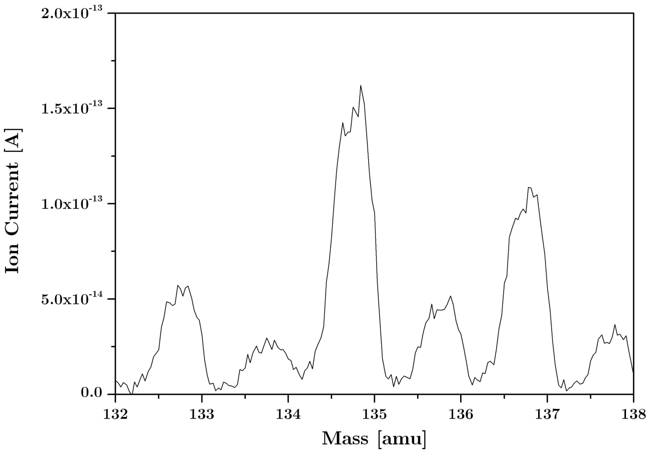

Figure 4.4.: A single scan from the mass spectrum of adenine recorded while pulsing at 0.5 Hz a solution of adenine in ethylene and ethanol (3%) at $p$ = 74.6 to 77.7 bar and $T$=40 °C.

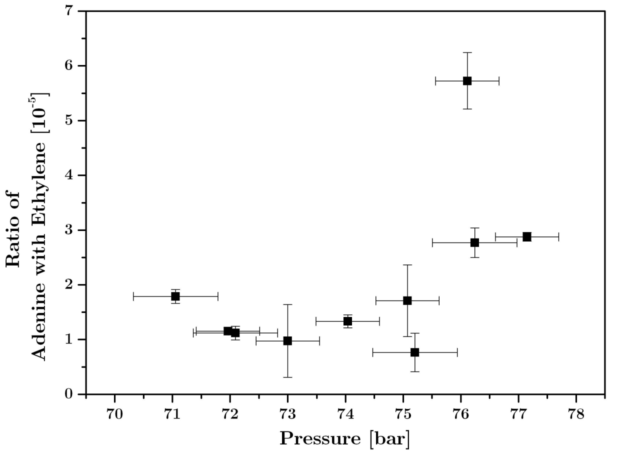

Figure 4.5.: The ratio of adenine with ethylene in the beam is plotted as a function of pressure. For explanation regarding the calculation of the ratio, see Section A.2.

to the solubility of the solute in the supercritical solvent as observed previously for caffeine.[14]

Structure of the solute is very important while considering solubility in a supercritical solvent.[39,59] The molecular structure of both the molecules is shown in Figure 4.1. It is evident from the comparison of the structures that the difference between guanine and adenine is that guanine has an extra oxygen atom attached to the purine ring. This can cause steric hindrance for the $\pi - \pi$ interaction between the unsaturated solvent (ethylene) and the unsaturated purine ring. This is one of the reasons behind the lower solubility of guanine as compared to adenine.

The major interaction that occurs between the solute and the cosolvent is hydrogen bonding. The carbonyl group present on guanine is capable of participating in the conjugation of the purine ring, thus reducing it's basicity. This in turn reduces the strength of the hydrogen bond. This not being present in adenine can lead to the conclusion that adenine would form stronger and thus more stable hydrogen bonds with the cosolvent. On the other hand, presence of a carbonyl group provides guanine with another hydrogen bonding site, thus increasing the overall probability of interacting with the cosolvent.

It is evident from the above discussion that it is not straightforward to explain the solubility order of the purines based on individual parameters. The order in the solubility between the purines is rather determined through a combination of the parameters discussed above.

## 4.4. Pyrimidines

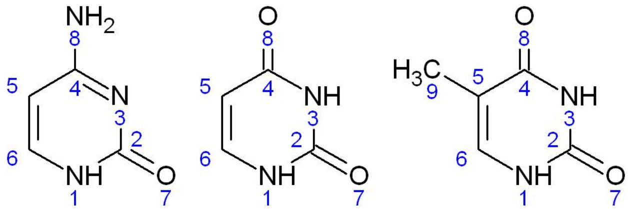

(a) Cytosine (b) Uracil (c) Thymine

Figure 4.6.: Molecular structure of the pyrimidines.

| Pyrimidine | Formula | Molecular Weight (amu) | Melting Point (°C) | Dipole Moment (Debye) |
|---|---|---|---|---|
| Uracil | $C_4H_4N_2O_2$ | 112 | 335 | 5.01 |
| Cytosine | $C_4H_5N_3O$ | 111 | 320-325[a] | 5.99 |
| Thymine | $C_5H_6N_2O_2$ | 126 | 316-317 | 4.50 |

---

[a] Decomposes.

Table 4.2.: Different properties of the three pyrimidines investigated in this work.

Uracil, cytosine and thymine are the pyrimidines that were investigated in this work. The molecule pyrimidine itself is known to be soluble in supercritical ethylene over a wide range of pressure and temperature.[124]

### 4.4.1. Uracil

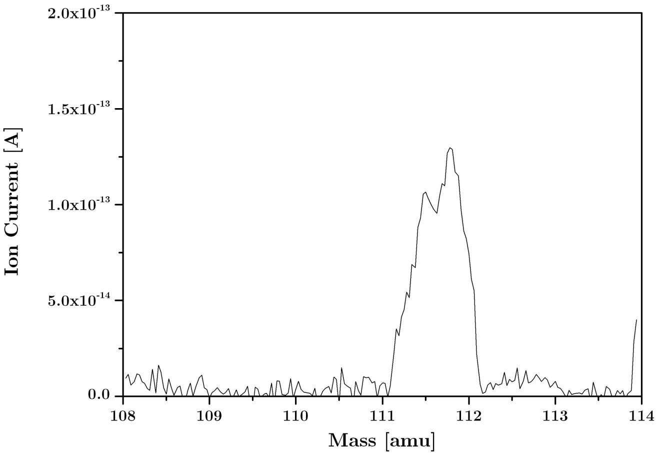

Figure 4.7.: A single scan from the mass spectrum of uracil recorded while pulsing at 0.5 Hz a solution of uracil in ethylene and ethanol (3%) at $p$=72.5 to 75.6 bar and $T$=40 °C.

In this experiment uracil was dissolved in a mixture of supercritical ethylene and ethanol. Pulsed molecular beam of the solution was formed and was detected using the quadrupole mass spectrometer.

Shown in Figure 4.7 is a part of the mass spectrum of uracil detected from the molecular beam expansion of a solution in ethylene and ethanol. It shows a peak which has a maximum at a value slightly less than 112 amu.

Similar scans were performed at different pressures to obtain a pressure dependence of the peak ratio and the pressure dependence of the ratio is shown in Figure 4.8.

### 4.4.2. Cytosine

Cytosine was also dissolved in a mixture of supercritical ethylene and ethanol. It was transferred into vacuum by forming molecular beam of the solution and detected in the gas phase by the QMS. Figure 4.9 shows the major molecular peak of cytosine. Measuring at different pressures depicts a pressure dependence of the ratio of cytosine and is shown in Figure 4.10. Apart from the main molecular peak of cytosine, other peaks present at 109, 110, 112 and 113 are also detected. They originate from the background and are accounted for during the calculations as described in Section A.2.

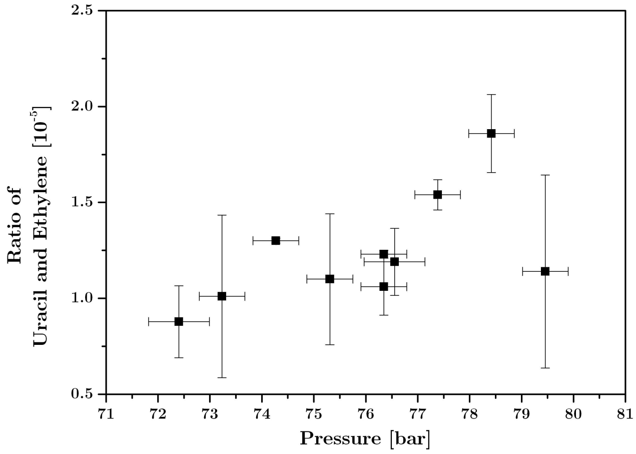

Figure 4.8.: The ratio of uracil with ethylene in the beam is plotted as a function of pressure. For explanation regarding the calculation of the ratio, see Section A.1.

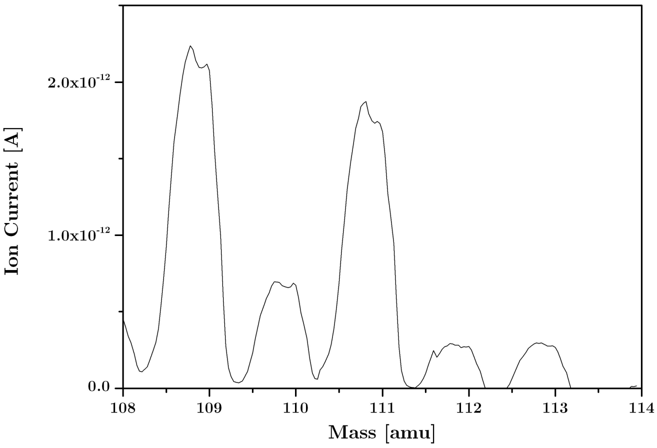

Figure 4.9.: A single scan from the mass spectrum of cytosine recorded while pulsing at 0.5 Hz a solution of cytosine in ethylene and ethanol (3%) at $p$=77.7 to 80.8 bar and $T$=40 °C.

### 4.4.3. Thymine

Thymine is the nucleobase which is exclusive to DNA. In RNA, the nucleobase uracil is present instead of thymine. Thymine is also known as 5-methyluracil, as is apparent from the name. It can be synthesized by methylation of uracil at the 5th carbon atom.

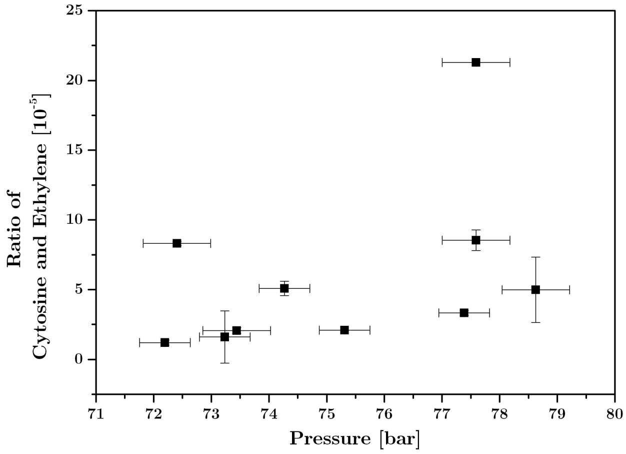

Figure 4.10.: The ratio of cytosine with ethylene in the beam is plotted as a function of pressure. For explanation regarding the calculation of the ratio, see Section A.2.

Despite measuring over a wide range of pressure and temperature similar to the ones for the previous nucleobases, thymine signal was not detected in the gas phase. Thus it is concluded that the solubility of thymine is extremely low in the supercritical solution used in this experiment.

### 4.4.4. Solubility of Pyrimidines

Figures 4.8 and 4.10 show the pressure dependence of the ratio of cytosine and uracil in the beam at a constant temperature. These values have a direct relationship to the solubility in the supercritical solution as exhibited in the case of caffeine previously.[14] Thus it is possible to obtain an ordering of the solubility with cytosine being most soluble and thymine being the least soluble pyrimidine. Given below is a discussion on this order and different factors that could play a role.

An important factor while discussing solubility of organic molecules in supercritical fluids is the molecular structure. The basic skeleton molecule (pyrimidine) is soluble in pure supercritical ethylene,[124] so the discussion regarding the structure will be related to the effect of the side groups on the solubility. Given in Figure 4.6 are the molecular structures of the pyrimidines studied in this work. Examining the structures, different changes regarding the side-groups can be observed. Uracil and thymine contain two oxygen side-groups whereas cytosine has only a single oxygen substituted on the ring as a side group. The pyrimidine nucleobases have the ability to form keto enol tautomers, thus converting the carbonyl group to a hydroxyl group. It has been reported in literature that on the addition of an hydroxyl group to the pyrimidine ring, it's solubility in ethylene drops by almost 2-3 orders of magnitude.[81,124] So the decrease in solubility can be attributed by an presence of an extra oxygen molecule on uracil as compared to cytosine. Furthermore, addition of methyl group also blocks the $\pi - \pi$ interaction through steric hindrance[96] of unsaturated solvent with the unsaturated pyrimidine ring. Studies involving supercritical ethylene also show that addition of a sidegroup on a heterocyclic aromatic ring also decreases the solubility significantly.[80] This can explain the lower solubility of thymine with respect to uracil.

In terms of dipole moments, it is seen that the solubility increases as the dipole moment increases as well. As the solvent (ethylene) itself is non-polar, the effect can be attributed due to the addition of ethanol. Thus the cosolvent effect (increase in solubility due to presence of cosolvent) is higher for a molecule with higher dipole moment.

All of the pyrimidines are able to form hydrogen bonds. Hydrogen bonding also plays a role in the solvation of pyrimidines in the supercritical fluid as we use ethanol as cosolvent. The structures of the pyrimidines show that uracil and thymine have similar side groups, except the presence of a methyl group in thymine which does not participate in hydrogen bonding. Therefore, the effect of hydrogen bonding will be similar for thymine and uracil. On comparison with cytosine, it can be seen that cytosine has an amine group instead of a carbonyl group. The carbonyl groups in cytosine and uracil participate in the ring conjugation, thus reducing the basicity to a greater extent then that done in the case of cytosine, and will lead to a hydrogen bond weaker than that formed by the amine group.

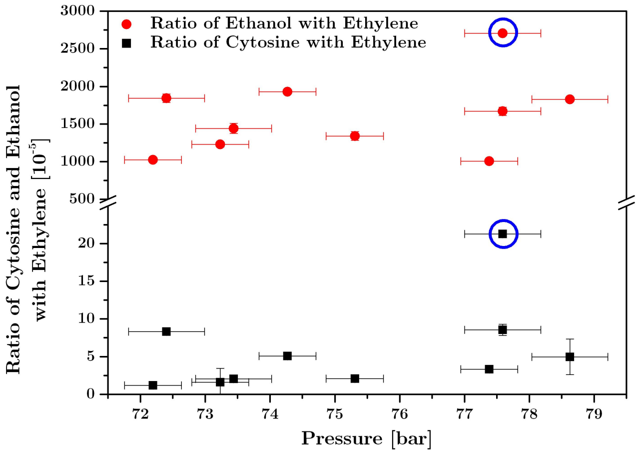

Figure 4.11.: Comparison of ratio of cytosine with ratio of ethanol present in the beam. The circled data points correspond to the same measurement. For explanation regarding the calculation of the ratio, see Section A.2.

Figure 4.11 shows the comparison of cytosine in the beam with ethanol. The point lying at 77.6 bar for cytosine can be explained on the basis of the differences in the ethanol concentration. The ethanol value at that pressure is higher than average, and is the cause for the high cytosine value at that particular pressure.

## 4.5. Conclusions

The preferential local density enhancement of a cosolvent around a solute is one of the most important phenomenon to be considered while discussing the solubility of a solute in a supercritical fluid.[57,58,118,126] In the case of nucleobases in supercritical ethylene with ethanol as cosolvent, it is evident that the so called 'cosolvent effect' is mainly due to the interactions between the nucleobases and ethanol. The cosolvent effect is defined as the increase in solubility of a solute by addition of a cosolvent to a supercritical fluid. The importance of the cosolvent effect is further supported by the fact that the nucleobases were not found to be soluble in pure supercritical ethylene.

# 5. Surface Deposition of Nucleobases

One of the most practical usage of supercritical fluids is the production of nanoparticles, which can be used in the cosmetics as well as the drug industry. Soda lime silicate (SLS) slides were used as substrates for depositing the nucleobases. Atomic force microscopy (AFM) was employed to image the morphology of the thin particulate films produced using the RESS process. Furthermore, morphology of films of the nucleobases on glass produced by drop casting methanol solutions of the nucleobases were also studied using AFM.

The two methods used for deposition are explained briefly below.

## 5.1. Rapid Expansion of Supercritical Ethylene

Supercritical ethylene with ethanol as cosolvent (1-3 %) was used to dissolve the nucleobases. A SLS glass slide was placed at ∼ 5 cm from the nozzle orifice. For all the RESS deposits discussed below, the pressure and the temperature of the solution was kept between 80-90 bar and at 40 ± 3 °C, respectively. Opening time of the nozzle was kept between 500-1500 $\mu$s and the nozzle pulsing rate was between 1-2 Hz. The nozzle was pulsed until a layer in the form of a circle was visible on the glass slide. The circular shape of the deposits is due to the geometry of the nozzle orifice. The glass slide was removed and then Atomic Force Microscopic images were recorded from different locations on the surface.

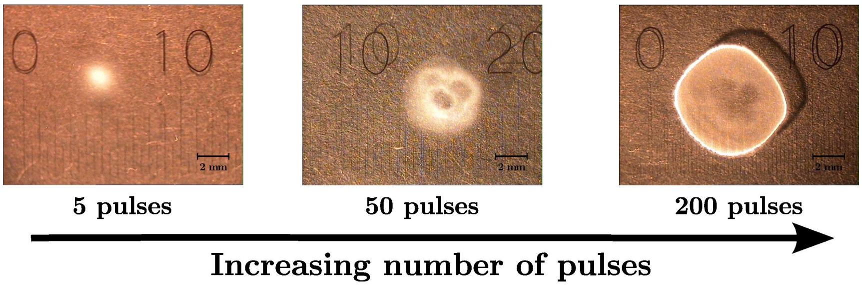

Figure 5.1.: Optical microscopy images of cytosine deposited on a glass slide at atmospheric pressure from a solution of supercritical ethylene and ethanol. The glass slide was placed at ∼ 5 cm from the nozzle opening and the number of pulses were increased to obtain this series of images.

Figure 5.1 depicts the optical microscopic images of cytosine deposited on a glass slide. A cytosine film is visible and the amount of cytosine deposited can easily be controlled by increasing the number of pulses as shown. Figure 5.1 also displays the circular form of the deposits discussed above. In the first image from the left, it is clear that the maximum amount of deposition occurs in the middle of the circle, whereas, in the third image the majority of the deposits seem to shift to the border.

## 5.2. Drop Casting

The drop casting method was employed to deposit the nucleobases on SLS glass slides using methanol as solvent. Solutions of all the nucleobases except guanine with concentration of $10^{-3}$ M were prepared. Guanine could not be used for deposition purposes using this method since it was found to have vanishingly low solubility in methanol. A 1 mL syringe was used to place a few drops ($\sim$ 0.1 mL) of the solution on a SLS glass slide. The SLS glass slide was left in air till the solvent evaporated leaving behind thin multilayers of the solute. The layer of the solute thus produced was imaged using an optical microscope as well as using the AFM.

## 5.3. Atomic Force Microscope

All AFM images were taken using the instrument "Nanosurf Mobile S" (Nanoscience Instruments, Inc.) which is shown in Figure 5.2. To eliminate acoustic noise, the AFM was placed on top of a vibrational isolated board (Halcyonics Inc.).

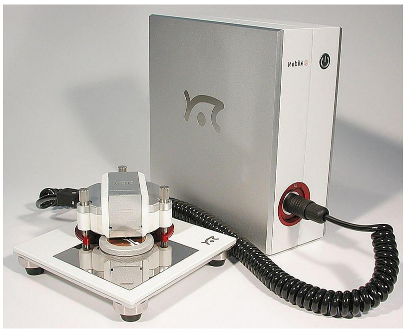

Figure 5.2.: The instrument Nanosurf Mobile S used in this work (Image from Nanoscience Instruments Inc.).

The scan head used had an xyz scan range of 110 x 110 x 22 $\mu$m. The cantilevers used were standard silicon tapping cantilevers (Pointprobe - Silicon SPM Sensors, Nanoworld, Inc.) with a force constant of 48 N/m and a thickness of 7 $\mu$m. The length and width of the cantilevers was 225 $\mu$m and 38 $\mu$m, respectively. The resonance frequency used for the measurement was about 190 kHz. The nominal tip radius of the probe was 10 nm.

The instrument was calibrated using a standard calibration grid with xy and z periodicity of 10 $\mu$m and 110 nm respectively. An image recorded from the calibration grid is shown in Figure 5.3 along with a line scan. The images depicted here were all recorded in tapping mode.

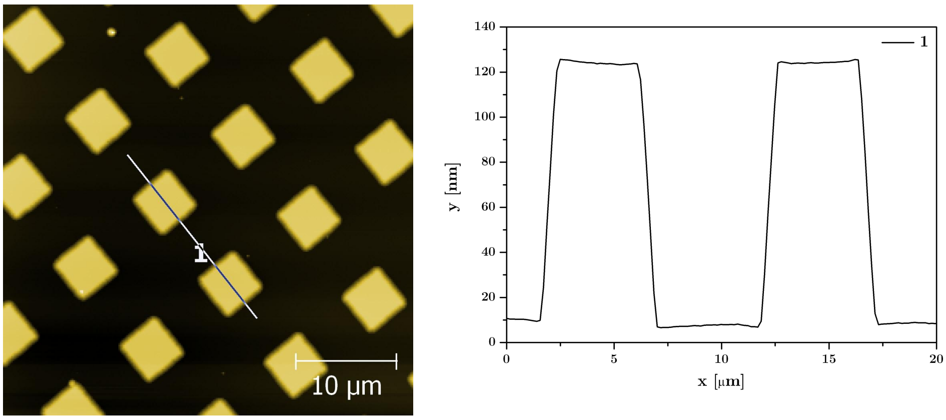

(a)

(b)

Figure 5.3.: Image recorded from the calibration grid depicting the xyz periodicity.

An important parameter that needs to be defined here is the roughness parameter ($R$). It is used to determine the surface uniformity of a film. It is defined as the root mean square of the deviation in *Z(x)* (height of the profile) in a region $r$ and is given by the formula:

$$R_{rms} = \sqrt{\frac{1}{r}\int_0^r \left|Z^2(x))\right| dx} \tag{5.1}$$

This parameter will be used in this work to determine and compare the surface roughness of different thin films.

## 5.4. Nucleobases on Surfaces

Taking into account the huge interest present in studying these molecules on surfaces, there is not much work available in literature addressing the morphology of thin films of nucleobases. Despite of there being significant amount of work available on imaging these molecules at the molecular level on surfaces, research relevant to imaging the structure of multilayers of nucleobases is rare. It has recently been reported[46] that inter and intra molecular structure of thin films of DNA bases cannot be directly correlated to that present in the gas phase or solutions, thus motivating more research relevant in this field.

### 5.4.1. Cytosine

Figure 5.4 depicts in an AFM image of cytosine together with a line scan. An aspect of the image worth noting is that cytosine forms rod like structures of different dimensions

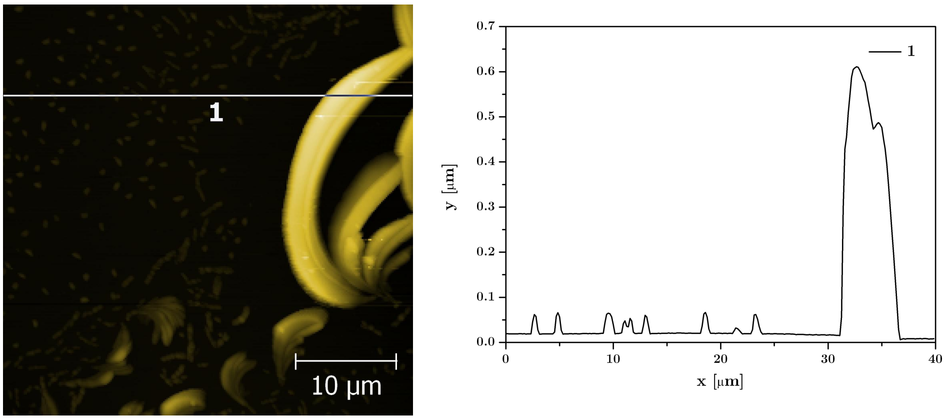

(a) (b)

Figure 5.4.: Atomic force microscopy image of cytosine deposited using the drop casting method on a glass slide (a) and the corresponding line scan (b).

ranging from 1-10 $\mu$m size.

Sarantopoulou et al[103] reported the formation of ultra thin films of cytosine by drop casting and then etching with a 157 nm laser. They reported a surface roughness of 10 nm of cytosine films which was improved further by laser illumination. Reported below are AFM images of cytosine using the two methods described above.

Another remarkable feature that can be observed is that the area immediately around the fingers of the large particle is void of smaller particles. This is also evident in Figure 5.5b where the area between the fingers does not contain any smaller particle. It can be concluded from these observations that upon nucleation, if the concentration is large enough, the particles prefer to aggregate to form the large finger like structure rather than smaller particles. Figure 5.5a displays another area where a collection of similar structures is present. It is worth noting here that there are many empty areas present in between the structures. This can also be explained similarly as for the previous image. It should be remarked here that depending on different conditions, the size and number of these structures varied but the overall morphology of these cytosine particles was found to be similar to the one depicted in these AFM images.

The comparison of the images produced in this work with the images reported by Sarantopoulou et al.[103] is difficult because of different substrates, and also due to the fact that the solvent used in the work by Sarantopoulou et al.[103] is not given. It should also be noted here that these structures seem to be substrate dependent, as deposition on other surfaces (e.g. polycrystalline gold) did not exhibit formation of such structures.

Literature survey reveals that there are no studies reported in literature which pertain to the production of particles or thin films of cytosine using the RESS process. Thin particulate films of cytosine images using AFM are reported here for the first time. RESS process is known to form nano to micro sized particles and also the fact that agglomeration of these particles occur during deposition has been reported.[76,117] Unless mentioned otherwise, images were scanned from the border of the main deposit which

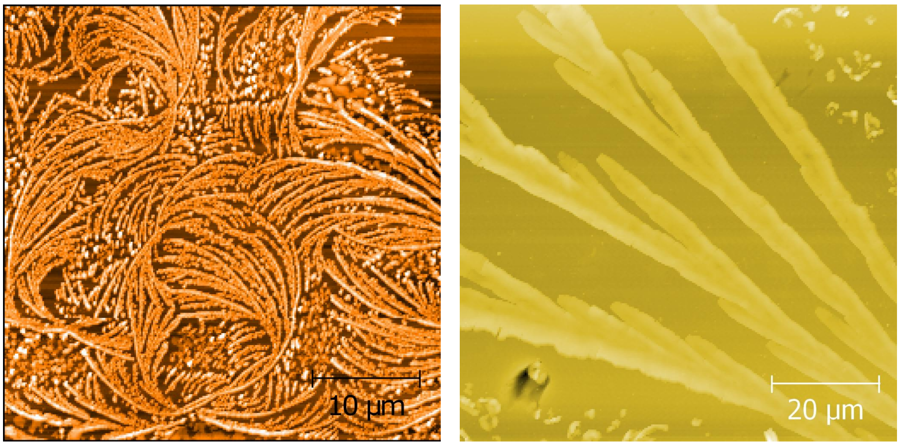

(a) (b)

Figure 5.5.: AFM images acquired from different sections of cytosine deposited on glass. Both (a) and (b) show similar structures with different dimensions

allows imaging of single particle rather than larger agglomerates.

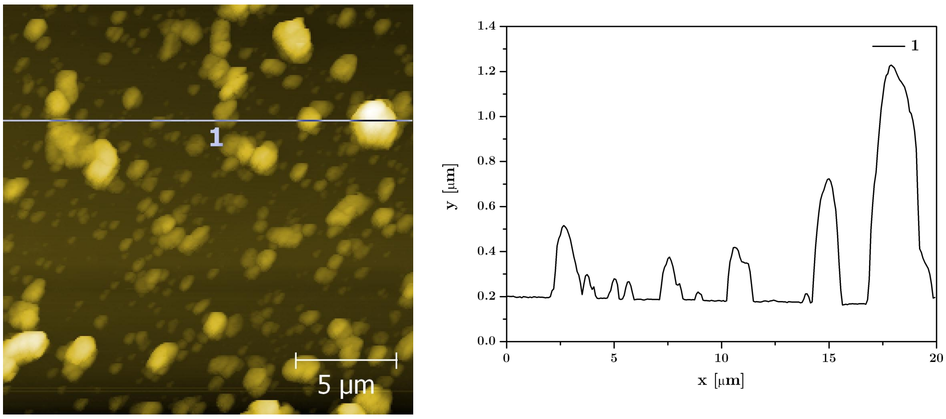

(a) (b)

Figure 5.6.: AFM image of cytosine deposited using RESS on a glass slide (a) and the corresponding line scan (b). Particles are observed with sizes ranging from submicrometer to micrometer region as evident in the line scan.

Figure 5.6 depicts an AFM scan to observe the particle morphology and a line scan to obtain information on the heights of the particles. The image shows particles varying in size from nano to micro meters. A close inspection of the line scan reveals small steps and shoulders in the peaks for the larger particles. This indicates that the larger micro sized particles are agglomerates of much smaller particles. The roughness parameter $\sigma$

was found to be ~ 100 nm. Although this roughness parameter is much larger than the one reported by Sarantopoulou et al.,[103] the advantage of RESS to produce thin particulate films is that no further treatment, such as laser etching or very stringent crystallization conditions are required.

Figure 5.7a shows a three dimensional view of Figure 5.6a. The 3D image shown in Figure 5.7b is recorded from near the middle of the deposit, where the concentration of agglomerates is much higher.

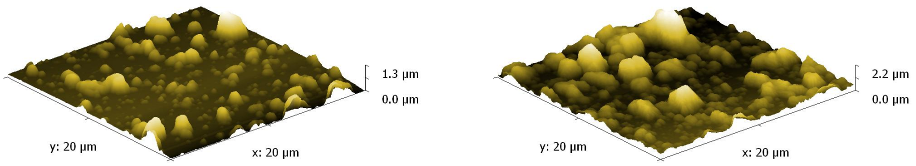

(a) (b)

Figure 5.7.: (a) 3D projection of Figure 5.6a. (b) 3D view of an image recorded near the middle of the main deposits signifying agglomeration.

## 5.4.2. Thymine

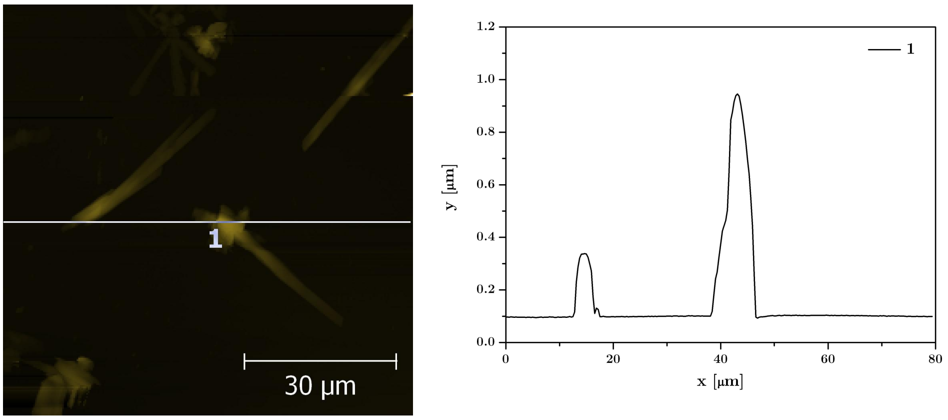

(a) (b)

Figure 5.8.: Atomic force microscopy image of thymine deposited on a SLS glass slide (a) and a line scan (b). Rod like structures with similar dimensions are seen throughout the image.

Most of the research work related to thymine deposition on different substrates is of relevance to a lot of differing fields, ranging from biosensing, to nanotechnological applications. Morphological studies of thymine deposited on surfaces such as HOPG and Au are limited to monolayer depositions and are used to gain knowledge regarding the interaction of the molecule with the substrates.[44]

Figure 5.8a depicts an AFM scan of thymine deposited on SLS glass using methanol as solvent. It shows that thymine forms mainly long rod like particles with a very high aspect ratio of differing lengths and heights. The height of two different particles is shown in the line scan (Figure 5.8b). A shoulder can be observed in the line scan for the larger particle. Close inspection of the data reveals that it is formed by aggregation of smaller particles.

Figure 5.9a displays an AFM scan of a large particle present on the surface. The irregular geometry of the particle and the line scan (Figure 5.9b) suggests that the particle is a collection of smaller particles rather than being a single entity.

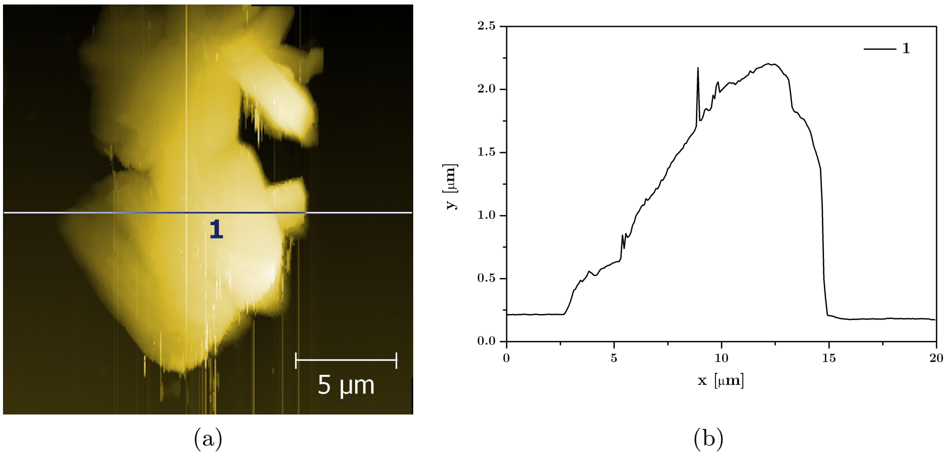

(a) (b)

Figure 5.9.: Atomic force microscopy image of thymine deposited on a glass slide (a) and a line scan (b).

It can be concluded that drop casting of thymine produces mainly larger (5-10 $\mu$m) rod like particles with a surprisingly high aspect ratio.

Thymine was deposited on a SLS glass slide using the RESS process and the images recorded using AFM are shown below. Figure 5.10a depicts an AFM scan of the deposited thymine particles. Interestingly, thymine is seen to form distinct islands upon deposition using the RESS process. It has been observed that these islands are composed of much smaller nano-micro sized particles, which is evident also from the steps seen in the line scan shown in Figure 5.10b. The height of the particles ($<$ 100 nm) can also be evaluated by inspection of the line scan.

The thin particulate films produced were further studied using higher magnifications of one of the island and the AFM images are depicted in Figure 5.11.

A large collection of round nano to microparticles strongly support the fact that

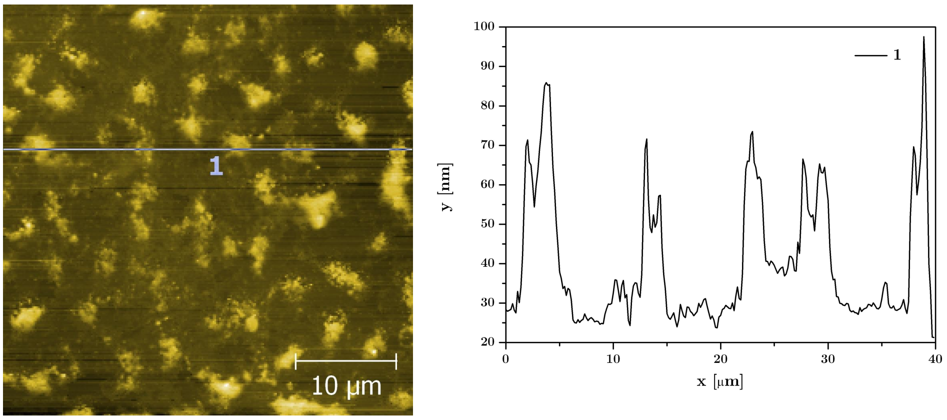

(a)

(b)

Figure 5.10.: Atomic force microscopy image of thymine deposited on a glass slide (a) and a line scan (b). Islands composed of smaller particles are seen in the image.

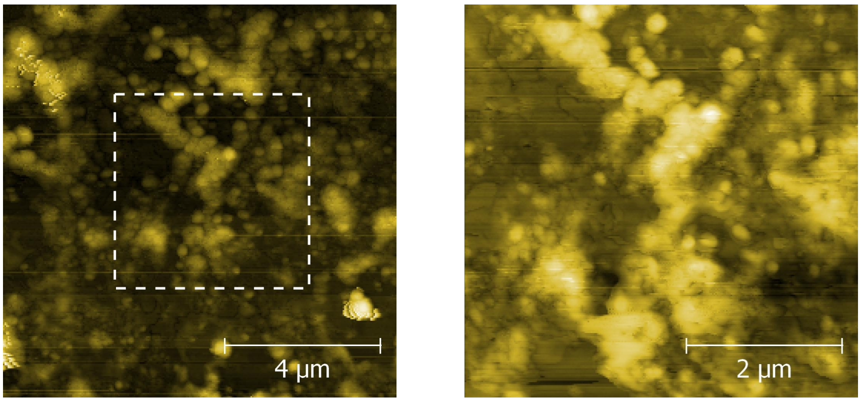

Figure 5.11.: (a) AFM image of the thymine particulate films observed on RESS deposition. (b) Higher magnification from (a) displays spherical particles at the nanometer scale.

the islands seen in Figure 5.10a are a collection of smaller particles. Figure 5.11 also shows further magnification of the image which exhibit spherical particles. As this magnification level is near the resolution limit of the AFM, the image quality is slightly effected.

### 5.4.3. Uracil

Studying the multilayered structure of uracil on surface using AFM has so far not been reported in literature, although work is reported pertaining to the monolayer of uracil on different surfaces such as Au,[30,48] and Si.[38]

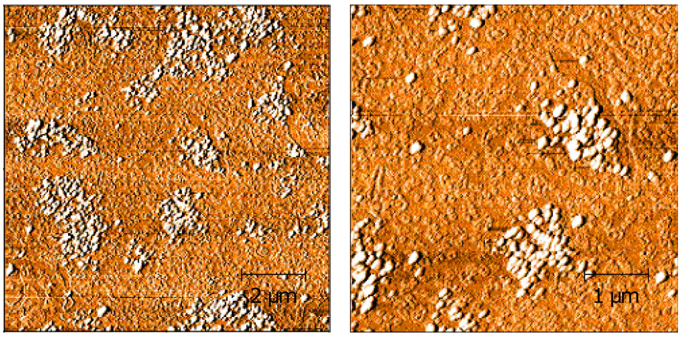

(a) (b)

Figure 5.12.: Atomic force microscopy image of uracil deposited on a SLS glass slide using the drop casting method (a) and a line scan (b). A uniform film together with small particles clustered together are seen in the image.

Uracil formed uniform thin particulate films on the SLS glass surface as apparent from the contrast in the AFM scan in Figure 5.12. Shown in Figure 5.12b is a magnified image of Figure 5.12a.

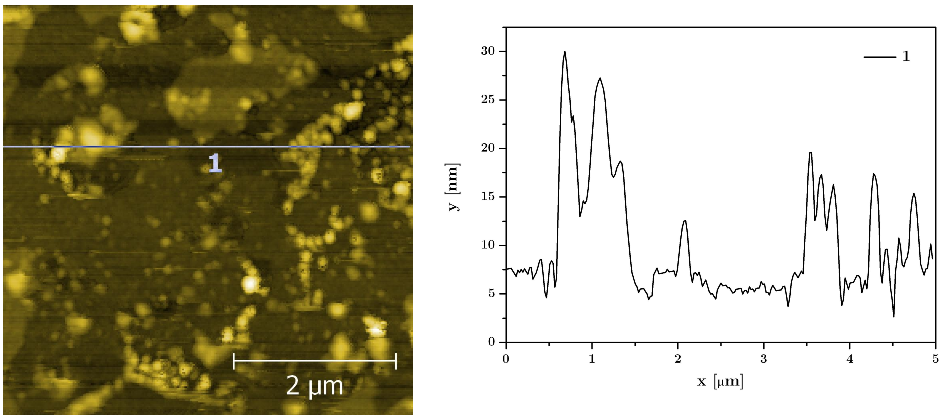

(a) (b)

Figure 5.13.: Atomic force microscopy image of uracil deposited on a SLS glass slide (a) and a line scan (b). Smaller particles aggregate to form larger ones as evident from the line scan.

In case of RESS deposition, the AFM image is shown in Figure 5.13a along with a line scan depicted in Figure 5.13b. Nanoparticles as well as agglomerates to produce microparticles are displayed in the image. The image also exhibits a very low surface roughness, which is $< 10$ nm. The scan size of the image in Figure 5.13a is near the limit of the AFM resolution. For this reason the image quality suffers, but despite of that, the image clearly portrays the ability of RESS process to form uniform particulate films of uracil.

### 5.4.4. Adenine

Results given below compare the morphology of adenine films and particles on a SLS slide, when formed using drop casting and RESS.

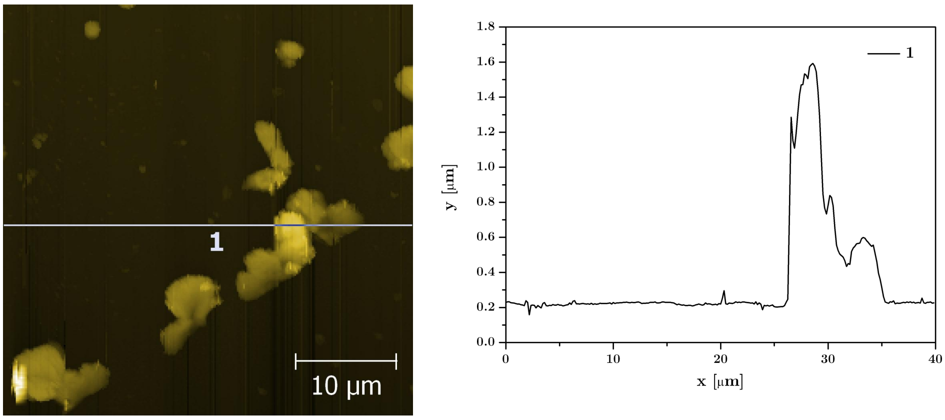

(a) (b)

Figure 5.14.: AFM image of adenine deposited on a glass slide using the drop casting method (a) and a line scan (b).

Previous research work dealing with the structure of adenine on surfaces is in part largely composed of monolayer studies. AFM and SEM images reported by Sarantopoulou et al.[103] long 2-10 $\mu$m size particles before being subjected to 157 nm laser. Shown in Figure 5.14a are adenine particles deposited on a glass slide using methanol as solvent. Figure 5.14b depicts the height of the line scan through the image. As is evident from the image and the line scan, the particles have a dimension of 2-5 $\mu$m.

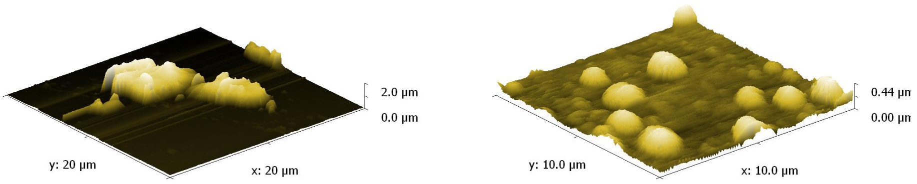

(a) (b)

Figure 5.15.: (a) 3D projection of a single particle exhibiting a relatively flat surface. (b) Image recorded from on top of a large adenine particle.

Furthermore, adenine deposits are depicted in Figure 5.15 using 3D projections of the AFM images. Figure 5.15a shows a large particle which is relatively flat, whereas Figure 5.15b is an image scanned from on top of a large adenine deposit exhibiting a relatively uniform surface.

It can be concluded that drop casting of adenine particles using methanol as solvent produces flat disc like particles varying in size from 5 to 10 $\mu$m.

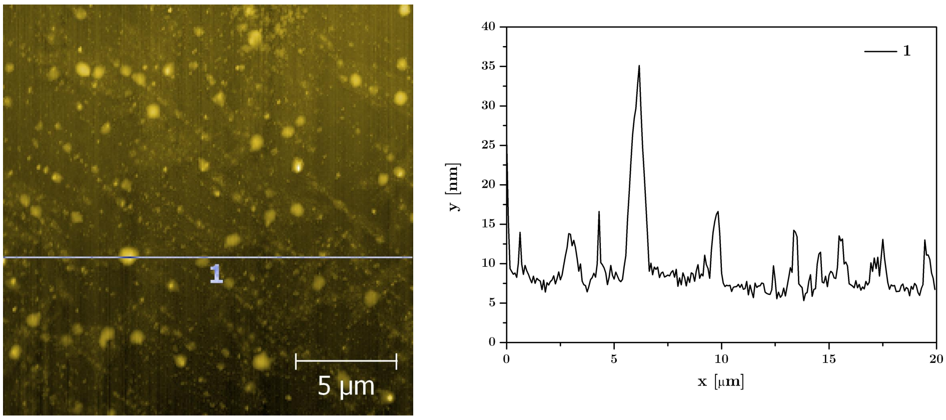

(a)

(b)

Figure 5.16.: AFM image of adenine deposited on a SLS glass slide using RESS (a) and a line scan (b). Particles ranging from submicrometer to nanometer region are observed as is evident from the line scan.

Figure 5.16a depicts an AFM image of RESS deposits of adenine on glass. It is evident from the figure that nano to micro particles of adenine are formed by using the RESS process under these conditions.

The line scan given in Figure 5.16b displays the height of different particles exhibiting a uniform height distribution with a few exceptions. The larger particles are considered to be agglomerates of smaller particles rather than being produced as single entities. The surface uniformity is also confirmed by the value of surface roughness amounts to $< 30$ nm. This surface roughness value is comparable to the ones achieved by Sarantopoulou et al.[103] after subjecting the film to laser at 157 nm.

Like most techniques AFM has it's limitations. One of the most common challenge while employing AFM is to separate 'real' images from tip artifacts. Tip artifacts are features that are produced once the tip is contaminated and/or damaged. To rule out the possibility of tip artifacts plaguing the images, optical microscopic images were taken at high magnification and then compared with AFM images. Shown in Figure 5.17 is such a comparison. The image recorded using the optical microscope has been tilted and digitally resized to match the orientation and size of the AFM image. As is clear from the comparison, the particles produced are of the same geometry and size. No pronounced tip changes were observed by repeatedly measuring the same location. This justified the fact that the AFM image produced in Figure 5.17 is free of tip artifacts and also helped increase confidence in the AFM measurements.

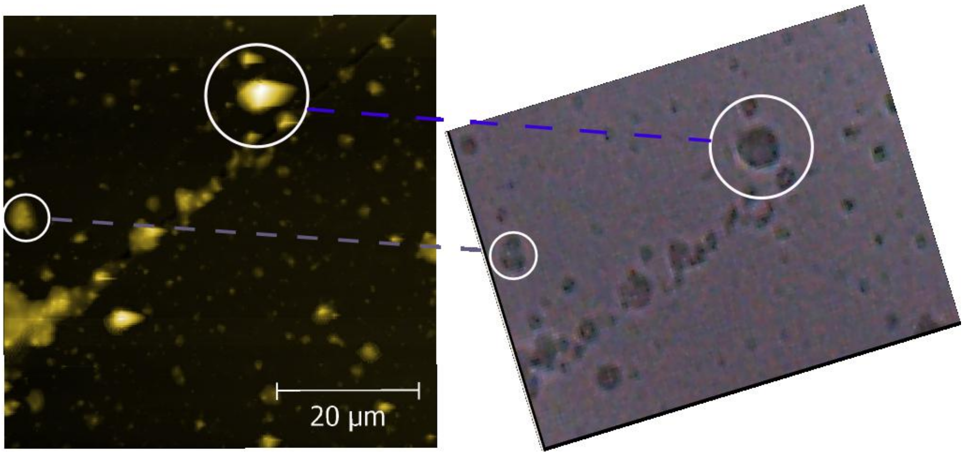

Figure 5.17.: Comparison of AFM and optical microscopy images. Major similarities in both images are circled for clarity.

### 5.4.5. Guanine

Solubility of guanine in many organic solvents is either extremely low or it is insoluble. Usually pH of the solvent needs to be altered to increase the solubility, which in turn can results in different tautomeric forms of the molecules. Furthermore, thermal evaporation of guanine has also been reported to be problematic as guanine has the tendency to dissociate at increased temperatures.[56]

Reported herein, are results from RESS deposits of guanine as well as molecular beam deposition of guanine on glass slides. Molecular beam deposition was carried out at a vacuum of $\sim 10^{-6}$ mbar.

Figure 5.18a depicts an AFM image of RESS deposited guanine on a SLS glass slide. It is evident from the line scan (Figure 5.18b) as well as the image that nanoparticles of guanine are formed with some microsized agglomerates. An interesting feature in the bottom right corner of the AFM image is the presence of a curve. This feature is part of a symmetrical ring which is seen with more detail in the AFM images depicted in Figure 5.19.

The AFM images displayed in Figure 5.19 exhibit the presence of microsized rings along with other particles ranging in the nano to micrometer range. Figure 5.19b displays a scan of one of the many rings observed. These bright circular features are seen to be present in varying dimensions, ranging from 10-30 $\mu$m size. The presence of these features can be explained by the combination of the basics of the RESS method and an effect known as 'Coffee Tabletop' effect.

Similar to the micro particle formation of guanine, it can be safely assumed that microsized particles of ethanol are also formed. Moreover, small droplets of ethylene can also condense and instantly evaporate on the SLS glass slide due to the expansion.

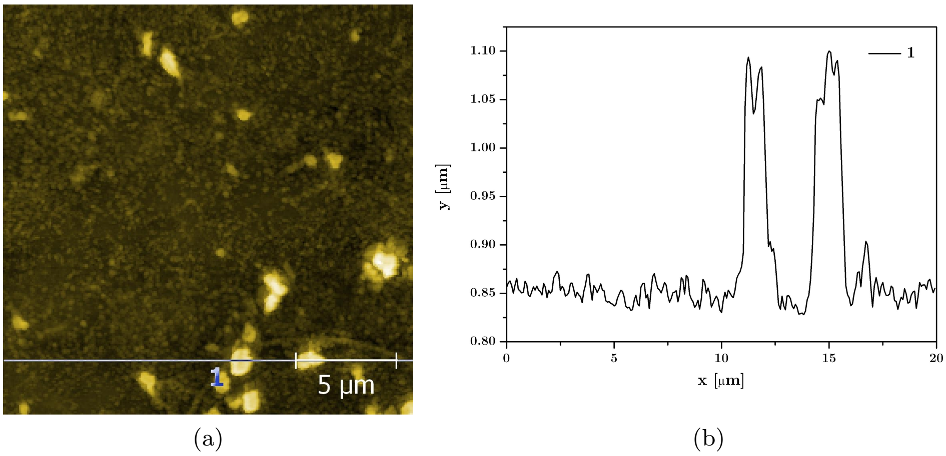

Figure 5.18.: Atomic force microscopy image of guanine deposited using the RESS process on a glass slide (a) and a line scan (b). Nanoparticles can be seen in the image along with a few agglomerates.

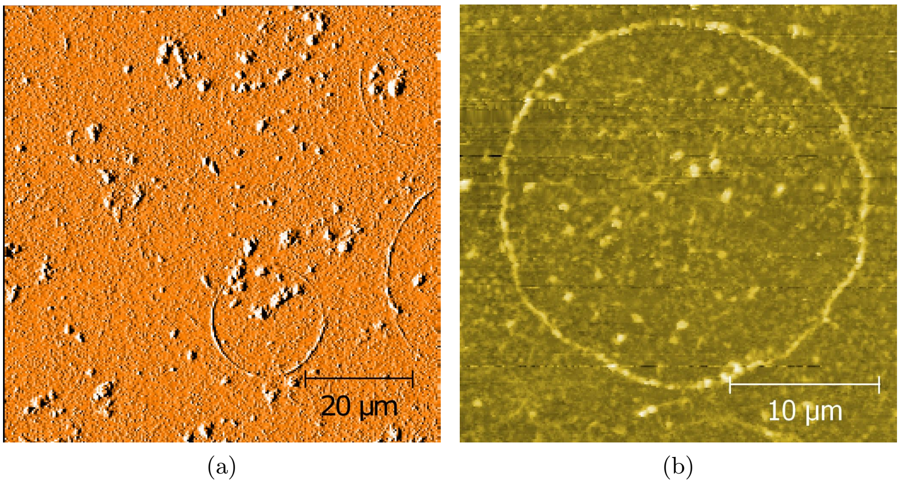

Figure 5.19.: (a) AFM image depicting deposits formed from the RESS of guanine exhibiting ring like structures(b) Magnified view of a ring produced by guanine deposits on a SLS slide.

Since guanine solubility in ethanol is extremely low, so it can be ruled out that ethanol droplets carry the particles onto the surface. Thus, the condensation and evaporation of ethylene droplets which contain guanine can be suspected as the cause of these ring structures being formed on the surface. The ring formation has been commonly observed at a relatively larger scale for drops of coffee drying on a table and has been the center of research quite recently.[26,70] The only difference between the two methods described

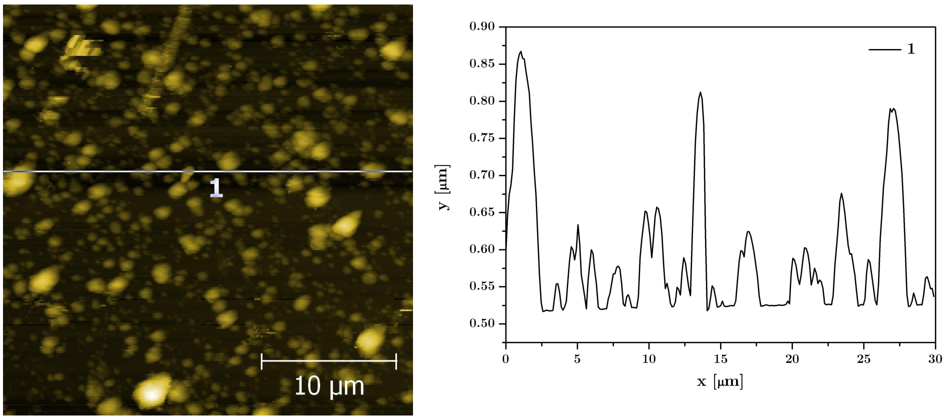

(a) (b)

Figure 5.20.: (a) Atomic force microscopy image of guanine particulate films fabricated using molecular beam deposition on a SLS glass slide. (b) The line scan shows sub-micrometer to nanometer sized particles.

here to deposit guanine is that the post expansion pressure is reduced significantly in the case of molecular beam deposition. This can prove useful for producing clean films of guanine on different substrates. It has been previously suggested that decreasing the post expansion pressure results in a increase in the particle size.[78] AFM scan of molecular beam deposited guanine on a glass substrate is shown in Figure 5.20a. The corresponding line scan is depicted in Figure 5.20b.

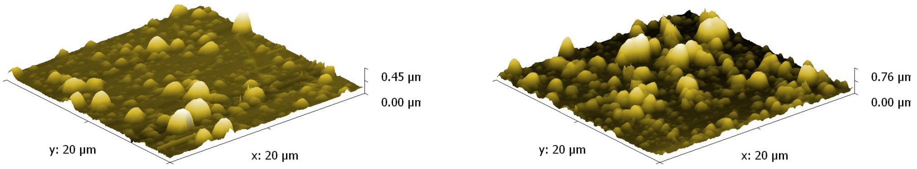

(a) (b)

Figure 5.21.: (a) 3D projection of Figure 5.18a (b) 3D projection of an image recorded from the guanine deposit at a location with much higher density of the deposits.

Figure 5.21 shows two 3D projections of different AFM scans from the molecular beam deposited guanine. The comparison of the AFM images for the molecular beam deposited guanine in Figure 5.20a with Figure 5.18 reveals that in general larger particles are observed when the post expansion pressure is decreased, which is supported by previous experiments.[78]

## 5.5. Thermal Desorption Spectroscopy of Guanine

Using supercritical fluids for deposition of nucleobases on substrates, requires no significant amount of heating (~ 40 °C). Molecular beam expansion from solutions of supercritical fluids produced particles which can be deposited onto substrates placed in the path of the beam. From the five nucleobases discussed here, guanine has been reported to be thermally labile.[11] Although guanine can be evaporated and detected in the gas phase directly, much higher temperatures are required to reach enough flux for deposition using a molecular beam.[55] Using molecular beam expansion of guanine dissolved in supercritical fluid, thin films were deposited on a polycrystalline gold surface.

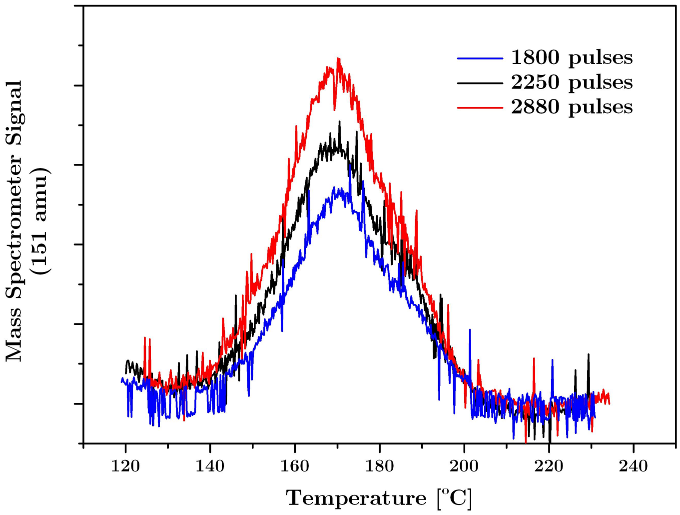

Figure 5.22.: TDS of molecular beam deposited guanine on polycrystalline gold.

Interaction of guanine with gold is of huge interest in development of DNA biosensors. Östblom et al[85] reported the dynamics of the DNA bases adsorbed on gold by using infra-red absorption spectroscopy (IRAS) and thermal desorption spectroscopy (TDS). Reported below are TDS measurements of guanine deposited on gold using molecular beam expansion from supercritical solutions. Number of pulses was varied to give films of different thicknesses. Figure 5.22 depicts three temperature programmed desorption spectra of guanine from polycrystalline gold. All three spectra exhibit a single peak with a shoulder present at higher temperature. The main peak is centered around 170 °C. The fragment masses of guanine were also measured and it was observed that the molecular peak was the most intense peak observed.

## 5.6. Discussion

The desorption spectra of guanine is examined using the line shape analysis. The desorption temperature of the peaks observed for different spectra in Figure 5.22 does not change significantly, thus it is assumed to be a first order desorption. Desorption kinetics is explained using a rate law which leads to an equation known as the Redhead Equation.[99] The rate law for a first order desorption process is given below:

$$-\frac{dN}{dt} = \nu_1 N e^{-\frac{E_d}{RT}} \tag{5.2}$$

where N = coverage (molecules $\mathrm{cm}^{-3}$), $\nu_1$ = first order frequency factor ($\mathrm{s}^{-1}$), and $E_d$ = activation energy (J $\mathrm{mol}^{-1}$) and R = gas constant (J $\mathrm{K}^{-1}$ $\mathrm{mol}^{-1}$). The rate law has been converted to a fitting function by Yates et al.[51] for the desorption peaks and is used to fit the peaks as shown in Figure 5.23.

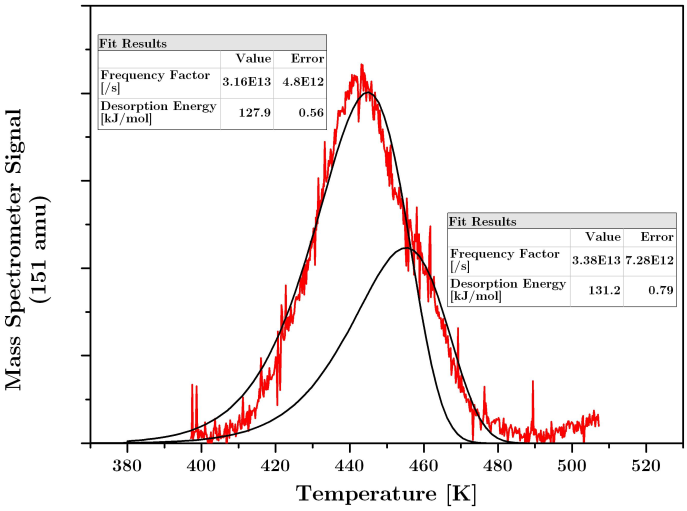

Figure 5.23.: Desorption peak of guanine from polycrystalline gold, along with two fits with values for the frequency factor and desorption energy.

The equation used as a fitting function is given below.

$$P(T) = \exp\left(-\frac{T}{\beta}\right)\frac{\nu_1}{\beta}\left[\int_0^T \exp\left[\frac{T}{\beta\tau} - \frac{E_d}{RT} - \frac{\nu_1 R}{\beta E_d}T^2 \exp\left(-\frac{E_d}{RT}\right)\right]dT\right] \tag{5.3}$$

where *P(T)* = normalized profile of the desorption spectrum with $\beta$ = heating rate (0.5 K/s) and $\tau$ = characteristic pumping speed (1.9 s). The value of $\tau$ is determined from the fitting of this equation to the experimental result.

Two peaks are used to fit the spectrum because of the large improvement in the error observed by using two peaks instead of a single peak to fit the data. The two peaks correspond to two different binding geometries of the guanine molecule on the gold surface as reported by Östblom et al.[85] The same parameters provided satisfactory fits for the other spectra with lower coverages. This leads once again to the conclusion that the desorption process is of first order. Moreover, the ratio between area under the curve for the fits remained constant with increasing coverage as seen in Table 5.1. This leads to the conclusion that the population of molecules present in both peaks increases with the same amount on increasing the coverage.

| **Number of pulses** | **Ratio between the fitted peaks** |
|---|---|
| 2880 | 1.80 |
| 2250 | 1.77 |
| 1880 | 1.82 |

Table 5.1.: Ratio between the peaks fitted to the desorption curve with different coverages.

The desorption energy for the major peak has a value of 127.9±0.56 kJ/mol which coincides with the value reported by Östblom et al.[85] The desorption spectra of guanine on gold is strongly dependent on the incubation time. In the spectra reported by Östblom et al.,[85] three different thermal desorption spectra are reported with increasing incubation time. They assigned the main peak to be originating from mono to submonolayer coverage of guanine molecule. They also observed a shoulder similar to the one observed here but could not evaluate its origin because of the inability of IRAS to resolve it.

In the case of molecular beam expansion of guanine using supercritical fluids for deposition purposes, there is theoretically no incubation time and the molecule is deposited as nano to micro particles directly on to the surface. This can also be seen in the fact that no new peaks appear on increasing the number of pulses, rather both the major peak and the shoulder increase with the same ratio. Thus it is concluded that it is similar to the spectrum observed by Östblom et al.[85] where the incubation time was minimum, as theoretically our incubation time is zero.

The RESS process has been used to form thin particulate films of the nucleobases and the deposits were studied using AFM. Interestingly, the nucleobases exhibited morphologically similar particles on using RESS for the fabrication of the particulate films. The main reason behind the uniformity of the particles obtained using the RESS process is the rapid pressure decrease leading to very a high supersaturation ratio.[25] Also, in the case of guanine some interesting rings were observed(See Figure 5.19). An effort has been made to explain the formation of these rings on the basis of formation of ethylene droplets, although it remains unclear if such phenomenon is also observed for the other nucleobases.

In the case of drop casting, the nucleobases exhibited different morphology depending on the molecule. Generally the observed particles were much larger than the one observed in RESS. This can be explained on the basis of the fact that during evaporation of the solvent, the supersaturation ratio increases up to the point of nucleation. These small nuclei undergo an extended crystal growth process. Interestingly, cytosine was seen to form self assembled structures on the soda lime silicate glasses. The case of using a volatile solvent to form crystals is much more complicated and needs to be investigated further for a better understanding.

# 6. Summary and Outlook

This work has successfully exhibited the applications of supercritical fluids in the analytical field through molecular beam detection and deposition of non-volatile molecules, namely DNA/RNA bases. The results obtained show promise regarding the use of supercritical fluids as a carrier gas for molecular beam expansion.

A new bracketing method using the phenomenon of increased scattering at the gas-liquid phase boundary has been developed for the determination of the critical coordinates of supercritical fluids. The increased scattering is due to condensation of small liquid droplets on the measurement window, which lead to scattering of light once the system is present at the phase boundary. In the liquid phase the system does not exhibit any scattering because, then these droplets coalesce to form a transparent film, whereas in the gas phase no scattering is observed because of the absence of these droplets.

The study of the shift in critical point of a supercritical fluid with a cosolvent showed an increase in the critical temperature of only 5.5 °C. The theoretical methods used in this work have not been able to determine the critical temperature accurately. This signifies the importance of the experimental determination of the critical coordinates. Furthermore, it motivates work to study the interaction between the solvent and cosolvent through spectroscopic measurements.

The molecular beam detection of the nucleobases provides valuable information regarding the solubility of the solutes in the supercritical fluid. The solubility order (cytosine $>$ uracil $\sim$ adenine $>$ guanine $>$ thymine) is explained on the basis of chemical interactions occurring between the solvent/cosolvent molecules and the solute. Moreover, it inspires study of other relevant molecules for a better understanding of solvation.

The RESS study exhibits the application of supercritical fluids for the purpose of forming uniform thin particulate layers of the nucleobases. Furthermore, some unexpected morphologies were observed, such as in the case of RESS of guanine and drop casting of cytosine, which warrants further investigations. Reported here, for the first time, is the molecular beam deposition of guanine on gold using a supercritical fluid at near ambient temperature. Pulsed molecular beam deposition of guanine on polycrystalline gold was used to control the amount deposited and determine the binding energy of guanine on gold (127.9 kJ/mol) which matched the one reported in literature.[85]

The relatively high binary interaction parameter reported in this work is an indication of significant interactions between ethylene and ethanol. Although adding a cosolvent to a supercritical fluid is common practice, there is a limited amount of data available on the exact nature of the interactions between the solvent and cosolvent. UV-Vis spectroscopy can be used to investigate the behavior of a cosolvent dissolved in a supercritical fluid. For example, by observing the n-$\pi^*$ shift of benzophenone, Knutson et al.[60] investigated the behavior of many cosolvents when dissolved in supercritical ethane.

Similar measurements can be performed on the ethylene-ethanol system for a better understanding of the interactions taking place between them. Furthermore, such measurements on a range of cosolvents can also lead to results that helps in the selection of a cosolvent better suited for a particular solute.

All the nucleobases contain a basic pyrimidine ring and are capable of forming tautomers. This has recently been a major field of research because of the biological importance of these molecules. Gas phase studies (for instance laser spectroscopy) of these molecules have been used to identify different tautomers and the research has been reviewed recently.[23] Transfer of these molecules in these experiments are generally carried out by thermal evaporation. In the case of guanine, it is difficult to assign the rotational spectrum because of it's thermal instability.[11] The molecular beam expansion of guanine using supercritical fluids can be used to transfer the molecule into the gas phase without any thermal deterioration. This method can be a viable alternative to thermal evaporation for non-volatile molecules.

The uniformity and the morphology of the nucleobases obtained using RESS can be controlled to a greater extent by changing the expansion conditions, which can lead to applications of these films in bio-organic field effect transistors[74] and molecular nanowires.[95]

# A. Appendix A

Two different methods were used for calculating the ratio of the solute present in the beam. The first method (Direct Ratio Method) was used when a peak of the solute was observed without any significant amount of background peaks and the second method (Reference Peak Method) was used when the unwanted peaks were of the same order as the main peak.

## A.1. Direct Ratio Method

The direct ratio method was used to calculate the ratio of the solute in the beam for the measurements involving guanine and uracil. Due to presence of some background peaks in guanine, the Reference Peak Method was also applied to the data. This did not lead to the any significant change in the results as when the Direct Ratio Method was used thus justifying the usage of this method. The details of the method are described below for the calculations involving uracil. Mass spectra were recorded in the range of interest for the molecules with the pulsed molecular beam on and once with the pulsed molecular beam off. The spectra recorded when the molecular beam was not operating was considered as background and subtracted from the spectra obtained when the molecular beam was on. Figure A.1 depicts the mass spectra in the range of interest for uracil, ethylene and ethanol after background subtraction. Ethanol undergoes dissociation upon electron

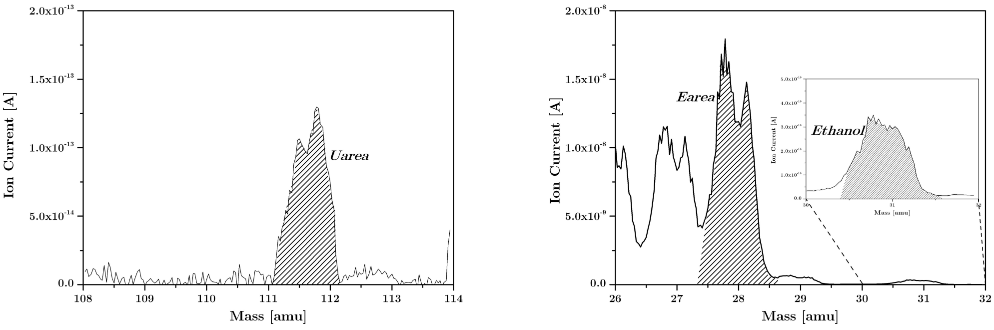

(a) (b)

Figure A.1.: Range of interest for the mass spectra of (a) uracil and (b) ethylene and ethanol. See text for details regarding treatment of data.

ionization and the major peak is present at 31 amu rather than 46 amu which is the molecular mass of ethanol.

The area under the peaks was evaluated using the script given below (Section A.1.1) and are shaded as seen in Figure A.1. The area under the peak for uracil (*Uarea*), ethylene (*Earea*), and ethanol (*Ethanol*) correspond to the terminology used in the script given below. The ratio is simply calculated by the ratio *Uarea/Earea*. Depending on the number of scans used for evaluation a standard deviation was obtained. This 'Ratio of Guanine/Uracil with Ethylene' and the corresponding standard deviation has been plotted against pressure in Figures 4.3 and 4.8 for guanine and uracil, respectively.

### A.1.1. Uracil Script

```
// This script is for evaluating the ratio of solute
// and ethylene from a number of analog scans for uracil
// Written for Microcal Origin Ver 8 with LabTalk
// Book1 and onwards must be the scans recorded using
// the QMS after background subtraction
// Masses Uracil: 111.31 to 112.31, Ethylene: 27.41 to 28.41,
// Ethanol: 30.41 to 31.41.
// Book1 to Book5 = 5 Scans

// creating worksheet to collect results
create Calcs -w 5 EArea GArea Ratio EthanolRatio;

// loop to go through each scan separating ethylene
// and solute peaks and evaluating ratios
for (ii=1; ii<=5; ii++){
create Solute$(ii) -w 200 Mass Intensity;
create Ethylene$(ii) -w 200 Mass Intensity;
copy -b 22 Book$(ii)_A Solute$(ii)_MASS -b 1 -e 191;

// plotting graphs for solute and solvent
win -t plot line SoluteScan$(ii);
layer -i Solute$(ii)_intensity;
win -t plot line EthyleneScan$(ii);
layer -i Ethylene$(ii)_intensity;

// separating solute and solvent from main scan
copy -b 22 Book$(ii)_B Solute$(ii)_INTENSITY -b 1 -e 191;
copy -b 215 Book$(ii)_A Ethylene$(ii)_Mass -b 1 -e 191;
copy -b 215 Book$(ii)_B Ethylene$(ii)_INTENSITY -b 1 -e 191;

//obtaining area under the peak for uracil (112 amu),
// ethylene (28 amu) and ethanol (31 amu)
```

```
integ solute$(ii)_intensity -b 107 -e 139; // Uracil
Uarea$(ii)=integ.area;
integ ethylene$(ii)_intensity -b 46 -e 78; // Ethylene
Earea$(ii)=integ.area;
integ ethylene$(ii)_intensity -b 142 -e 174; // Ethanol
Ethanol$(ii)=integ.area;

//ratio of uracil and ethylene
Ratio$(ii) = UArea$(ii)/EArea$(ii);

//ratio of ethanol and ethylene
Eratio$(ii) = Ethanol$(ii)/EArea$(ii);

//placing calculated values in worksheet
window -a Calcs;
Col(1)[$(ii)] = EArea$(ii);
Col(2)[$(ii)] = UArea$(ii);
Col(3)[$(ii)] = Ratio$(ii);
Col(4)[$(ii)] = Eratio$(ii);
};
```

## A.2. Reference Peak Method

This method for calculating ratio of the nucleobases in the beam was used for the measurements involving adenine and cytosine. Given below is an explanation of the method using the a single example for cytosine.

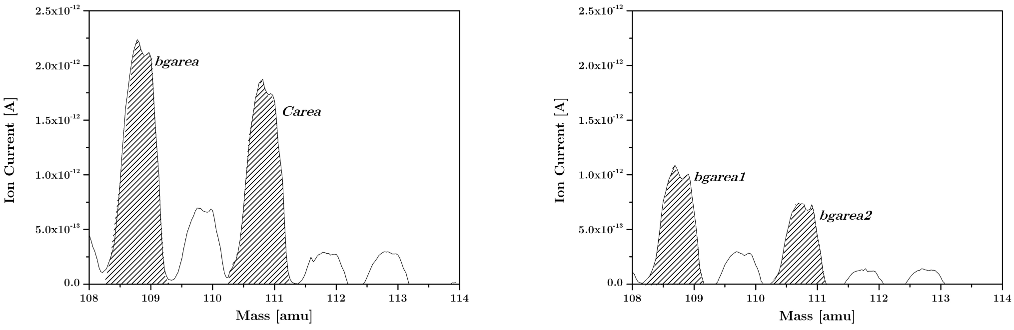

(a) (b)

Figure A.2.: Range of interest for the mass spectra of cytosine (a) with pulsing and (b) without pulsing. See text regarding evaluation of data.

In this case, no background subtraction was done for the mass spectra, but rather the original data was used for evaluation. The reason will become clear with the explanation given below. Seen in Figure A.2 are two mass spectra in which (a) was recorded with the molecular beam on and (b) was recorded without pulsing the molecular beam. It was observed that simple subtraction still showed a peak at 109 amu, which is absent in the mass spectrum of cytosine (from NIST). Whereas, the mass 111 is also observed in the background scan. To eliminate the increase in the peak at 109 amu caused due to background, the following procedure was adopted.

The terminology used in the graphs for the peak areas are the ones also used in the script given below (Section A.2.1. The ratio (*ratiobg*) between the area under the peaks observed in the background scan (*bgarea1* and *bgarea2*) was evaluated. Similarly the ratio (*Ratio*) between the area under the reference peaks (*bgarea*) and apparent cytosine peak (*Carea*) was also evaluated. *Carea* is composed of the actual cytosine contribution (*Cactual*) plus the background contribution (*Ref*). As the ratio between the background peaks at 111 and 109, is equal to the ratio of the background contribution (*Ref*) with background peak (*bgarea*), the following method was adopted to remove the background contribution from the peak at 111 amu.

$$\begin{aligned} ratiobg &= \frac{bgarea2}{bgarea1} \\ Ratio &= \frac{Carea}{bgarea} = \frac{Creal + Ref}{bgarea} \\ \frac{bgarea2}{bgarea1} &= \frac{Ref}{bgarea} \end{aligned}$$

Thus the background contribution (*Ref*) to the cytosine peak can be calculated to be:

$$Ref = \frac{bgarea2}{bgarea1} \cdot bgarea$$

and the contribution of cytosine (*Carearea*) is then given as:

$$Careareal = Carea - \frac{bgarea2}{bgarea1} \cdot bgarea$$

Rewriting in terms of ratios:

$$
\begin{aligned}
Careareal &= (\frac{Carea}{bgarea} - \frac{bgarea2}{bgarea1}) \cdot bgarea \\
Careareal &= (Ratio - ratiobg) \cdot bgarea
\end{aligned}
$$

The area thus calculated is then used to calculate the ratio of cytosine with ethylene (*Careareal/Earea*). Depending on the number of scans used for evaluation a standard deviation was obtained. This 'Ratio of Adenine/Uracil with Ethylene' and the corresponding standard deviation has been plotted against pressure in Figures 4.5 and 4.10 for adenine and cytosine, respectively.

The value for the 'Ratio of Ethanol' was simply calculated by taking the ratio of the area under the peaks shown in Figure A.1b, i.e. *Ethanol/Earea.* This value is plotted in Figure 4.11 against pressure for the 'Ratio of Ethanol with Ethylene'.

### A.2.1. Cytosine Script

```
// This script is for evaluating the ratio of solute and
// ethylene from a number of analog scans for cytosine
// Written for Microcal Origin Ver 8 with LabTalk
// Reference mass subtraction using a reference peak at
// 109 amu is performed
// Book1 must be the background scan and Book2 onwards
// must be the measured cycles with pulses
// Masses Cytosine: 110.31 to 111.31, Ethylene: 27.41 to 28.41,
// Ethanol: 30.41 to 31.41. Bg: 108.31 to 109.31
// Book 1 = Background, Book2 to Book6 = 5 Scans

// separating ethylene and solute peaks from the
// main file of the background scan
Create Solbg -w 200 Mass Intensity;
copy -b 22 Book1_A Solbg_MASS -b 1 -e 191;
copy -b 22 Book1_B Solbg_Intensity -b 1 -e 191;

//obtaining area under the peak at mass 109 and 111 amu
// and their ratio
integ solbg_intensity -b 11 -e 43; // mass 109
bgarea1=integ.area;
integ solbg_intensity -b 75 -e 107; // mass 111
bgarea2=integ.area;
ratiobg=bgarea2/bgarea1;

// creating worksheet to collect results
```

```
create Calcs -w 5 EArea CArea Ratio Bgsubratio Ethanol Bgratio;

// loop to go through each scan separating ethylene and
// solute peaks and evaluating ratios
for (ii=2; ii<=6; ii++){
Create Solute$(ii) -w 200 Mass Intensity;
Create Ethylene$(ii) -w 200 Mass Intensity;
copy -b 22 Book$(ii)_A Solute$(ii)_MASS -b 1 -e 191;

// plotting graphs for solute and solvent
win -t plot line SoluteScan$(ii);
layer -i Solute$(ii)_intensity;
win -t plot line EthyleneScan$(ii);
layer -i Ethylene$(ii)_intensity;

// separating solute and solvent from main scan
copy -b 22 Book$(ii)_B Solute$(ii)_INTENSITY -b 1 -e 191;
copy -b 215 Book$(ii)_A Ethylene$(ii)_Mass -b 1 -e 191;
copy -b 215 Book$(ii)_B Ethylene$(ii)_INTENSITY -b 1 -e 191;

// obtaining area under the peak for cytosine (111 amu),
// reference (109 amu), ethylene (28 amu) and ethanol (31 amu)
integ solute$(ii)_intensity -b 75 -e 107; // cytosine
Carea$(ii)   = integ.area;
integ solute$(ii)_intensity -b 11 -e 43; // reference
bgarea$(ii)   = integ.area;
integ ethylene$(ii)_intensity -b 46 -e 78; // ethylene
Earea$(ii)    = integ.area;
integ ethylene$(ii)_intensity -b 142 -e 174; // ethanol
Ethanol$(ii)  = integ.area;

// ratio of ethanol and ethylene
Eratio$(ii)=Ethanol$(ii)/Earea$(ii);

// ratio of cytosine and ethylene before subtraction
// using the reference mass
Ratio$(ii)    = CArea$(ii)/EArea$(ii);

/ /ratio between the apparent cytosine peak with the reference mass
Ratiocyt$(ii)   = Carea$(ii)/bgarea$(ii);

// calculating contribution from cytosine in the peak
Careareal$(ii) = (ratiocyt$(ii)-ratiobg)*bgarea$(ii);
Ratioc$(ii) = Careareal$(ii)/Earea$(ii);
```

```
// placing results in worksheet
window -a Calcs;
Col(1)[$(ii)] = EArea$(ii);
Col(2)[$(ii)] = CArea$(ii);
Col(3)[$(ii)] = Ratio$(ii);
col(4)[$(ii)] = Ratioc$(ii);
Col(5)[$(ii)] = Eratio$(ii);
Col(6)[$(ii)] = Ratiocyt$(ii);
};
```

# Bibliography

[1] Andrew P. Abbott, Christopher A. Eardley, and James E. Scheirer. $CO_2$/HFC 134a mixtures: alternatives for supercritical fluid extraction. *Green Chemistry*, 2 (2):63–66, 2000.

[2] Till Adrian, Jeorg Freitag, and Gerd Maurer. Partitioning of some biomolecules at high pressures to aqueous/organic liquid-liquid phases of the carbon dioxide+water+1-propanol system. *The Journal of Supercritical Fluids*, 17(3): 197–213, 2000.

[3] Thomas Andrews. The bakerian lecture: On the continuity of the gaseous and liquid states of matter. *Philosophical Transactions of the Royal Society of London (1776-1886)*, 159:575–590, 1869.

[4] M. J. Anselme and A. S. Teja. Critical properties of dilute multicomponent mixtures. *AIChE Journal*, 36(6):897–906, 1990.

[5] Yasuhiko Arai, Takeshi Sako, and Yoshihiro Takebayashi. *Supercritical Fluids*. Springer, 2002.

[6] Mehdi Ashraf-Khorassani, Larry T. Taylor, Kenneth C. Waterman, Padma Narayan, Daniel R. Brannegan, and George L. Reid. Purification of pharmaceutical excipients with supercritical fluid extraction. *Pharmaceutical Development and Technology*, 10(4):507–516, 2005.

[7] Keith D. Bartle, Anthony A. Clifford, and Gavin F. Shilstone. Estimation of solubilities in supercritical carbon dioxide: A correlation for the peng-robinson interaction parameters. *The Journal of Supercritical Fluids*, 5(3):220–225, 1992.

[8] Bertrand Berche, Malte Henkel, and Ralph Kenna. Critical phenomena: 150 years since Cagniard de la Tour. *Revista Brasileira de Ensino de Fisica*, 31(2):2602, 2009.

[9] André Brack. *The molecular origins of life*. Cambridge University Press, 1998.

[10] Gabriela I. Burgos-Solórzano, Joan F. Brennecke, and Mark A. Stadtherr. Solubility measurements and modeling of molecules of biological and pharmaceutical interest with supercritical $CO_2$. *Fluid Phase Equilibria*, 220(1):55–67, 2004.

[11] Walther Caminati. Nucleic acid bases in the gas phase. *Angewandte Chemie International Edition*, 48(48):9030–9033, 2009.

[12] Wolfgang Christen and Klaus Rademann. Cooling and slowing in high-pressure jet expansions. *Physical Review A (Atomic, Molecular, and Optical Physics)*, 77 (1):012702–5, 2008.

[13] Wolfgang Christen and Klaus Rademann. Probing free jet expansions of supercritical fluids. *Physica Scripta*, 80(4):048127, 2009.

[14] Wolfgang Christen, Stephanie Geggier, Svitlana Grigorenko, and Klaus Rademann. Pulsed supersonic expansion of nonvolatile solids. *Review of Scientific Instruments*, 75(11):5048–5049, 2004.

[15] Wolfgang Christen, Klaus Rademann, and Uzi Even. Efficient cooling in supersonic jet expansions of supercritical fluids: CO and $CO_2$. *The Journal of Chemical Physics*, 125(17):174307–5, 2006.

[16] Wolfgang Christen, Tim Krause, and Klaus Rademann. Precise thermodynamic control of high pressure jet expansions. *Review of Scientific Instruments*, 78(7): 073106–3, 2007.

[17] Wolfgang Christen, Tim Krause, and Klaus Rademann. Transferring pharmaceuticals into the gas phase. *International Journal of Mass Spectrometry*, 277(1-3): 305–308, 2008.

[18] Leigh B. Clark, Gary G. Peschel, and Ignacio Tinoco. Vapor spectra and heats of vaporization of some purine and pyrimidine bases. *The Journal of Physical Chemistry*, 69(10):3615–3618, 1965.

[19] Tony Clifford. *Fundamentals of supercritical fluids*. Oxford University Press, 1999.

[20] Carlos E. Crespo-Hernández, Boiko Cohen, Patrick M. Hare, and Bern Kohler. Ultrafast Excited-State dynamics in nucleic acids. *Chemical Reviews*, 104(4):1977–2020, 2004.

[21] R. Czermiński, B. Lesyng, and A. Pohorille. Tautomerism of pyrimidine bases - uracil, cytosine, isocytosine: Theoretical study with complete optimization of geometry. *International Journal of Quantum Chemistry*, 16(3):605–613, 1979.

[22] C. Cagniard de la Tour. Exposé de quelques résultats obtenu par l'action combinée de la chaleur et de la compression sur certains liquides, tels que l'eau, l'alcool, l'éther sulfurique et l'essence de pétrole rectifiée. *Annales de Chimie et de Physique*, 21:127–132, 1822.

[23] Mattanjah S. de Vries and Pavel Hobza. Gas-phase spectroscopy of biomolecular building blocks. *Annual Review of Physical Chemistry*, 58:585–612, 2007.

[24] Silvia De Dea, David R. Miller, and Robert E. Continetti. Cluster and solute velocity distributions in Free-Jet expansions of supercritical $CO_2$. *The Journal of Physical Chemistry A*, 113(2):388–398, 2009.

[25] Pablo G. Debenedetti. Homogeneous nucleation in supercritical fluids. *AIChE Journal*, 36(9):1289–1298, 1990.

[26] Robert D. Deegan, Olgica Bakajin, Todd F. Dupont, Greb Huber, Sidney R. Nagel, and Thomas A. Witten. Capillary flow as the cause of ring stains from dried liquid drops. *Nature*, 389(6653):827–829, 1997.

[27] Maria del Mar Caja Lopez, Gracia P. Blanch, and Marta Herraiz. Derivatization of chiral amino acids in supercritical carbon dioxide. *Analytical Chemistry*, 76(3): 736–741, 2004.

[28] M. Dey, F. Moritz, J. Grotemeyer, and E. W. Schlag. Base pair formation of free nucleobases and mononucleosides in the gas phase. *Journal of the American Chemical Society*, 116(20):9211–9215, 1994.

[29] Joseph M. Dobbs and Keith P. Johnston. Selectivities in pure and mixed supercritical fluid solvents. *Industrial & Engineering Chemistry Research*, 26(7):1476–1482, 1987.

[30] Th. Dretschkow, A. S. Dakkouri, and Th. Wandlowski. In-Situ scanning tunneling microscopy study of uracil on Au(111) and Au(100). *Langmuir*, 13(10):2843–2856, 1997.

[31] T Gregory Drummond, Michael G Hill, and Jacqueline K Barton. Electrochemical DNA sensors. *Nature Biotechnology*, 21(10):1192–1199, 2003.

[32] Charles A. Eckert, David H. Ziger, Keith P. Johnston, and Timothy K. Ellison. The use of partial molal volume data to evaluate equations of state for supercritical fluid mixtures. *Fluid Phase Equilibria*, 14:167–175, 1983.

[33] Charles A. Eckert, David H. Ziger, Keith P. Johnston, and Sunwook Kim. Solute partial molal volumes in supercritical fluids. *The Journal of Physical Chemistry*, 90(12):2738–2746, 1986.

[34] Charles A. Eckert, Barbara L. Knutson, and Pablo G. Debenedetti. Supercritical fluids as solvents for chemical and materials processing. *Nature*, 383(6598):313–318, 1996.

[35] Albert Einstein. Theorie der Opaleszenz von homogenen Flüssigkeiten und Flüssigkeitsgemischen in der Nähe des kritischen Zustandes. *Annalen der Physik*, 338 (16):1275–1298, 1910.

[36] S. R. M. Ellis, R. L. Valteris, and G. J. Harris. High-Pressure equilibrium still for vapor phase extraction studies. *Chemical Engineering Progress Symposium Series*, 64(1968):16–21, 1968.

[37] Neil R. Foster, Harcharan Singh, S. L. Jimmy Yun, David L. Tomasko, and Stuart J. Macnaughton. Polar and nonpolar cosolvent effects on the solubility of

cholesterol in supercritical fluids. *Industrial & Engineering Chemistry Research*, 32(11):2849–2853, 1993.

[38] K. Fujii, K. Akamatsu, and A. Yokoya. Near-Edge x-ray absorption fine structure of DNA nucleobases thin film in the nitrogen and oxygen k-edge region. *The Journal of Physical Chemistry B*, 108(23):8031–8035, 2004.

[39] S. Garnier, E. Neau, P. Alessi, A. Cortesi, and I. Kikic. Modelling solubility of solids in supercritical fluids using fusion properties. *Fluid Phase Equilibria*, 158-160:491–500, 1999.

[40] Daniel P. Glavin, Michael Schubert, and Jeffrey L. Bada. Direct isolation of purines and pyrimidines from nucleic acids using sublimation. *Analytical Chemistry*, 74 (24):6408–6412, 2002.

[41] S. R. Goates, A. J. Barker, H. S. Zakharia, B. Khoobehi, and C. W. Sheen. Direct supersonic expansions of supercritical fluids for analysis of polycyclic aromatic hydrocarbons. *Appl. Spectrosc.*, 41(8):1392–1397, 1987.

[42] J. A. Gualtieri, J. M. Kincaid, and G. Morrison. Phase equilibria in polydisperse fluids. *The Journal of Chemical Physics*, 77(1):521–536, 1982.

[43] S. K. Gupta, R. D. Lesslie, and A. D. King. Solubility of alcohols in compressed gases. comparison of vapor-phase interactions of alcohols and homomorphic compounds with various gases. i. ethanol in compressed helium, hydrogen, argon, methane, ethylene, ethane, carbon dioxide, and nitrous oxide. *The Journal of Physical Chemistry*, 77(16):2011–2015, 1973.

[44] Wolfgang Haiss, Bernd Roelfs, Simon N. Port, Elke Bunge, Helmut Baumgärtel, and Richard J. Nichols. In-situ infrared spectroscopic studies of thymine adsorption on a Au(111) electrode. *Journal of Electroanalytical Chemistry*, 454(1-2):107 – 113, 1998.

[45] A. Haneda, T. Seki, D. Kodama, and M. Kato. High-Pressure phase equilibrium for ethylene + methanol at 278.15 K and 283.65 K. *Journal of Chemical & Engineering Data*, 51(1):268–271, 2006.

[46] Andrea Haug, Sabine Schweizer, Florian Latteyer, Maria Benedetta Casu, Heiko Peisert, Christian Ochsenfeld, and Thomas Chassé. Thin-Film properties of DNA and RNA bases: A combined experimental and theoretical study. *ChemPhysChem*, 9(5):740–747, 2008.

[47] John M. Hayes. Analytical spectroscopy in supersonic expansions. *Chemical Reviews*, 87(4):745–760, 1987.

[48] M.H. Hölzle, Th. Wandlowski, and D.M. Kolb. Structural transitions in uracil adlayers on gold single crystal electrodes. *Surface Science*, 335:281–290, 1995.

[49] Nakcheol Jeong and Sung Hee Hwang. Catalytic intermolecular pauson - khand reactions in supercritical ethylene. *Angewandte Chemie International Edition*, 39 (3):636–638, 2000.

[50] Hans-Werner Jochims, Martin Schwell, Helmut Baumgärtel, and Sydney Leach. Photoion mass spectrometry of adenine, thymine and uracil in the 6-22 eV photon energy range. *Chemical Physics*, 314(1-3):263–282, 2005.

[51] John T. Yates Jr. and Theodore E. Madey. The adsorption of methane by tungsten (100). *Surface Science*, 28(2):437–459, 1971.

[52] Okitsugu Kajimoto. Solvation in supercritical fluids: Its effects on energy transfer and chemical reactions. *Chemical Reviews*, 99(2):355–390, 1999.

[53] Arthur Kantrowitz and Jerry Grey. A high intensity source for the molecular beam. part I. theoretical. *Review of Scientific Instruments*, 22(5):328–332, 1951.

[54] R. E. A. Kelly and L. N. Kantorovich. Planar nucleic acid base super-structures. *Journal of Materials Chemistry*, 16(20):1894–1905, 2006.

[55] Nam Joon Kim, Yung Sam Kim, Gawoon Jeong, Tae Kyu Ahn, and Seong Keun Kim. Hydration of DNA base cations in the gas phase. *International Journal of Mass Spectrometry*, 219(1):11–21, 2002.

[56] S.K. Kim, W. Lee, and D.R. Herschbach. Cluster beam chemistry: Hydration of nucleic acid bases; ionization potentials of hydrated adenine and thymine. *Journal of Physical Chemistry*, 100(19):7933–7937, 1996.

[57] Sunwook Kim and K. P. Johnston. Clustering in supercritical fluid mixtures. *AIChE Journal*, 33(10):1603–1611, 1987.

[58] Sunwook Kim and Keith P. Johnston. Molecular interactions in dilute supercritical fluid solutions. *Industrial & Engineering Chemistry Research*, 26(6):1206–1213, 1987.

[59] Jerry W. King and John P. Friedrich. Quantitative correlations between solute molecular structure and solubility in supercritical fluids. *Journal of Chromatography A*, 517:449–458, 1990.

[60] Barbara L. Knutson, Steven R. Sherman, Karen L. Bennett, Charles L. Liotta, and Charles A. Eckert. Benzophenone as a probe of local cosolvent effects in supercritical ethane. *Industrial & Engineering Chemistry Research*, 36(3):854–868, 1997.

[61] D. Kodama, R. Sato, A. Haneda, and M. Kato. High-Pressure phase equilibrium for ethylene + ethanol at 283.65 K. *Journal of Chemical & Engineering Data*, 50 (1):122–124, 2005.

[62] Daisuke Kodama, Joji Miyazaki, Masahiro Kato, and Takeshi Sako. High pressure phase equilibrium for ethylene + 1-propanol system at 283.65 K. *Fluid Phase Equilibria*, 219(1):19–23, 2004.

[63] Daisuke Kodama, Takashi Seki, and Masahiro Kato. High-pressure phase equilibrium for ethylene + 1-butanol at 283.65 K and 290.80 K. *Fluid Phase Equilibria*, 261(1-2):99–103, 2007.

[64] Daisuke Kodama, Takuya Yagihashi, Tetsuya Hosoya, and Masahiro Kato. High-Pressure vapor liquid equilibrium for ethylene + 2-Methyl-1-propanol. *Journal of Chemical & Engineering Data*, 54(3):1046–1048, 2009.

[65] Petr Kolář and Kazuo Kojima. Prediction of critical points in multicomponent systems using the PSRK group contribution equation of state. *Fluid Phase Equilibria*, 118(2):175–200, 1996.

[66] Tim Krause. Molecular beam expansion of $C_{60}$ in supercritical fluids. Diplomarbeit, Institut für Chemie der Humboldt-Universität zu Berlin, 2005.

[67] Ronald T. Kurnik, Samuel J. Holla, and Robert C. Reid. Solubility of solids in supercritical carbon dioxide and ethylene. *Journal of Chemical & Engineering Data*, 26(1):47–51, 1981.

[68] Joseph R. Lakowicz. *Principles of Fluorescence Spectroscopy*. Springer, 2nd edition, 1999.

[69] Jae M. Lee, Byung-Chul Lee, and Chan-Hwi Cho. Measurement of bubble point pressures and critical points of carbon dioxide and chlorodifluoromethane mixtures using the variable-volume view cell apparatus. *Korean Journal of Chemical Engineering*, 17(5):510–515, 2000.

[70] Jork Leiterer, Franziska Emmerling, Ulrich Panne, Wolfgang Christen, and Klaus Rademann. Tracing coffee tabletop traces. *Langmuir*, 24(15):7970–7978, 2008.

[71] Zhi-Yong Liu. Prediction of critical pressure of dilute multicomponent mixtures. *AIChE Journal*, 44(7):1709–1712, 1998.

[72] Jie Lu, Buxing Han, and Haike Yan. UV-Vis spectroscopic studies of solute-solvent and solute-cosolvent interactions in supercritical carbon dioxide. *Physical Chemistry Chemical Physics*, 1(14):3269–3276, 1999.

[73] Palenchar Robert M., Erickson Dale D., and Leland Thomas W. Prediction of binary critical loci by cubic equations of state. In *Equations of State*, ACS Symposium Series, pages 132–155. American Chemical Society, 1986.

[74] Giuseppe Maruccio, Paolo Visconti, Valentina Arima, Stefano D'Amico, Adriana Biasco, Eliana D'Amone, Roberto Cingolani, Ross Rinaldi, Stefano Masiero, Tatiana Giorgi, and Giovanni Gottarelli. Field effect transistor based on a modified DNA base. *Nano Letters*, 3(4):479–483, 2003.

[75] Eva Mateo-Martí, Claire-Marie Pradier, and Jose-Angel Martín-Gago. Ultraviolet photostability of adenine on gold and silicon surfaces. *Astrobiology*, 9(6):573–579, 2009.

[76] Dean W. Matson, John L. Fulton, Robert C. Petersen, and Richard D. Smith. Rapid expansion of supercritical fluid solutions: solute formation of powders, thin films, and fibers. *Industrial & Engineering Chemistry Research*, 26(11):2298–2306, 1987.

[77] Dmitri I. Mendeleev. Ueber die ausdehnung der flüssigkeiten beim erwärmen über ihren siedepunkt. *Annalen der Chemie und Pharmacie*, 119(1):1–11, 1861.

[78] Rahoma S. Mohamed, Pablo G. Debenedetti, and Robert K. Prud'homme. Effects of process conditions on crystals obtained from supercritical mixtures. *AIChE Journal*, 35(2):325–328, 1989.

[79] Kunio Nagahama. VLE measurements at elevated pressures for process development. *Fluid Phase Equilibria*, 116(1-2):361–372, 1996.

[80] Tadashi Nakatani, Kazunari Ohgaki, and Takashi Katayama. Substituent effect on solubilities of solids in supercritical fluids. naphthalene derivatives. *Industrial & Engineering Chemistry Research*, 30(6):1362–1366, 1991.

[81] Tadashi Nakatani, Tatsuya Tohdo, Kazunari Ohgaki, and Takashi Katayama. Solubilities of pyrimidine and pyrazine derivatives in supercritical fluids. *Journal of Chemical & Engineering Data*, 36(3):314–316, 1991.

[82] H Namatsu. Evaluation of critical-point behavior of fluoro-compounds. *Japanese Journal of Applied Physics. Part 2: Letters & express letters*, 45(33-36):L887–L890, 2006.

[83] Eyal Nir, Karl Kleinermanns, and Mattanjah S. de Vries. Pairing of isolated nucleic-acid bases in the absence of the DNA backbone. *Nature*, 408(6815):949–951, 2000.

[84] Robert M. Oag, Peter J. King, Christopher J. Mellor, Michael W. George, Jie Ke, Martyn Poliakoff, Vladimir K. Popov, and Viktor N. Bagratashvili. Determining phase boundaries and vapour/liquid critical points in supercritical fluids: a multi-technique approach. *The Journal of Supercritical Fluids*, 30(3):259–272, 2004.

[85] Mattias Östblom, Bo Liedberg, Linette M. Demers, and Chad A Mirkin. On the structure and desorption dynamics of DNA bases adsorbed on gold: A Temperature-Programmed study. *Journal of Physical Chemistry B*, 109(31):15150–15160, 2005.

[86] Roberto Otero, Maya Schöck, Luis M Molina, Erik Lægsgaard, Ivan Stensgaard, Bjørk Hammer, and Flemming Besenbacher. Guanine quartet networks stabilized by cooperative hydrogen bonds. *Angewandte Chemie International edition in English*, 44(15):2270–5, 2005.

[87] H. M. Pang and D. M. Lubman. Design of a pulsed valve for high-pressure ($nh_3$) injection into supersonic beam-mass spectrometry. *Revie of Scientific Instruments*, 59:2460–2463, 1988.

[88] H. M. Pang, C. H. Sin, and D. M. Lubman. Pulsed high-pressure liquid injection of biological molecules into supersonic beam/mass spectrometry with resonant two-photon ionization detection. *Applied Spectroscopy*, 42(7):1200–1206, 1988.

[89] Ding-Yu Peng and Donald B. Robinson. A new Two-Constant equation of state. *Industrial & Engineering Chemistry Fundamentals*, 15(1):59–64, 1976.

[90] Robert C. Petersen, Dean W. Matson, and Richard D. Smith. Rapid precipitation of low vapor pressure solids from supercritical fluid solutions: the formation of thin films and powders. *Journal of the American Chemical Society*, 108(8):2100–2102, 1986.

[91] Robert C. Petersen, Dean W. Matson, and Richard D. Smith. The formation of polymer fibers from the rapid expansion of supercritical fluid solutions. *Polymer Engineering & Science*, 27(22):1693–1697, 1987.

[92] Stefano Piana and Ante Bilic. The nature of the adsorption of nucleobases on the gold [111] surface. *Journal of Physical Chemistry B*, 110(46):23467–23471, 2006.

[93] Bruce E. Poling, John M. Prausnitz, and John P. O'Connell. *The properties of gases and liquids.* McGraw-Hill, 2001.

[94] Vladimir K. Popov, James A. Banister, Viktor N. Bagratashvili, Steven M. Howdle, and Martyn Poliakoff. Acoustic and photoacoustic measurements in supercritical fluids; a new approach to determining the critical point of mixtures. *The Journal of Supercritical Fluids*, 7(2):69–73, 1994.

[95] Danny Porath, Alexey Bezryadin, Simon de Vries, and Cees Dekker. Direct measurement of electrical transport through DNA molecules. *Nature*, 403(6770):635–638, 2000.

[96] Jean-Yves Le Questel, Christian Laurence, Abdeljalil Lachkar, Maryvonne Helbert, and Michel Berthelot. Hydrogen-bond basicity of secondary and tertiary amides, carbamates, ureas and lactams. *Journal of the Chemical Society, Perkin Transactions 2*, pages 2091–2094, 1992.

[97] Norman Ramsey. *Molecular beams.* The Clarendon Press, 1985.

[98] L. G. Randall and A. L. Wahrhaftig. Dense gas chromatograph/mass spectrometer interface. *Analytical Chemistry*, 50(12):1703–1705, 1978.

[99] P. A. Redhead. Thermal desorption of gases. *Vacuum*, 12(4):203–211, 1962.

[100] Otto. Redlich and J. N. S. Kwong. On the thermodynamics of solutions. v. an equation of state. fugacities of gaseous solutions. *Chemical Reviews*, 44(1):233–244, 1949.

[101] Richard J. Sadus. Calculating critical transitions of fluid mixtures: Theory vs. experiment. *AIChE Journal*, 40(8):1376–1403, 1994.

[102] E. Samoylova, H. Lippert, S. Ullrich, I.V. Hertel, W. Radloff, and T. Schultz. Dynamics of photoinduced processes in adenine and thymine base pairs. *Journal of the American Chemical Society*, 127(6):1782–1786, 2005.

[103] E. Sarantopoulou, Z. Kollia, A.C. Cefalas, Z. Samardzija, and S. Kobe. Preparation of ultra-thin films of DNA bases with laser light at 157 nm. *Thin Solid Films*, 495 (1-2):45–50, 2006.

[104] Thomas Schlatholter, Fresia Alvarado, Sadia Bari, and Ronnie Hoekstra. Ion-induced ionization and fragmentation of DNA building blocks. *Physica Scripta*, 73 (4):C113–C117, 2006.

[105] Gerhard M. Schneider. Physicochemical principles of extraction with supercritical gases. *Angewandte Chemie International Edition*, 17(10):716–727, 1978.

[106] Gina R. Shaub, Joan F. Brennecke, and Mark J. McCready. Radial model for particle formation from the rapid expansion of supercritical solutions. *The Journal of Supercritical Fluids*, 8(4):318–328, 1995.

[107] Chung Hang Sin, Matthew R. Linford, and Steven R. Goates. Supercritical fluid/supersonic jet spectroscopy with a sheath-flow nozzle. *Analytical Chemistry*, 64(2):233–238, 1992.

[108] I. W. M. Smith, D. Talbi, and E. Herbst. The production of HCN dimer and more complex oligomers in dense interstellar clouds. *Astronomy and Astrophysics*, 369 (2):611–615, 2001.

[109] Giorgio Soave. Equilibrium constants from a modified Redlich-Kwong equation of state. *Chemical Engineering Science*, 27(6):1197–1203, 1972.

[110] J.N. Spencer, S.W. Barton, K.A. Smith, W.S. Wolbach, J.F. Powell, M.R. Kirshenbaum, D.W. Firth, E.M. Harris, and T.A. Judge. Hydrogen bonded interactions of methanol and water with purines and pyrimidines. *Canadian Journal of Chemistry*, 61(12):2695–2698, 1983.

[111] E. Stofer, C. Chipot, and R. Lavery. Free energy calculations of Watson-Crick base pairing in aqueous solution. *Journal of the American Chemical Society*, 121 (41):9503–9508, 1999.

[112] Pascale Subra, Sandrine Castellani, Patrick Jestin, and Asdin Aoufi. Extraction of $\beta$-carotene with supercritical fluids: Experiments and modelling. *The Journal of Supercritical Fluids*, 12(3):261–269, 1998.

[113] Ya-Ping Sun. *Supercritical fluid technology in materials science and engineering.* CRC Press, 2002.

[114] Petra Swiderek. Fundamental processes in radiation damage of DNA. *Angewandte Chemie International Edition*, 45(25):4056–4059, 2006.

[115] A. Tavana, J. Chang, A. D. Randolph, and N. Rodriguez. Scanning of cosolvents for supercritical fluids solubilization of organics. *AIChE Journal*, 35(4):645–648, 1989.

[116] Ranjit Thakur and Ram B. Gupta. Rapid expansion of supercritical solution with solid cosolvent (RESS-SC) process: Formation of griseofulvin nanoparticles. *Industrial & Engineering Chemistry Research*, 44(19):7380–7387, 2005.

[117] Jean W. Tom, Pablo G. Debenedetti, and Robert Jerome. Precipitation of poly(-lactic acid) and composite poly(-lactic acid)-pyrene particles by rapid expansion of supercritical solutions. *The Journal of Supercritical Fluids*, 7(1):9–29, 1994.

[118] Susan C. Tucker and Michael W. Maddox. The effect of solvent density inhomogeneities on solute dynamics in supercritical fluids: A theoretical perspective. *The Journal of Physical Chemistry B*, 102(14):2437–2453, 1998.

[119] Johan van Dranen. The possibility of a theoretical calculation of the critical temperature. *The Journal of Chemical Physics*, 20(7):1175, 1952.

[120] James D. Watson and Francis H. Crick. Molecular structure of nucleic acids; a structure for deoxyribose nucleic acid. *Nature*, 171(4356):737–738, 1953.

[121] Paul B. Webb, Patricia C. Marr, Andrew J. Parsons, Harmanjit S. Gidda, and Steve M. Howdle. Dissolving biomolecules and modifying biomedical implants with supercritical carbon dioxide. *Pure and Applied Chemistry*, 72(7):1347–1355, 2000.

[122] John A. White and Bruce S. Maccabee. Temperature dependence of critical opalescence in carbon dioxide. *Physical Review Letters*, 26(24):1468–1471, 1971.

[123] S.L. Xu, M. Dong, E. Rauls, R. Otero, T.R. Linderoth, and F. Besenbacher. Coadsorption of guanine and cytosine on graphite: Ordered structure based on GC pairing. *Nano Letters*, 6(7):1434–1438, 2006.

[124] Seiichi Yamamoto, Kazunari Ohgaki, and Takashi Katayama. High-pressure phase behavior of eight binary mixtures of pyrimidine or pyrazine with carbon dioxide, ethylene, ethane or fluoroform. *Journal of Chemical & Engineering Data*, 35(3): 310–314, 1990.

[125] D. R. T. Zahn, S. Seifert, G. Gavrila, and W. Braun. Investigation of bioorganic/inorganic semiconductor interfaces. *Journal of Optoelectronics and Advanced Materials*, 9(3):522–526, 2007.

[126] Jianwei Zhang, Lloyd L. Lee, and Joan F. Brennecke. Fluorescence spectroscopy and integral equation studies of preferential solvation in supercritical fluid mixtures. *The Journal of Physical Chemistry*, 99(22):9268–9277, 1995.

[127] Qiang Zhang and Alec M. Wodtke. Using volatile solvents for ion formation in liquid molecular beam expansion mass spectrometry. *Analytical Chemistry*, 77(23): 7612–7617, 2005.

[128] Xiaogang Zhang, Buxing Han, Zhenshan Hou, Jianling Zhang, Zhimin Liu, Tao Jiang, Jun He, and Hongping Li. Why do co-solvents enhance the solubility of solutes in supercritical fluids? New evidence and opinion. *Chemistry - A European Journal*, 8(22):5107–5111, 2002.

[129] James W. Ziegler, John G. Dorsey, T. L. Chester, and D. P. Innis. Estimation of Liquid-Vapor critical loci for $CO_2$-Solvent mixtures using a Peak-Shape method. *Analytical Chemistry*, 67(2):456–461, 1995.

# Abbreviations

| Abbreviation | Explanation |
|---|---|
| AFM | Atomic Force Microscopy |
| DNA | Deoxyribonucleic Acid |
| EOS | Equation of State |
| ESI | Electrospray Ionization |
| HOPG | Highly Oriented Pyrolytic Graphite |
| IRAS | Infra-Red Absorption Spectroscopy |
| MACOR | Machinable glass-ceramic |
| MALDI | Matrix Assisted Laser Desorption Ionization |
| MID | Multiple Ion Detection |
| NIST | National Institute of Science and Technology |
| QMS | Quadrupole Mass Spectrometer |
| RESS | Rapid Expansion of Supercritical Solutions |
| RNA | Ribonucleic Acid |
| SCF | Supercritical Fluid |
| SLS | Soda Lime Silicate |
| SRK-EOS | Soave Redlich Kwong-Equation of State |
| STM | Scanning Tunneling Microscopy |
| TDS | Thermal Desorption Spectroscopy |
| UV-Vis | Ultraviolet-Visible |
| UNIFAC | Unified Functional Activity Co-efficient |
| vdW | van der Waals |

# Acknowledgement

I would like to start by sincerely thanking my Ph.D. advisor, Professor Klaus Rademann, for his scientific guidance, advice, support, and for providing a very pleasant working environment throughout the course of my work. I was most impressed by his ability to make any discussion, either scientific or non-scientific, a very enjoyable experience.

I also wholeheartedly acknowledge the support given to me by Dr. Wolfgang Christen. It was mostly due to his initial support, help, and guidance that I was able to work on my Ph.D. thesis here in Berlin. Moreover, I am also thankful for the very fruitful discussions and exchange of ideas throughout the period of this work, which played an important role in shaping this thesis.

A very important part of my Ph.D. were all my colleagues in the workgroup. I am grateful for the scientific and technical help from my Lab Fellows Tim Krause and Muhammer Bulat. I am also thankful for the help provided by Ms. Elizabeth Ehlers and Hanna Kaukel. I would especially like to mention the interesting coffee time discussions that made the daily work much more interesting. I am also obliged by the help provided by Maik Eichelbaum, Anne Simo and Ferdinand Friedrichs. I am also thankful to Robert Fenger and Christian Schaumberg for the help they provided with the AFM. From the older colleagues I would above all like to mention Claudia Ritter and Markus Geuß, who initially provided a very friendly atmosphere for me.

The technical staff also played a very important role and I am obliged to all of them. I am indebted to Michael von Löwis for the mass spectrometric analysis he provided for my samples. I would like to thank Bernd Lück and Sven Zillmann from the workshop for always providing me with the parts I required and Bernhard Buck and Helmut Draba from the electronic workshop for the friendly support throughout the years.

I am also thankful for the stipend provided to me by the Max Planck Society through the International Max Planck Research School: Complex Surfaces in Materials Science. Furthermore, I am very grateful to Professor Hajo Freund, especially for providing me with the opportunity to co-organise a scientific workshop, which helped me improve my organizational skills. I would especially like to mention Dr. Thomas Risse for his support and Bettina Menzel for the friendly help.

I am also very thankful to my Mom, Dad, Zeeshan, Jibran and Saba for their love and support. I would also like to remember my lovely niece Amber who I am going to meet very soon! Moreover, I am grateful and proud of my ever loving uncle Gulzar Ahmad, who always had encouraging words for me.

The love and support provided to me by Farooq, Asma and especially Daniyal, has been one of the forces during my stay here that helped me through the hard times and made the good times much more enjoyable.

Another important part of my stay here has been all the new friends that I made

and the old friendships that grew stronger. I would particularly like to thank Andreas, Asbjörn, Asif Bashir, Asif Sadiq, Erik, Hadj, Husnain, Imtiaz, Katrin, Konrad, Lars, Marko, Oliver, Patrick, Philipp Grüne, Philipp Schmidt, Sebastian, Tanya, Tasneem, Usman and many more. I must also mention the old friends who although have been far away but were still close to my heart. I thank Gul Zeb, Irfan, Muzaffar, and Aman for their support.

# Selbständigkeitserklärung

Ich erkläre, dass ich die vorliegende Arbeit selbständig und nur unter Verwendung der angegebenen Literatur und Hilfsmittel angefertigt habe.

Berlin, den 28.01.2008 Adnan Sarfraz